博士論文　(要約)

Detection and control of electron spin states in multiple quantum dots

(多重量子ドットにおける電子スピン状態の検出および操作)

伊藤　匠

Dissertation Supervisor: Professor Seigo tarucha Author: Takumi Ito

Detection and control of electron spin states in multiple quantum dots

Abstract

Semiconductor quantum dot (QD) is an artificial system that confines electrons in three-dimensions in the scale of the De Broglie wavelength (~ 100 nm). It is often called "artificial atom," and the energy levels of electrons are discretized by the quantum size effect, which is called the interaction effect. The QD systems have been widely utilized to study several topics: quantum transportation, physics of the electron states, spin-spin interactions, spintronics, quantum simulations and application for quantum information processing. These topics have been studied mainly in the single or double QD (DQD) and the QD system has been scaled up to study more complicated interactions and multiple qubits. Owing to the semiconductor micro-fabricating techniques, the multiple QD (MQD) system has potential scalability but the scale-up of QD systems whose electronic states can be precisely manipulated and detected requires several technical advances. For the application of the MQD system as spin qubits, the demonstration of the basic manipulations in the QQD system is a necessary step. For example, single spin control with a micro-magnet electron spin resonance (MM-ESR) method are established in a DQD and demonstrated in a triple QD (TQD). In the QQD system, four individual ESR signals are observed while individual control of electron spins in a QQD has not been realized yet. The MQD system is also considered as the promised platform for analogue quantum simulations owing to the established control methods in spin qubits experiments. In the spin state of the Fermi-Hubbard model, anti-ferromagnetism spin chain, spin frustration and Nagaoka ferromagnetism are expected to be observed; however experimental work in this aspect is lacking. For these researches, the exact control and detection method of the spin state in the further scaled up MQD system, such as QQDs and 5QDs, must be established.

This thesis present the demonstration of the charge and spin state in the MQD system. First, we propose the new device architecture and demonstrate it by fabricating and measuring the 5QD device with this new architecture. Then, utilizing the MQD system and established control methods, we investigate their applications. Second, we aim the realization of the multiple spin qubits and demonstrate

the coherent manipulation of the single electron spins confined in the QQD with the MM-ESR method. Finally, we investigate the charge and spin states of the QQD and suggest the measurement scheme to utilize the QQD system for the analogue quantum simulation model.

Acknowledgement

The work presented in this thesis has been performed under the guidance of Prof. Seigo Tarucha at the Tarucha Laboratory, Department of Applied Physics, University of Tokyo. I would like to express my sincerest gratitude to Prof. Seigo Tarucha, who gave me the opportunity to work on this exciting subject. He has always kindly encouraged me to work on these challenging experiments. His one-on-one supervision often continued four hours-a-day despite his busy schedule, and he provided considerable support and insightful comments. I am grateful to Prof. Akira Oiwa (Osaka Univ.), Lecturer Michihisa Yamamoto, and Assistant Prof. Sadashige Matsuo for their generous support throughout my research course.

I also feel gratitude to our Spin-Qubit group members in Riken. In almost all years of the PhD course, I have worked with Dr. Tomohiro Otsuka, who taught me the basic techniques and know-hows for the spin qubit experiments. My works described in this thesis was performed with him and I would not finish my PhD course in three years without his support. I appreciate Dr. Jun Yoneda, who taught me the basics of spin qubit experiments such as device fabrication and low temperature with high frequency experiments. I also thank Dr. Akito Noiri, who taught me the basics of the device fabrications and experimental techniques. It was great pleasure for me to work with them for almost all my research course in Tarucha group. Dr. Takashi Nakajima, Dr. Kenta Takeda, Dr. Matthieu Romain Delbecq, and Dr. Shinichi Amaha always encouraged me through daily conversations. Dr. Giles Allison always corrected my incorrect English. I have learned a lot of things through supervising Mr. Shotaro Kano for their bachelor's degree.

Most experiments presented here have been possible only with high-quality 2DEG. We are fortunate to work in close collaboration with Prof. Andreas D. Wieck' s group at Ruhr-Universität Bochum.

My graduate life has turned out to be really enjoyable, thanks to all current and former lab members who created this nice and open group atmosphere.

Finally, my heartfelt appreciation goes to my parents for their support and warm encouragement. Thank you.

Contents

Chapter 1

Introduction

1.1 Background

Semiconductor quantum dot (QD) [1–3] is an artificial system that confines electrons in three-dimensions in the scale of the De Broglie wavelength (~ 100 nm). It is often called an "artificial atom," and the energy levels of electrons are discretized by the quantum size effect which is the so called interaction effect. The number of electrons (or holes) in the dot can be electrically varied one-by-one; in addition, the other parameters associated with the orbital, spin, etc.., can be controlled. Utilizing these features, many types of quantum phenomena such as Kondo effect [4] and Pauli spin blockade (PSB) [5] have been observed until now. The QD systems have been widely utilized to study several topics: quantum transportation, physics of the electron states, spin-spin interactions [6, 7], spintronics [8], quantum simulations [9–11], and application for quantum information processing [12].

These topics have been studied mainly in single or double QD (DQD) [13,14]. In these ten years, aiming to study more complicated interactions and multiple qubits, several operations have been conducted to scale up the system. Owing to the semiconductor micro-fabricating techniques, the multiple QD (MQD) system has potential scalability. To date, the linear array of the QDs scaled up to quadruple QDs (QQDs) have been fabricated and utilized for the above topics [15–17]. More recently, half-filled QDs have been demonstrated in an array of nine QDs [18]. In addition to the linear QD arrays, a two-dimensional array of the QDs is also fabricated and the electrical control of the QD parameters are demonstrated [19–21]. One may consider that five tunnel coupled QDs (quintuple

QD: 5QD) can be prepared just by adding one QD to the QQD; however, scaling up QD systems whose electronic states can be precisely manipulated and detected requires several technical advances.

The theoretical model for quantum information processing with the QD system was proposed in 1998 by Loss and DiVincenzo [22, 23]. The electron spins confined in QDs form a natural two-level system and this system is utilized to make quantum bits (spin qubits). Two electron spins confined in a DQD can be also utilized as qubit which is called a singlet-triplet qubit [24]. The QD system has advantages in implementing spin qubits, including a relatively long coherence time in the solid-state devices, potential scalability owing to the well-established fabrication technology and small physical size per qubit. Basic manipulations such as initialization, readout, and single and two qubit control have been established in DQDs [25–28]. In TQDs, further manipulation methods of spin qubits have been established such as long-distant coherent couplings [29–31] and hybrid qubits in different codes [32]. Considering the application as a spin qubit and the realization of practical quantum information processing, one of the targets is developing a five qubit system, the smallest quantum system that can be used to perform perfect quantum error correction [33]. Toward the multiple qubit system, the demonstration of the basic manipulations in the QQD system are necessary steps. For example, the single spin control with the micro magnet electron spin resonance (MM-ESR) method are established in a DQD [34] and demonstrated in a triple QD (TQD) [17]. In the QQD system, four individual ESR signals are observed [35] while the individual control of electron spins in a QQD has not been realized yet.

Quantum simulation experiments are performed on multiple platforms [36–42] because of the potential for realizing novel electronic and magnetic properties of correlated-electron phases in low-dimensional condensed-matter physics [43–45]. Since the MQD system is a scalable platform that is naturally described by a Fermi-Hubbard model and can make use of the developments described above, it is considered a promising platform for analogue quantum simulations. Recently, an experimental work of the TQD system as the Fermi-Hubbard model was reported; however, it focused on the charge interaction and not on the spin interaction [7]. In the spin state of the Fermi-Hubbard model, anti-ferromagnetism spin chain, spin frustration [44, 46–49], and Nagaoka ferromagnetism [50] are expected to be observed but the experimental work about it is rarely reported. For these research studies, the exact control and detection method of spin states in further scaled up MQD systems, such as QQDs and 5QDs, must be established.

1.2 Motivation of Present Work

In the conventional device structure, there are some difficulties in the exact detection and control of the charge states of the MQD. For further scaling up the MQD system, we propose a new device architecture and demonstrate it by fabricating and measuring the 5QD device with this new architecture. Then, utilizing the MQD system and the established control methods, we investigate their applications. First, we aim to realize the multiple spin qubits and demonstrate the coherent manipulation of the single electron spins confined in the QQD with the MM-ESR method. Second, we investigate the charge and spin states of the QQD and propose a method to utilize the QQD system for the analogue quantum simulation model.

1.3 Organization of this Thesis

In chapter 2, the basics for spin qubits with single QDs are described. First, we describe the electronic properties of QDs and the experimental techniques to control and detect the electron charge and spin states. Second, the theory and basic techniques to realize the spin qubits are described.

In chapter 3, the difficulties in scaling up the MQD system and solutions are described. First, the concept of the new device architecture for further scaling up are described and then the measurement results in the fabricated 5QD device are shown. In the measurement, the charge state control and the simultaneous readout of the multiple charge sensors are demonstrated.

In chapter 4, the single spin manipulation measurement in each dot of the QQD device with the MM-ESR method is described. First, the device design and setup and the voltage pulse scheme are described. The coherent control of four individual spins are demonstrated by observing four Rabi oscillations. Finally, the estimation of the g-factor, local magnetic field, and the actual QD positions are demonstrated from the measured results.

The part related to the application to quantum simulations (chapter 5) can not be published in this thesis and it is replaced in this version.

In chapter 6, the conclusions and future prospects of this study are provided.

Chapter 2

Spin Qubits in Quatum dot

In this chapter, we describe the basics for spin qubits with single QDs. Firstly, we describe the electronic properties of QDs and the experimental techniques to control and detect the electron charge and spin states. Secondly, theory and basic techniques to realize the spin qubits are described.

2.1 Electronic property of Quantum Dots

Here, we first describe the basic properties of single QDs and then multiple QDs such as double, triple and quadruple QD.

2.1.1 Basic theory of Single Quantum Dot

A QD is an artificial architecture that confines conduction electron (or hole) in three dimentionally. In general, QDs are connected to electron reservoirs or other QDs via tunnel barriers and confined electrons can be exchanged between the dot and reservoirs or between the dots. Normally, in order to control the electrostatic potential of QD, gate electrodes are capacitively connected to QDs. Especially in single QD with two electron reservoirs, we can investigate its property with transport current and voltages through a QD. In Fig.2.1, a QD is connected to two electron reservoirs and one gate electrode is capacitively coupled.

Coulomb oscillation is one of the unique phenomena observed in the QD system. By changing gate voltage, the conductance through a QD show periodic peaks (*Coulomb peak*) and the conductance is strongly suppressed between the

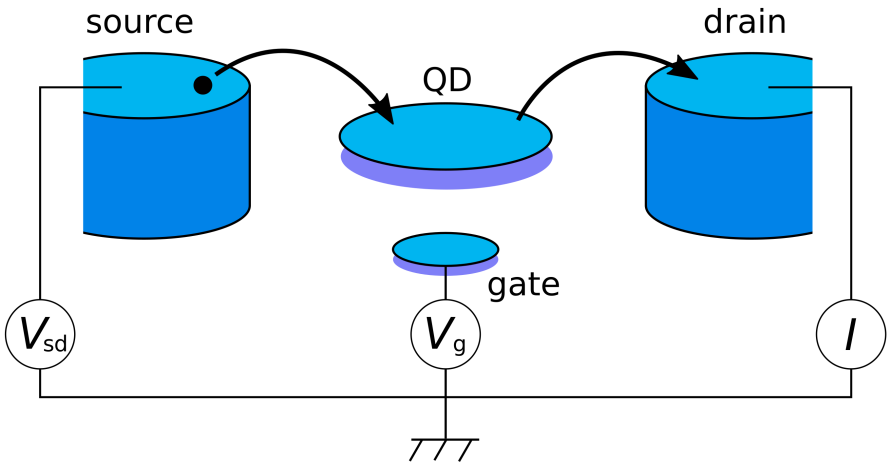

Figure 2.1: Schematic of a QD device. A QD is connected with two electron reservoirs, source and drain. Finite bias voltage V_{sd} is applied across the reservoirs and the current through the QD I is measured. In order to tune the electronic parameters of QD, usually more than one capacitively-coupled gates are used.

peaks (*Coulomb blockade*). These features are explained with Constant Interaction (CI) model.

Constant Interaction model

CI model is the simplest model to explain Coulomb oscillation. This model is based on following two assumptions:

1. Coulomb interaction between the electron inside QD is given by a capacitive coupling constant C,
2. Single particle energy level spectrum of the electrons E_{n} are independent to the interaction.

A capacitive constant C in 1st assumption is given by $C = C_{\mathrm{S}} + C_{\mathrm{D}} + C_{\mathrm{G}}$ (C_{S} is a capacitive coupling between the QD and the source, C_{D} is that between the QD and the drain, C_{G} is that between the QD and the gate electrode.) In the case of a lateral QD, 2 Dimentional Electron Gass (2DEG) around the QD also connects to QD capacitively and a capacitive coupling between the QD and 2DEG is also added to C. Energy level of single particle confined in QD E_{n} depends on the

confinement potential and the external magnetic field $B_{\rm ext}$ but, from the second assumption, does not depend on the number of electrons. Then, the total energy U of a QD with N electrons in the ground state is given by

$$U(N) = \frac{1}{2C}[-e(N - N_0) + C_{\rm S}V_{\rm S} + C_{\rm D}V_{\rm D} + C_{\rm G}V_{\rm G}]^2 + \sum_{n=1}^{N} E_{\rm n}(B), \quad (2.1)$$

where $-e$ is the single electron charge, eN_0 is the positive background charge by donor ions in semiconductor. $V_{\rm S}, V_{\rm D}$ and $V_{\rm G}$ are the voltages applied on the source, drain and gate, respectively. $U(N)$ can be controlled continuously by changing these voltages. The *electrochemical potantial* $\mu(N)$ is defined as the energy diffrence between the N-electron ground state GS(N) and $(N-1)$-electron ground state GS($N-1$). From Eq.(2.1),

$$\mu(N) \equiv U(N) - U(N-1) \quad (2.2)$$

$$= \left(N - N_0 - \frac{1}{2}\right) E_C - \frac{E_{\rm C}}{e}(C_{\rm S}V_{\rm S} + C_{\rm D}V_{\rm D} + C_{\rm G}V_{\rm G}) + E_{\rm N}, \quad (2.3)$$

where $E_{\rm C} \equiv e^2/C$ is the *single electron charging energy*. By definition, $\mu(N)$ corresponds to the energy required for the addition of N-th electron to QD in GS($N-1$). The *addition energy* is defined as the difference of the electrochemical potentials between the successive ground states and is written by

$$E_{\rm add}(N) \equiv \mu(N) - \mu(N-1) \quad (2.4)$$

$$= E_{\rm C} + \Delta E, \quad (2.5)$$

where $\Delta E \equiv E_{\rm N+1} - E_{\rm N}$ is the succesive quantized energy level spacing. Only when the N-th and $(N+1)$-th electron are spin degenerated and occupy the same orbital with N-th electron, ΔE becomes 0 and $E_{\rm add}(N) = E_{\rm C}$.

Coulomb oscillation

The electron transport through a QD is determined by how the $\mu(N)$ is aligned with the electrochemical potentials of the source $\mu_{\rm S}$ and the drain $\mu_{\rm D}$. A bias voltage $V_{\rm SD} = V_{\rm S} - V_{\rm D}$ across the source and the drain opens an energy window

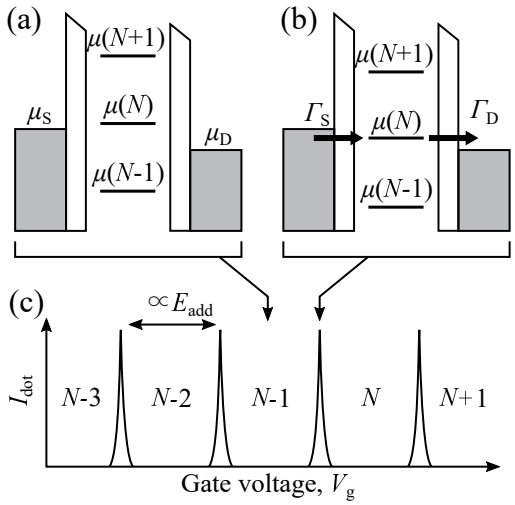

Figure 2.2: The relationship between the electrochemical potential of the QD and those of the source or drain in the low bias regime to generate Coulomb blockade (a) and the single electron tunneling (b). (c) Coulomb oscillation as a function of gate voltage and the corresponding change in the number of electron in the QD.

(*bias window*) with a gap of $|eV_{\rm SD}|$. When the chemical potential of a QD $\mu(N)$ is within the bias window, electron transport through a QD is allowed. For the observation of the Coulomb oscillation, electron temperature must be low enough compared with charging energy $E_{\rm C}$ and energy spacing ΔE, i.e. $k_{\rm B}T \ll E_{\rm C}, \Delta E$ where $k_{\rm B}$ is Boltzmann constant. In GaAs QD system, electron temperature is typically below 1K. In the followings, we assume that this condition is always satisfied. The electron transport through a QD can be categolized in to two different regime : low bias regime ($|eV_{\rm SD}| \ll E_{\rm C}, \Delta E$) and high bias regime ($|eV_{\rm SD}| > E_{\rm C}, \Delta E$).

Low bias regime $|eV_{\rm SD}| \ll E_{\rm C}, \Delta E$ In the low bias regime, at most only single energy level in the QD can contribute to electron transport. Electron tunneling is allowed only when an electrochemical potential $\mu(N)$ is within the bias window, i.e. $\mu_{\rm S} \geq \mu(N) \geq \mu_{\rm D}$. Otherwise electron transport through a QD is forbidden and the number of electrons confined in a QD N is fixed (*Coulomb blockade*, Fig.2.2 (a)). Coulomb blockade can be lifted by adjusting an electrochemical potential $\mu(N)$ within the bias window, by tuning gate voltage (Fig.2.2 (b)). In such condition, the number of electrons in the QD can be both of $N-1$ and

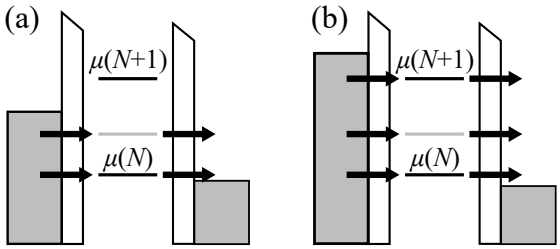

Figure 2.3: The relationship between the electrochemical potential of the QD and those of the source or drain in the high bias regime. (a) Electron tunneling via a ground state and the excited state for N electrons. (b) Two electron tunneling for the N and $N+1$ electron state when the two ground states are in the bias window.

N, and a single electron can tunnel through the QD one by one. This process is called as *single electron tunneling* or *Coulomb peak*. By sweeping gate voltage, single electron tunneling and Coulomb blockade are repeated and dot current $I_{\rm dot}$ oscillates and it is known as *Coulomb oscillation* (Fig.2.2 (c)).

The separation of Coulomb peak $\Delta V_{\rm G}$ is given by

$$\mu(N, V_{\rm G}) = \mu(N+1, V_{\rm G} + \Delta V_{\rm G}) \tag{2.6}$$

Using Eqs.2.3 and 2.5, $\Delta V_{\rm G}$ becomes

$$\Delta V_{\rm G} = \frac{C}{eC_{\rm G}} E_{\rm add}(N) \tag{2.7}$$

and is proportional to $E_{\rm add}$.

High bias regime $|eV_{\rm SD}| > E_{\rm C}, \Delta E$ In the high bias regime, multiple levels can be within the *bias window* and contribute to $I_{\rm dot}$. By increasing the *bias window* to satisfy $|eV_{\rm SD}| \geq \Delta E$, not only the ground state but also excited state can be within the *bias window.* Under this condition, there are multiple paths for electron tunneling shown as Fig.2.3 (a). In general, $I_{\rm dot}$ changes by the paths within *bias window*, however, how much it changes depends on many parameters such as tunnel coupling between the lead and the ground or excited state. By increasing the *bias window* further to satisfy $|eV_{\rm SD}| \geq E_{\rm add}$, the ground state for $N+1$ electron is within the bias window and two electron tunneling is allowed (Fig.2.3 (b)).

2.1.2 Lateral Quanrum Dots

There are various kinds of QDs with different materials and size. such as "vertical" QDs and "lateral" QD in a semiconductor heterostructure, "self-assembled" QDs with nano-gap electrodes, InAs nanowire QDs and carbon nanotube QDs. For the research of spin qubits, lateral QDs are adopted because

1. High tunability of the QD parameters such as inter-dot and QD-lead couplings with gate voltages,
2. Good scalability thanks to semiconductor micro-fabricating techniques.

These features are very important for application as spin qubit. Here, we describe about the character of the lateral quantum dot and established experimental techniques.

High Electron Mobility Transistor

High Electron Mobility Transistor (HEMT) is a field effect transistor formed in a Two-Dimentional Electron Gas (2DEG) at a semiconductor hetero-junction. Thanks to the development of thin film facrication technique such as Molecular Beam Epitaxy, it enabe to realize lattice-matched layer structure of quantum wells and hetero-junctions inside of semiconductor. In such a hetero-junction where semiconductor materials with different band gaps are connected with an atomically flat interface, an ideal 2DEG is formed. A typical example of a heterojunction is constructed by III-V group smeiconductors such as GaAs and $Al_xGa_{1-x}As$ ($Al_xGa_{1-x}As$ is semiconductor in which some of Ga atoms are replaced by Al atoms). By doping doners such as Si to $Al_xGa_{1-x}As$ layer, electrons suplied from these doners are trapped at a triangle-shaped potential as shown in Fig.2.4 (a) and (b). Here, the electron momentum in the growth direction is quantized due to the strong confinement in the thin conduction layer. Therefore, the electron motion in this direction is neglected when the quantized energy level splitting is much larger than the thermal fluctuation energy.

This 2DEG is a clean system and has a very high electron mobility. This is because ionized impurity scattering, main source of electron scattering in a low temperature experiment, is suppressed since the donor layer and the 2DEG layer are spatially separeted. Espacially at very low temperature, phonon scattering is suppressed, and the electron mobility exceeds $10^6 \mathrm{cm}^2/\mathrm{Vs}$. Therefore, electron transport is ballistic even on sub-micrometer scales at cryogenic temperatures.

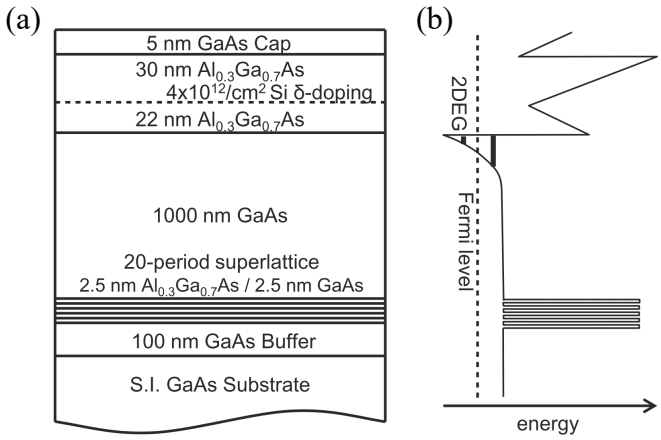

Figure 2.4: (a) A typical heterostructure of HEMT wafer. (b) Schematic image of the corresponding energy profile of the conduction band. The images are adopted from [51].

Thanks to this feature, HEMT wafers are widely utilized to realize low dimentional electron systems such as lateral quantum dots and quantum wires. The 2DEG itself has long been an appealing system to study for mesoscopic physics such as ballistic transport, wave interference and quantum Hall effects.

To fabricate nano-structures in the 2DEG, further confinement of carriers in the lateral directions is necessary. For this purpose, metal gate electrodes with Schottly barriers can be utilized to locally change the electriv potential. The Schottky barrier is a current-rectifying junction formed at the metal-semiconductor interface, with appropriate choices of metal and semiconductor materials. The 2DEG region beneath the gates can be depleted by application of sufficiently negative voltages on the Schottky gates. This gives *in-situ* tunability of confinement potential in the 2DEG in the lateral directions.

Lateral Quantum Dot

Lateral QDs are formed in a 2DEG by applying negative voltages to metal gate electrodes on the surface of the wafer (Fig.2.5). The metal gates create the Schottky barriers when negatively biased, the barrier potential rises above the Fermi level of the 2DEG to finally deplete it under the gate electrodes. Then, the lateral QD is formed by applying appropriate voltages to the surface gate electrodes. In lateral QDs, electrons are confined by barrier potential and the inter-dot and

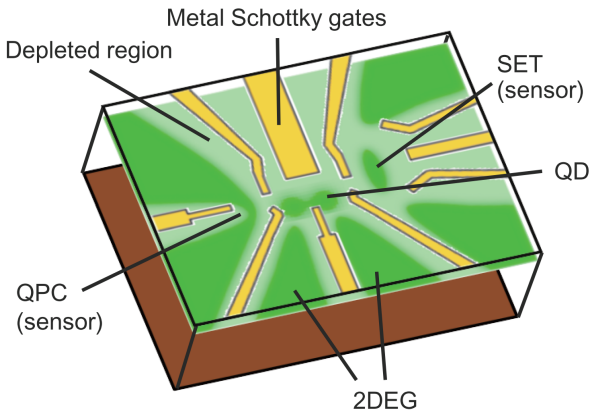

Figure 2.5: Schematic image of the lateral QD structure. The 2DEG is colored in green. The images are adopted from [51].

dot-lead tunnel couplings can be controled by the gate voltages in wide range. In addition to this, less limitation of the device design is one of the feature of lateral QDs.

Quantum Point Contact

Quantum Point Contact (QPC) is the simplest exmaple of gate defined structures, a quantum one-dimentional channel that is short enough to regard the constriction as a point. A QPC can be formed in the 2DEG by negatively biasing a pair of Schottky gate electrodes to deplete regions on two sides of a narrow channel. The conductance G through a QPC follows Landauer fomula without scattering and is given by $G = Ne^2/h$, where N is the number of the occupied one-dimensional subbands, e is charge of electron and h is Plank constant. Especially in the case of no external magnetic field, N becomes even due to spin degeneracy. In 2DEG system, QPC can be formed by applying negative voltage to two gate electrode with small separation and its conductance is quantized. Fig.2.6 is the gate voltage dependence of the conductance of a QPC and the conductance is quantized by e^2/h. The QPC conductance shows step-like feature. The number of subbands in the bias window can be changed by the gate voltage here. While N is kept same, the QPC conductance does not change (plateau). When N changes between the plateaus, the QPC conductance changes drastically (step).

When the QPC conductance is tuned to the step region of the QPC conduc-

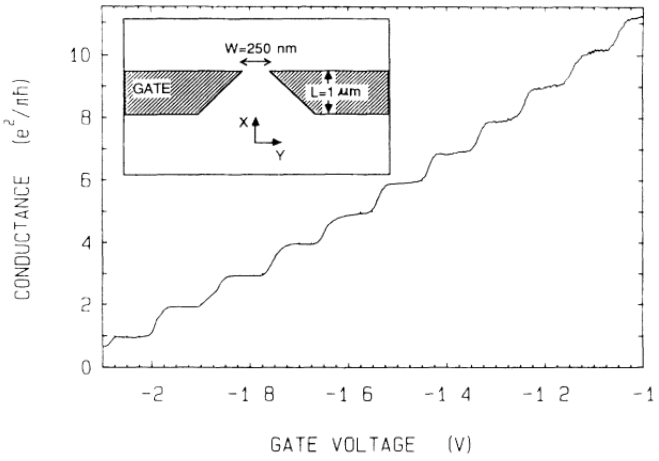

Figure 2.6: Gate voltage dependence of the conductance of QPC. Conductance is quantized by $2e^2/h$ [52].

tance, QPC becomes highly sensitive to the electrostatic environment including the arrangement of electrons trapped nearby. In rateral QDs, QPCs placed the visinity of the QDs enables the measurement of the charge configuration inside QDs from the conductance through an adjacent QPC. The change of charge configuration changes nearby electrostatical environment and detected as the change of the QPC conductance. This charge sensing technique is useful in the multiple QD system that $I_{\rm dot}$ through the multiple QD array become too small to detect on a realistic time scale. A proximal SET can be used in place of a QPC for detecting the QD electron number, since the only necessary ingredient is the susceptibility to the surrounding electrostatic potential. Indeed, an SET tuned at the slope of a Coulomb peak has more than an order of magnitude higher sensitivity to the charge rearrangement in the QD.

Charge Sensing Techniques

In lateral QDs, current through the QD ($I_{\rm dot}$) can be utilized to measure charge state inside QD. But, in order to achieve a few electron regime, large negative voltage is necessary but tunnel barrier between the QD and reservoir becomes too thick to measue $I_{\rm dot}$. In such a case, QPC placed nearby lateral QDs can be utilized as a charge sensor. The conductance through a QPC changes drastically from one plateau to the next when the number of the subbands in the bias window is changed one by one. When the gate voltage is tuned at the steep slope between

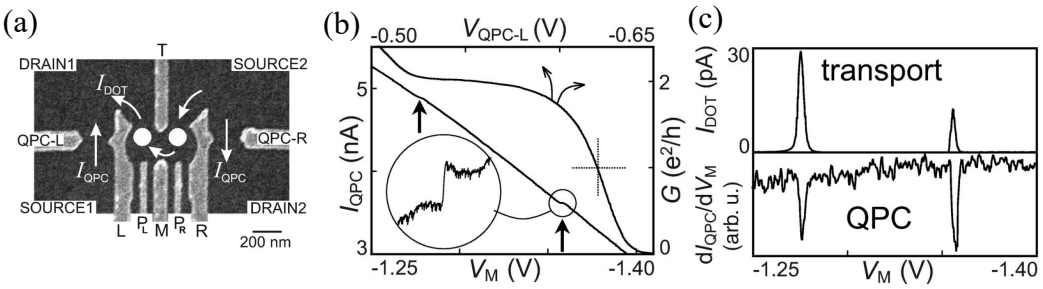

Figure 2.7: Charge sensing using QPC [53]. (a) Scanning electron microgpah (SEM) image of DQD with QPC. (b) The gate voltage $V_{\rm M}$ dependence of the current through QPC $I_{\rm QPC}$ and the gate voltages $V_{\rm APC}$ and $V_{\rm L}$ dependence of the conductance of QPC G $V_{\rm APC}$ and $V_{\rm L}$ are the voltages applied on the gate electrodes that form QPC. (c) The comparison between the transport current $I_{\rm dot}$ and the charge sensing signal $dI_{\rm QPC}/dV_{\rm M}$

the plateaus, the QPC conductance becomes highly sensitive to the electrostatic environment including arrangement of electrons trapped nearby. This enables the measurement of the charge occupation in a QD from the conductance through an adjacent QPC. The change of electron number configuration in a QD modifies the electrochemical potential in the QPC channel, which is detected as a step-like rise in the QPC current or a kink in the current derivative.

Fig.2.7 shows the experiment of charge detection using QPC. In the following measurement, by applying negative gate voltages on gate electrodes, the DQD and two QPCs are formed at the position shown as white circle and white arrows in Fig. 2.7 (a), respectively. Fig.2.7 (b) shows the $V_{\rm QPC-L}$ dependence of the QPC conductance G and $V_{\rm QPC-L}$ is tuned to steep point depicted as the dotted cross so as to be sensitive to nearby electrostatic potential. Fig.2.7 (b) also shows the $V_{\rm M}$ dependence of the $I_{\rm QPC}$. $I_{\rm QPC}$ decreases by increasing $V_{\rm M}$ negatively but increases step-like at some point depicted as black arrows. At these points, an electron tunnels to a reservoir and it causes the change in the nearby electrostatic potential. This is detected as the increase of the G.

Fig.2.7 (c) shows the comparison of the $V_{\rm M}$ dependence of the $I_{\rm dot}$ and $dI_{\rm QPC}/dV_{\rm M}$ in the same range of $V_{\rm M}$. The dips are observed in $dI_{\rm QPC}/dV_{\rm M}$ at the same position of the Coulomb peak in $I_{\rm dot}$. It means that the QPC can detect the change of the electron number in the QDs one by one.

RF reflectometry

As mentioned above, the charge sensing techniques using QPC or SET are very effective for the charge state measurement in multiple QDs. At first, the signal of the charge sensor was detected as DC current through a QPC or SET with a finite bias voltage. However, in this method, the resistance of the charge sensor (tens of $k\Omega$) and a parasitic capacitance between the wire and setup (hundreds of pF) configures the RC filter and it causes the difficulty in fast measurement. In addition to this, in the measurements with low frequency, $1/f$ noise become dominant and prevents highly sensitive measurements. RF reflectometry that configures the tank circuit with charge sensor as resistance is one of the solutions of these difficulties. In this section, we explain the basic principle of RF reflectometry and the applications in multiple QDs.

Impedance matching Either RF-QPC or RF-SET uses a different principle for charge state detection. But, in both method, the charge sensor is configured in a tank circuit and charge state is readout with reflected RF signal by impedance mismatch. In general, input voltage $V_{\rm in}$, input current $I_{\rm in}$, reflected voltage $V_{\rm ref}$ and reflected current $I_{\rm ref}$ has following relation ship,

$$V_{\rm in} + V_{\rm ref} = (I_{\rm in} - I_{\rm ref}) Z_{\rm eff} = \left(\frac{V_{\rm in}}{Z_0} - \frac{V_{\rm ref}}{Z_0} \right) Z_{\rm eff} \tag{2.8}$$

where output impedance Z_0 and imput impedance $Z_{\rm eff}$. Reflection coefficient ρ can be written as

$$\rho = \frac{V_{\rm ref}}{V_{\rm in}} = \frac{Z_{\rm eff}^* - Z_0}{Z_{\rm eff} + Z_0}. \tag{2.9}$$

Here, we can write $Z_0 = R_0 + iX_0$ and $Z_{\rm L} = R_{\rm L} + iX_{\rm eff}$ an dthe power transmitted to the inut side $P_{\rm IN}$ can be written as

$$P_{\rm IN} = Re \left(\frac{|V_{\rm IN} + V_{\rm REF}|^2}{Z_{\rm L}} \right) = \frac{4|V_{\rm IN}|^2 R_{\rm L}}{(R_{\rm L} + R_0)^2 + (X_{\rm L} + X_0)^2} \tag{2.10}$$

When $Z_{\rm L} = Z_0^*$, eq.2.10 gives maximum value of $P_{\rm IN}$ ($P_{\rm MAX}$)

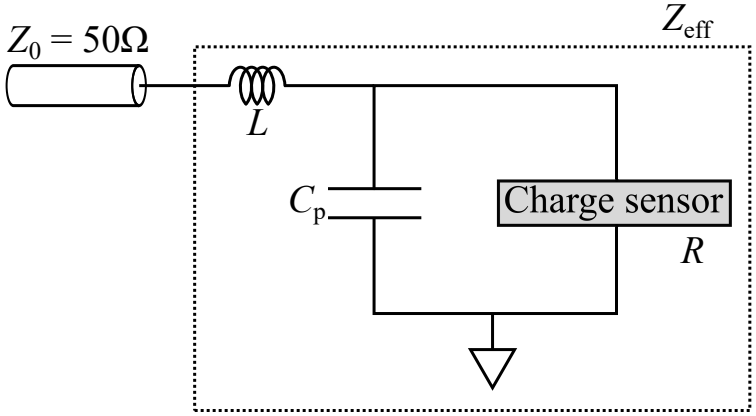

Figure 2.8: Schecmatic picture of the tank circuit for RF reflectometry

$$P_{\text{MAX}} = \frac{|V_{\text{IN}}|^2}{R_0} \tag{2.11}$$

it gives the power reflection S_{11}

$$S_{11} = 1 - \frac{P_{\text{IN}}}{P_{\text{MAX}}} = \left| \frac{Z_0 - Z_{\text{L}}^*}{Z_0 + Z_{\text{L}}} \right|^2 \tag{2.12}$$

When Z_{L} Z_0^*, S_{11} becomes 0 (*Impedance matching*). In normally, radio-frequency circuit is designed to realize impedance matching so as to transmit RF power efficiently. In RF reflectometry, however, Z_{L} is modulated nearby Z_0 and we detect this $Z_{[}\text{L}]$ changes via the change of S_{11}.

Tank circuit Tank circuit for RF reflectometry is configured of a resistance R of the charge sensor, a inductance L of on chip coil and a parasitic capacitance C_{p} between the measurement set-ups shown as Fig.2.8. The effective impedance Z_{RC} of this tank circuit of a rf career with frequency f is written as

$$Z_{\text{RC}} = 2\pi i f L + \frac{1}{2\pi i f C_{\text{p}} + \dfrac{1}{R}} \tag{2.13}$$

From eq.2.13, we can get the resonant frequency $f_{\rm res}$ that $Z_{\rm RC}$ becomes real number as

$$f_{\rm res} = \frac{1}{2\pi}\sqrt{\frac{R^2C_{\rm p} - L}{R^2C_{\rm p}^2L}} \tag{2.14}$$

When $R^2C_{\rm p} \gg L$ is satisfied, eq.2.14 becomes

$$f_{\rm res} \sim \frac{1}{2\pi\sqrt{C_{\rm p}L}} \tag{2.15}$$

and the impedance in resonance condition $Z_{\rm RC}(f = d_{\rm res}) = Z_{\rm res}$ becomes

$$Z_{\rm res} = \frac{L}{RC_{\rm p}} \tag{2.16}$$

Here, the resistance that realize impedance matching $R_{\rm match}$ is written as

$$R_{\rm match} \equiv \frac{L}{Z_0C_{\rm p}} \tag{2.17}$$

The typical value of the resistance for charge sensor is about 10 $k\Omega$ and the tank circuit is designed so that $R_{\rm match}$ becomes neighbourhood by choosing L. In the experimental set-ups, Z_0 is a characteristic impedance of coax cable (50Ω). Fig.2.9 shows the frequency dependence of $S11$ in each charge sensor resistance. In $R = R_{\rm match}$, the reflection is suppressed at the resonance frequency of tank circuit and a dip is observed.

2.1.3 Charge States of Multiple Quantum Dots

A *multiple QD* (MQD) is the system that some single QDs are tunnel coupled each other. This system enables us to observe the various phenomena caused by electron-electron interactions and it is also necessary for the realization of the practical quantum information processing. For both purpose, it is the first important step that its charge states are understood and controlled. Here we describe about the *charge stability diagram* that is an essential tool for the charge state manipulations and show those of some multiple QD systems. Furthermore, we describe the spin correlated phenomena observed in these system.

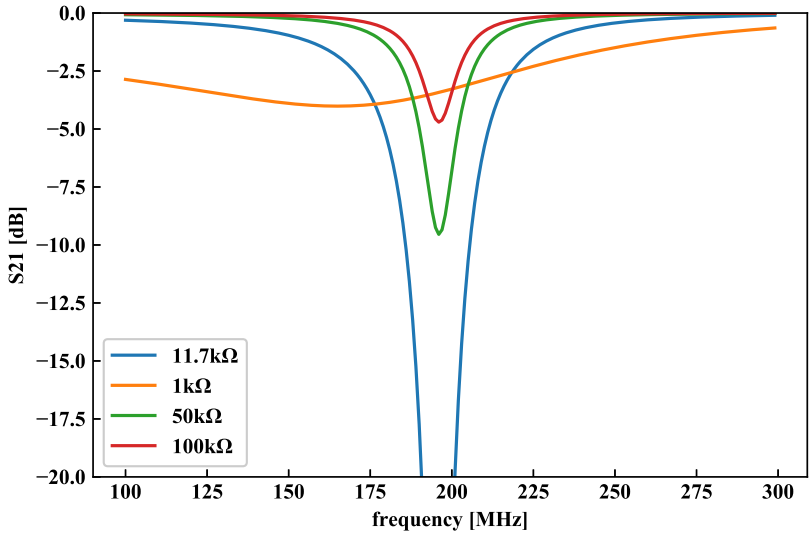

Figure 2.9: The numerical calculated frequency dependence of the power reflectance in each resistance value, where $C_{\mathrm{p}} = 1.06$pF and $L = 620$nH.

Charge Stability Diagram of Double Quantum Dot

A charge stability diagram maps the equilibrium charge states in multiple QDs in gate-voltage space. In the following, we denote the electron number in QD_i as n_i and the equilibrium charge states of the multiple QD system as (n_1,n_2,...).

Figs.2.10 (a)-(c) show schematic pictures of the stability diagram of DQD. Here, the solid straight lines (*charge transition lines*) indicate the gate voltages that the equilibrium charge state changes. In Fig.2.10 (a), we assume that the QDs are not capacitively coupled each other and the energy level of QD_{i} is affected only by the voltage of the gate electrode $\mathrm{G_i}$ (V_{Gi}). In this case, the charge transition lines are either completely vertical or horizontal in the V_{G1}-V_{G2} voltage plane. The charge configureations in a DQD (n_1,n_2) in each voltage conditions are distinguished by counting the charge transition lines from completely depleted region $(0, 0)$.

In the actual QD system, the neighboring QDs are capacitively coupled and there are crosstalk between the QD_i an the gate electrode Gj ($i \neq j$). Fig.2.10 (b) shows a schematic image of stability diagram in case that $\mathrm{G_i}$ has a finite cross-coupling with $\mathrm{QD_i}$. Normally, the coupling between a QD and a gate electrode

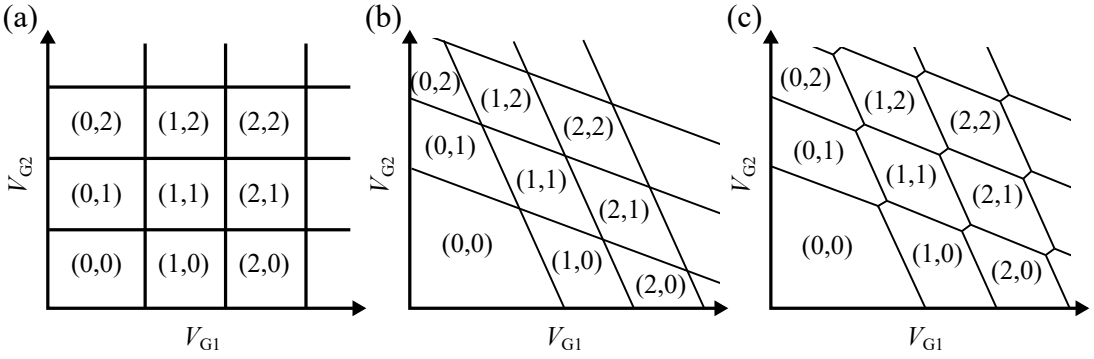

Figure 2.10: DQD stability diagram. (a)-(c) Schematic pictures of charge stability diagrams. In (a), QD_1 and QD_2 are not capacitively coupled each other and a gate electrode G_1 (G2) is capacitively coupled only to QD_1 (QD_2) with no cross-coupling between the other dot. $n_{\rm i}$ is solely determined by the gate voltage $V_{\rm Gi}$ ($i = 1, 2$) as in single QD and charge transition lines are either completely vertical or horizontal in the $V_{\rm G1}-V_{\rm G2}$ plane. In (b), $G_{\rm i}$ has finite cross-coupling to QDj ($i \neq j$). In (c), QD_1 and QD_2 are capacitively coupled.

is determined by a geometrical distance and cross-coupling between QD and $G_{\rm j}$ is smaller than the coupling between $QD_{\rm i}$ and $G_{\rm i}$ ($i \neq j$). In Fig.2.10 (b), charge transition lines have finite slopes due to cross-couplings. In Figs.2.10 (a) and (b), four charge states are degenerated at the cross point of the charge transition lines.

In Fig.2.10 (c), the effect of the capacitive coupling between the QDs is further included. Here, due to the capacitive coupling between the dots, cross point of the charge transition lines are separated to two *triple points* and the honeycomb structure is observed. The spacing between two triple points is defined by the capacitive and tunnel coupling between the QDs.

In the low bias region, the electron transport through DQD is observed only around the triple point that all energy levels locate inside the bias window and the current measurement through the dots does not play a role so as to detect the charge states of DQD. However, the charge sensor works even in the region that all energy levels do not adjusted and can detect all charge transitions in DQD.

Fig.2.11 shows the stability diagram near a pair of neighboring triple points with no bias voltage. When the inter-dot tunnel coupling $t_{\rm C}$ is much smaller than the inter-dot capacitive coupling (*weak-coupling* regime), charge transition lines are observed where two lowest electrochemical potentials degenerate shown as solid lines in Fig.2.11. When $t_{\rm C}$ is not negligible (*strong-coupling* regime),

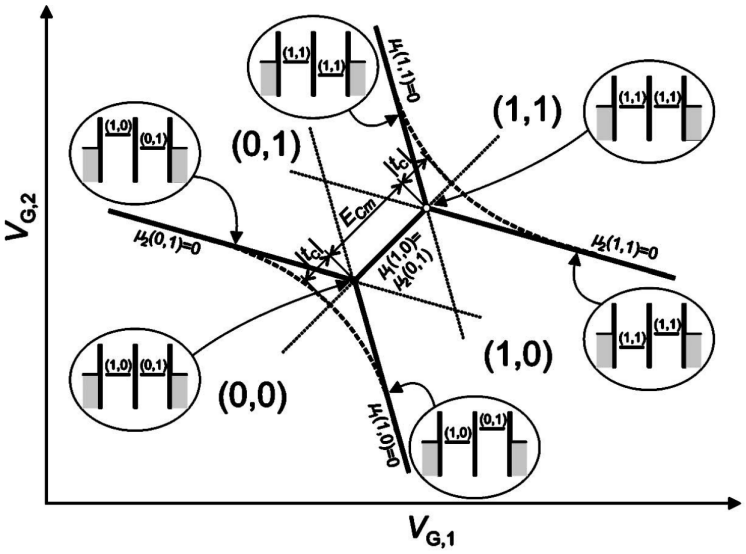

Figure 2.11: Stability diagram around neighboring triple points with no bias voltage [12].

electrons do not localized in either QD and they occupy the hybridized orbitals which distribute over the whole DQD. Due to this hybridization, the energy of the bounding (anti-bounding) state is decreased (increased) by $|t_{\mathrm{C}}|$. Therefore, the charge transition lines around triple points bend as depicted the dotted lines in Fig.2.11.

Charge Stability Diagram of Triple Quantum Dot

Generally speaking, increasing number of QDs causes more complexed charge states and difficulty in clarification of its distribution due to the capacitive couplings between the QDs. In n-QD system, capacitive coupling can be written as n by n size matrix (*cross-capacitance matrix*) and its values are mainly defined geometrical distance between the QDs. TQD has a degree of freedom in arrangement of each three QDs and it also affects capacitive couplings. In addition to this, the charge states of n-QD can be controlled with n-plunger gate voltages and distribute n-dimensional space defined by these voltages. Two-dimensional stability diagram can be said as a slice of n-dimensional charge state distribution and its shape is affected by combination of gate voltages.

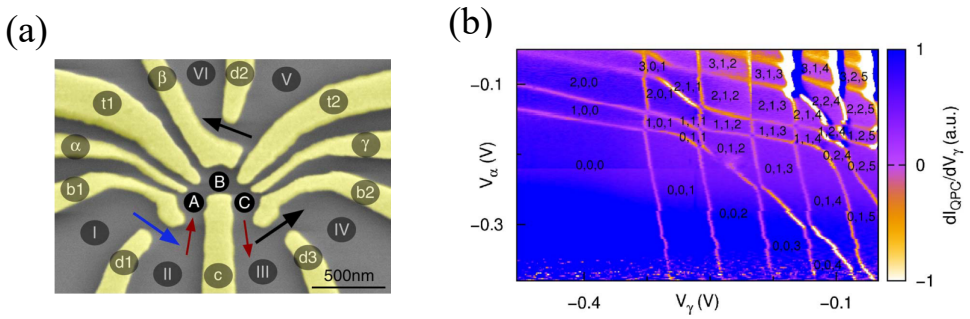

Figure 2.12: Linearly aligned TQD. (a) SEM image of TQD device [54]. Three QDs are formed the position shown as filled circle and they are named as QD_A, QD_B and QD_C. Charge states of three QD are modulated by voltage applied to plunger gate electrode α , β and γ, respectively. This device has three QPC charge sensors nearby each QD. (b) Stability diagram in V_α-V_γ voltage plane measured by charge sensor near QD_A. In each region, charge configuration of TQD is shown as (N_A, N_B, N_C) where N_i is the number of electron confined in QD_i.

Two-dimentipnal stability diagram Fig.2.12 (a) shows SEM image of TQD device. Three QDs are formed in the position shown as filled circle and named as QD_A, QD_B and QD_C. In such arrangement, neighboring QDs (QD_A and QD_B, QD_B and QD_C) are capacitively coupled but coupling between QDs in both ends of TQD array (QD_A and QD_C) is almost 0 due to large gate electrode c. This TQD array connect with electron reservoirs II and III via QD_A and QD_C. Electron exchanges with reservoirs happen only at these QDs and electron tunnelings between QD_B and reservoirs becomes second order process.

Fig.2.12 (b) shows the charge stability diagram in V_α-V_γ voltage plane. Due to capacitive coupling between QDs and gate electrodes, energy level of QD_A (QD_C) is affected strongly by V_α (V_γ) and almost unaffected by V_γ (V_α). Then, charge transition lines of QD_A and QD_C are observed as horizontal and vertical lines in V_α-V_γ voltage plane, respectively. In case of QD_B, its energy level is affected equally by both gate voltages and its charge transition lines have some slope in this voltage plane. This slope is defined by the ratio of capacitive couplings between QD_B and gate electrodes α and γ. In Fig.2.12 (b), QD_B equally couples with gate electrode α and γ, and the slope of charge transition line for QD_B is about -1. It also means QD_B is formed near the middle point between gate electrodes α and γ.

In the left-lower corner of diagram where any charge transition line is not ob-

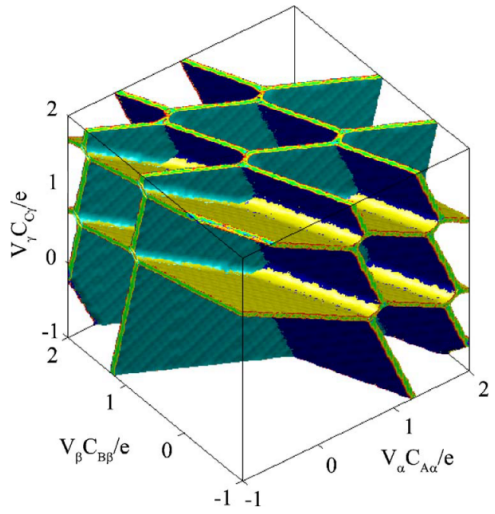

Figure 2.13: Three dimensional stability diagram measured in the TQD device shown in Fig.2.12 (a) [54].

served, it indicate all electrons are depleted from TQD structure. Charge configuration in each region can be identified by counting charge transition lines from this region. In the diagram, charge configuration identified above method are shown as N_{A}, N_{B}, N_{C} where N_i is number of electrons in QD_i.

At the cross-points of charge transition lines, anti-crossings are observed whose distance are affected by the capacitive coupling between respective QDs. Comparing the anti-crossings, in the condition of Fig.2.12 (b), the coupling between $\mathrm{QD_A}$ and $\mathrm{QD_B}$ is larger than that of $\mathrm{QD_B}$ and $\mathrm{QD_C}$. Tunnel couplings between the QDs can be estimated from the curvature of charge transition lines around triple point.

Three dimentional stability diagram The charge states of TQD spread three-dimensional space. Fig.2.13 shows the stability diagram in V_α-V_β-V_γ voltage space. In three-dimensional stability diagram, charge transitions occurs the voltage region shown as plane and triple points observed as lines. Two-dimensional stability diagram shown in Fig.2.12 (b) is a slice of this three-dimensional stability diagram. In multiple QD system from single to triple QD, charge states distribution can be visualized like two- or three-dimensional stability diagram. However, the charge states of larger multiple QD system, such as quadruple QD (QQD), distribute multi-dimensional space larger than three-dimension and its visualization

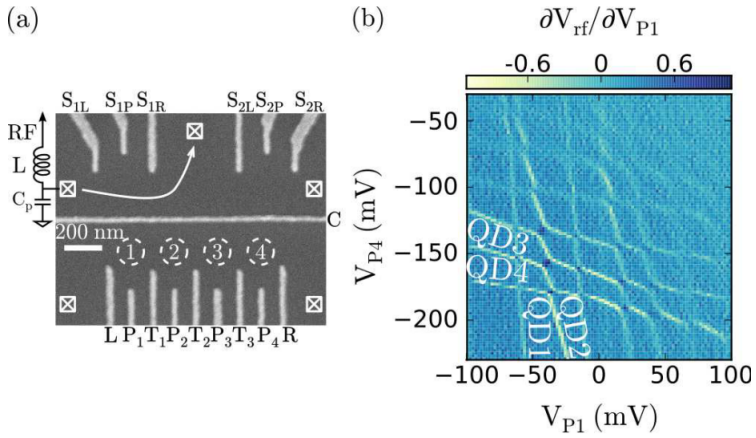

Figure 2.14: SEM image of QQD device (a) and stability diagram (b) [15]. (a) SEM image of QQD device used in [15]. Four tunnel-coupled QDs are formed linearly at the locations that are indicated by dashed white circles. They are named as QD_1, QD_2, QD_3 and QD_4 from left to right. Cross marks indicate Ohmic contacts. Two charge sensors are formed above the gate electrode C but only left charge sensor formed with gate electrodes S_{1L}, S_{1C} and S_{1R} is utilized here. Left charge sensor is connected with chip inductance L and parasitic capacitance between surrounding wires C_p and form tank circuit for RF reflectometry. (b) Charge stability diagram of QQD measuring left charge sensor signal in (a) as a function of plunger gate voltage of both ends od QQD array V_{P1} and V_{P4} (V_{P1}-V_{P4} voltage plane). The QQD empty state (0,0,0,0) is observed in the left lower corner.

become hard. At that case, charge state investigation and control needs improvement.

Charge Stability Diagram of Quadruple Quantum Dot

The charge states of QQD distributes four-dimensional space defined by gate voltages for each QD's energy levels. Full visualization of the charge states is impossible and improvement in measurement and control method is necessary.

Fig.2.14 (b) shows the charge stability diagram measured with a QQD device shown in Fig.2.14 (a). Four QDs, named as QD_1, QD_2, QD_3 and QD_4 from left to right, are linearly aligned and neighboring QDs are tunnel coupled each other in this device. Similar with TQD stability diagram, charge transition line for each QD have a slope defined by the aspect of capacitive couplings between

QD and modulating gate electrodes. In stability diagram in V_{P1}-V_{P4} plane shown in Fig.2.14, they have different slopes and can be distinguished as those of QD_1, QD_2, QD_3 and QD_4 from vertical to horizontal ones, respectively. By counting the charge transition lines from the QQD empty state observed in the left lower corner of Fig.2.14 (b), the charge configurations of QQD can be identified in any region. However, considering the application as four-spin qubit system, conventional control method that only uses one-voltage plane is insufficient and need improvement.

2.2 Spin States in Quantum Dots

Spin qubit systems based on multiple QD usually consists of an array of singly-occupied QDs. Investigation of energy levels of spin states is basic requirement for spin qubit initialization, readout and control. In this section, we describe spin states those are used for spin qubits in multiple QD.

2.2.1 Single-Electron Spin States

In non-magnetic semiconductors, electron-spins confined in QDs can be treated as independent quantum systems since interactions between them are very weak. The Zeeman Hamiltonian of a single spin in a QD under a magnetic field $\boldsymbol{B}$ is given by,

$$\mathcal{H}_{\mathrm{Z}} = \frac{g\mu_{\mathrm{B}}}{2}\boldsymbol{B}\cdot\boldsymbol{\sigma}, \tag{2.18}$$

where g is the Landé g-factor, μ_{B} is the Bohr magneton and σ_i ($i = x, y, z$) are the Pauli matrices. The spin up and down eigenstates, aligned to the direction of $\boldsymbol{B}$, are shifted by the Zeeman energy $E_{\mathrm{Z}} = |g|\mu_{\mathrm{B}}|\boldsymbol{B}|$. The spin precesses at the Larmor frequency $f_{\mathrm{L}} = |g|\mu_{\mathrm{B}}|\boldsymbol{B}|/h$, where h is Planck's constant, in the laboratory frame.

To investigate the spin dynamics, it is useful to take a reference frame rotating at an angular frequency ω. A superposition spin state in the reference frame $|\psi\rangle_{\mathrm{ref}}$ is given by $|\psi\rangle_{\mathrm{ref}} = U_\omega |\psi\rangle_{\mathrm{lab}}$, where $U_\omega = exp(\frac{i\omega t}{2}\sigma_{\mathrm{z}})$ and $|\psi\rangle_{\mathrm{lab}}$ is the superposition spin state in the laboratory frame. The time dependent Schrödinger equation in the laboratory frame is expected as

$$i\hbar\frac{\mathrm{d}}{\mathrm{d}t}(U_\omega^{-1}|\psi\rangle_{\mathrm{ref}}) = \mathcal{H}_{\mathrm{lab}}(U_\omega^{-1}|\psi\rangle_{\mathrm{ref}}). \tag{2.19}$$

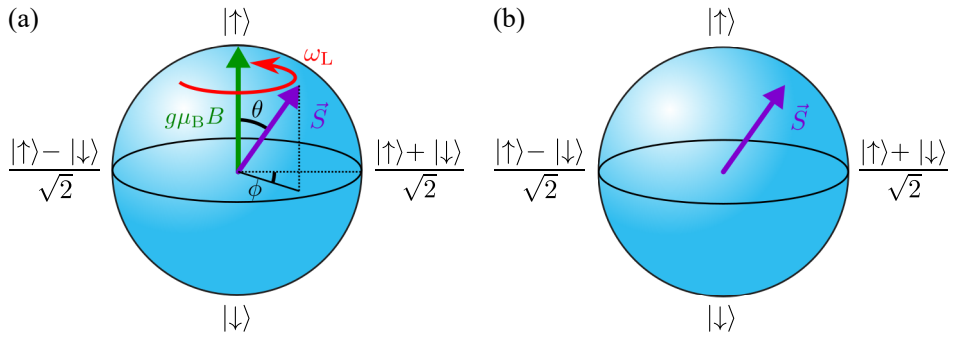

Figure 2.15: The Bloch sphere representation of a single spin. The direction of the magnetic field aligns the z-axis. A pure spin state can be depicted by a Bloch vector pointing to the surface of the sphere. The inclination from the z-axis θ is determined such that the spin up probability $P_{|\uparrow\rangle} = cos^2\theta$. The azimuthal angle ϕ corresponds to the relative phase between the spin up and down states. (a) Bloch sphere in laboratory frame. The Bloch vector shown as purple arrow precesses around the z-axis. (b) Bloch sphere in the reference frame rotating at the spin precession frequency. The Bloch vector appears static.

Then the spin dynamics in the reference frame is obtained as,

$$\mathcal{H}_{\mathrm{ref}} = U_\omega \mathcal{H}_{\mathrm{lab}} U_\omega^{-1} - \frac{\hbar\omega}{2}\sigma_{\mathrm{z}}. \tag{2.20}$$

When $\omega = 2\pi f_{\mathrm{L}}$, $\mathcal{H}_{\mathrm{ref}} = 0$ and no time evolution of the spin state takes place in the reference frame. Fig.2.15 shows the Bloch sphere representation of a single spin in (a) the laboratory frame and (b) reference frame [55].

2.2.2 Two-Electron Spin States

In two-electron spin states, spin-spin interactions, especially exchange coupling between QDs, play important roles in the entanglement control and two-qubit operation. The exchange coupling is strongly enhanced at the charge degeneracy of (1,1)-(2,0) and (1,1)-(0,2) in a DQD [25, 56].

To discuss the two-spin state in the vicinity of (1,1)-(2,0) charge degeneracy point, it is convenient to introduce the *level detuning*, ε as the difference of electrical potential between QDs. Here, we consider tunnel coupled DQD system and name two QDs as QD_1 and QD_2. Fig.2.16 (a) shows the stability diagram of DQD

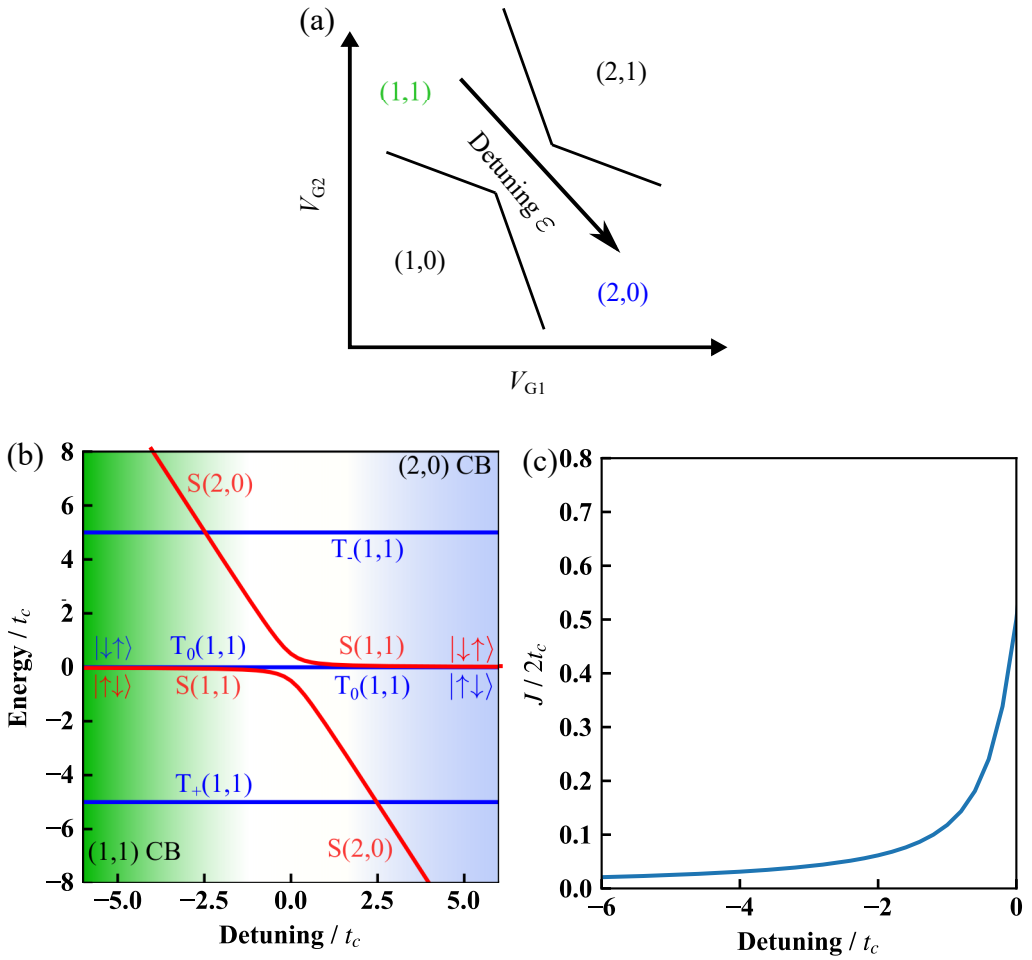

Figure 2.16: Energy level diagram of the two-electron spin states as a function of the detuning ε. (a) Schematic picture of DQD stability diagram around (1,1)-(2,0) charge transition. The black arrow shows the detuning axis. (b) Numerically calculated energy level diagram of the two-electron spin states as a function of ε. All parameters used in this calculation are normalized by t_{c}. The three blue lines show the (1,1) triplet states those are separated from each other by Zeeman energy $E_{\mathrm{Z}} = 10t_{\mathrm{c}}$ (assumed for the calculation). The two red lines show the (2,0) and (1,1) singlet states. These two states are hybridized by the inter-dot tunnel coupling $t_{[\mathrm{c}]}$ and form anti-crossing with $2\sqrt{2}t_{\mathrm{c}}$ at $\varepsilon = 0$. (c) J as a function of ε.

in $V_{\mathrm{G1}} - V_{\mathrm{G2}}$ voltage plane and ε-axis is defined as black arrow. Fig.2.16 (b) shows the numerically calculated energy level diagram as a function of ε. In the large ε, the electrostatic potential of the QD_1 decreases and the doubly-occupied state in the left QD becomes the ground state. Due to Pauli's exclusion principle, the symmetric spins must occupy excited orbital s in QD_1 and the spin state becomes singlet $|S(2,0)\rangle = (|\uparrow_1\downarrow_1\rangle - |\downarrow_1\uparrow_1\rangle)/\sqrt{2}$. The energy difference between localized singlet-triplet E_{ST} is normally much larger than other energies such as inter-dot tunnel coupling t_{c} and ε. Therefore, we only consider the singlet state for doubly-occupied charge state. In $\varepsilon = 0$ condition, the electrostatic potentials of both QD are aligned and hybridization between (1,1) and (2,0) charge states are enabled. In (1,1) charge state, singlet and triplet states are degenerated but inter-dot tunnelling process preserve spin state and hybridization with (2,0) state is only allowed with singly-occupied singlet state$|S(1,1)\rangle = (|\uparrow_1\downarrow_2\rangle - |\downarrow_1\uparrow_2\rangle)/\sqrt{2}$. Then, the Hamiltonian describing the tunnel coupling is expressed as

$$\mathcal{H}_{\mathrm{T}} = -\varepsilon|S(2,0)\rangle\langle S(2,0)| + \sqrt{2}t_{\mathrm{c}}(|S(2,0)\rangle\langle S(1,1)| + |S(1,1)\rangle\langle S(2,0)|). \tag{2.21}$$

This hybridization decreases the energy of $|S(1,1)\rangle$ by the exchange energy $J/2$. Then, J is a function of ε and t_{c} shown in Fig.2.16 (c) and given by,

$$J(\varepsilon, t_{\mathrm{c}}) = \sqrt{\varepsilon^2 + 8t_{\mathrm{c}}^2}. \tag{2.22}$$

In the largely negative ε region where charge state is in the deep Coulomb blockade of (1,1), Eq.2.21 is well approximated by the Heisenberg Hamiltonian, $J\mathbf{S}_1 \cdot \mathbf{S}_2$, where $\mathbf{S}_{1(2)}$ is the spin operator of $\mathrm{QD}_{1(2)}$. Then, the effective Hamiltonian of the two-electron spin is given by

$$\begin{aligned}\mathcal{H} = -J(\varepsilon)|S(1,1)\rangle\langle S(1,1)| + \Delta E_{\mathrm{Z}}(|\uparrow_1\downarrow_2\rangle\langle\downarrow_1\uparrow_2| - |\downarrow_1\uparrow_2\rangle\langle\uparrow_1\downarrow_2|) \\ + E_{\mathrm{Z},0}(|T_+(1,1)\rangle\langle T_+(1,1)| - |T_-(1,1)\rangle\langle T_-(1,1)|),\end{aligned} \tag{2.23}$$

where ΔE_Z is the difference of Zeeman energy between the two QDs and $E_{\mathrm{Z},0}$ is the average Zeeman energy of the two QDs. $|T_\pm(1,1)\rangle$ are the triplet substates with parallel spins. In the experiments, a large magnetic field is usually applied so that these triplet states are energetically separated from $S_z = 0$ states. These remaining $S_z = 0$ states,$|\uparrow\downarrow\rangle$ and $|\downarrow\uparrow\rangle$ form a subspace and we can use it to form qubit (*Singlet-Triplet* (ST) qubit). Here J and ΔE_{Z} compete with each other as shown in Fig.2.17.

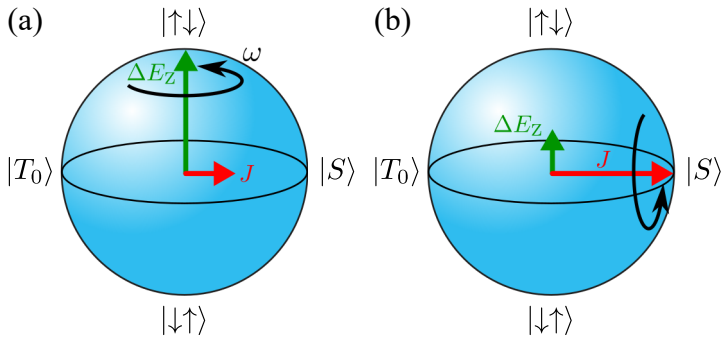

Figure 2.17: The Bloch sphere representation of a two-spin system in the $S_z = 0$ subspace. (a) For ΔE_{Z} much larger than J, the Bloch vector precesses around ΔE_{Z} and $|\uparrow\downarrow\rangle$ and $|\downarrow\uparrow\rangle$ becomes good eigenstates. (b) For J much larger than ΔE_{Z},, the vector precesses around the J axis and $|S\rangle$ and $|T_0\rangle$ becomes eigenstates.

2.2.3 Three-Electron Spin States

The discussion on the two-spin states in above section can be extended to a three-spin system in TQDs. Especially in linearly-coupled TQDs, single spins in respective QDs are coupled by the nearest neighbor exchange interactions J_{ij} between QD_i and QD_j where $(i, j) = (1, 2), (2, 3)$. These exchange energies are similarly enhanced near the charge degeneracy point between (1,1,1) and (2,0,1) or (1,0,2). Fig.2.18 (a) shows schematic picture of the stability diagram of TQD in the vicinity of (1,1,1) and (2,0,1) or (1,0,2) degeneracy point. Here, ε axis is defined as the energy difference between the electrostatic potentials of $\mathrm{QD_L}$ and $\mathrm{QD_R}$ and a black arrow in Fig2.18 (a) shows one of ε axis that does not detune energy level of $\mathrm{QD_C}$. In $\varepsilon = 0$ condition, all electrostatic potential of TQD are aligned and (1,1,1) charge states becomes the ground states. In negative (positive) ε, electrostatic potential of the $\mathrm{QD_L}$ ($\mathrm{QD_R}$) decreases and the (2,0,1) ((1,0,2)) charge state becomes the ground state.

Similar with DQD case, the exchange couplings and the local Zeeman energy differences compete with each other. When the exchange couplings are dominant, the eight eigenstates of (1,1,1) charge state are four quadruplets $Q_{\mathrm{S_z}}$ with the total spin $S = 3/2$ which are not affected by ε (triplet-like states) and four doublets $D^{\pm}_{\mathrm{S_z}}$ with $S = 1/2$ which depend on ε (singlet-like states). The explicit forms of these states without normalization are written as follows,

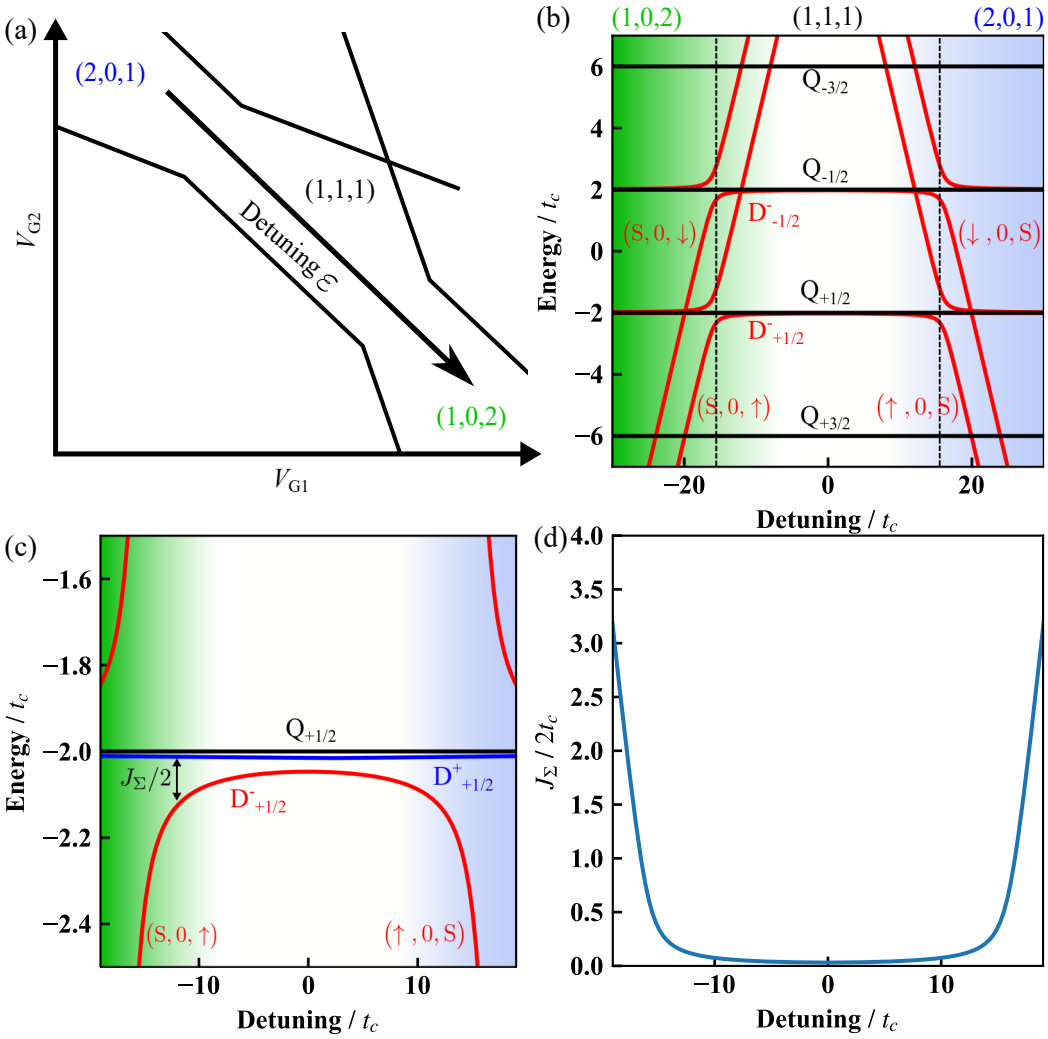

Figure 2.18: Energy level diagram of three-electron spin states in TQD. (a) Schematic picture of stability diagram of TQD in V_{G1}-V_{G3} voltage plane around (2,0,1), (1,1,1) and (1,0,2) charge states. The diagonal arrow shows detuning ε axis. (b) The energy level diagram of three-electron spin states as a function of ε. All parameters used in this calculation are normalized by $t_C (= t_{LC} = t_{CR}$, assuming symmetric inter-dot couplings.) The boundary between (1,1,1) and (1,0,2) or (2,0,1) charge states is located at $\varepsilon = 15t_C$ or $-14t_C$ shown as black dotted lines. (c) Enlarged diagram of (b) around $Q_{+1/2}$. The three states with $S_z = 1/2$ are energetically separated due to the exchange-interaction. (d) Energy difference between $D^-_{+1/2}$ and $D^+_{+1/2}$ (J_Σ) as a function of ε. J_Σ decreases when moving into the center of CB of (1,1,1) charge state ($\varepsilon = 0$). Therefore, the three-spin eigenstates deep in (1,1,1) are determined by the Zeeman Hamiltonian, not the exchange coupling.

$$
\begin{aligned}
Q_{+3/2} =& |\uparrow\uparrow\uparrow\rangle \\
Q_{+1/2} =& |\uparrow\uparrow\downarrow\rangle + |\uparrow\downarrow\uparrow\rangle + |\downarrow\uparrow\uparrow\rangle \\
Q_{-1/2} =& |\downarrow\downarrow\uparrow\rangle + |\downarrow\uparrow\downarrow\rangle + |\uparrow\downarrow\downarrow\rangle \\
Q_{-3/2} =& |\downarrow\downarrow\downarrow\rangle \\
D^{\pm}_{+1/2} =& (J_{12} - J_{23} \pm J_{\Sigma}) |\uparrow\uparrow\downarrow\rangle + (J_{23} \mp J_{\Sigma}) |\uparrow\downarrow\uparrow\rangle - (J_{12}) |\downarrow\uparrow\uparrow\rangle \\
D^{\pm}_{-1/2} =& (J_{12} - J_{23} \pm J_{\Sigma}) |\downarrow\downarrow\uparrow\rangle + (J_{23} \mp J_{\Sigma}) |\downarrow\uparrow\downarrow\rangle - (J_{12}) |\uparrow\downarrow\downarrow\rangle
\end{aligned} \tag{2.24}
$$

where $J_{\Sigma} = \sqrt{J_{12}^2 + J_{23}^2 - J_{12}J_{23}}$. Fig.2.18 (b) shows the energy level diagram of twelve states as a function of ε.The four black solid lines indicate (1,1,1) $Q_{\mathrm{S_z}}$ separated from each other by Zeeman energy $E_{\mathrm{Z}} = 10t_{\mathrm{C}}$ (assumed for calculation). The six red lines indicate the two $D^{\pm}_{\pm 1/2}$ and four doubly-occupied singlet states, (S,0,$\sigma_{\mathrm{z,R}}$) and ($\sigma_{\mathrm{z,L}}$,0,S) where $\sigma_{\mathrm{z,i}} = \uparrow$ or $\downarrow$. At the boundary between (1,1,1) and (2,0,1) or (1,0,2) charge states (shown as black dashed lines in Fig.2.18 (b)), the doubly-occupied singlet states and $D^{\pm}_{\mathrm{S_z}}$ generate the hybridized states energetically separated by $2\sqrt{2}t_{\mathrm{C}}$ due to the inter-dot tunnel coupling. Fig.2.18 (c) shows the enlarged energy level diagram of Fig.2.18 (b) around $S_{\mathrm{z}} = 1/2$. $D^{\pm}_{+1/2}$ can be used as a qubit (*exchange-only qubit*) [57, 58] under an external magnetic field which energetically separates these two states from others.

When the local Zeeman energy differences $\Delta E_{\mathrm{Z,12}}$ and $\Delta E_{\mathrm{Z,23}}$ are dominant, the eigenstates are approximated by those of the Zeeman Hamiltonian, $\sigma_{\mathrm{z,i}}$ (i=L, C, R). This condition is achieved in $\varepsilon = 0$ where (1,0,2) and (2,0,1) are energetically separated and the exchange couplings decreases as shown in Fig.2.18 (d).

2.3 Spin State Initialization and Readout

The readout of single-spin state is an essential technique for spin qubit experiments. However, the direct measurement of single spin states is normally difficult because the magnetic moment of single electron spins is too small to detect directly. Nevertheless, some spin state readout methods are established by combining the charge sensing and spin-to-charge conversion. In this section, we will review these techniques and also the spin state initialization schemes.

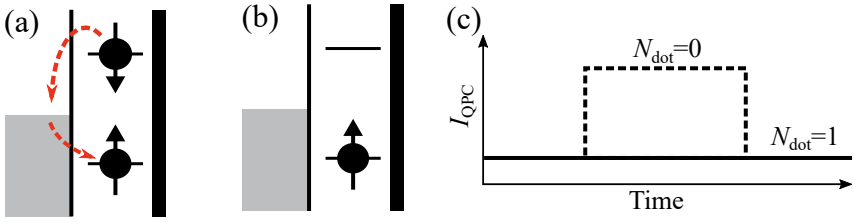

Figure 2.19: Electron exchange between the QD and the adjacent reservoir. (a) Schematic image of the energy level in the readout stage when the initial spin state is the excited state with down spin. The electron can tunnel out from the QD and then another electron with up spin enters the QD to occupy ground state. (b)Schematic image of the energy level as same as (a) but the initial spin state is the ground state with up spin. The charge state in unchanged. (c) Real-time change of the charge sensor current I_{QPC} for (a) (broken line) and (b) (solid line).

2.3.1 Electron Exchange between Quantum Dots and Leads

The first method uses the energy-selective spin state readout. In this scheme, a large external magnetic field is applied to make Zeeman energy larger than the thermal energy $k_{\mathrm{B}}T_{\mathrm{e}}$ in the reservoirs (T_{e} is the electron temperature). Then, to perform spin state readout, the electrochemical potential of the QD is tuned so that only the ground state with up spin is under the Fermi level of the reservoir. If an electron occupies the excited state with down spin, then it tunnels out to the reservoir and other electron enters the QD to form the ground state. If an electron occupies the ground state with up spin, the electron tunnelling is forbidden (see Figs.2.19(a) and (b)). This single-electron tunnelling process can be detected by monitoring a charge sensor Fig.2.19 (c). Utilizing this technique, single-shot readout of single spins [59], independent two spin readout in DQD [60] and a sequential readout of three spins using a single reservoir [61] are realized.

This scheme requires large Zeeman energy compared to the thermal energy. Since the Zeeman energy is usually a few tens of GHz in experiments, low electron temperature ($\preceq 100mK$) is necessary for high fidelity readout. In addition to this, the tunnel rate between the QD and the adjacent reservoir has to be adjusted to an appropriate value in order to detect the real-time tunnelling (see Fig.2.19(c)).

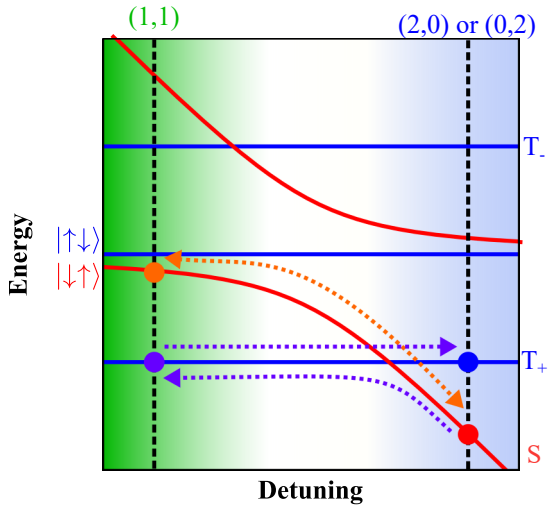

Figure 2.20: Energy level diagram of two-electron spin state as a function of ε defined in Fig.2.16. This diagram is numerically calculated as same as Fig.2.16 (b) but the parameter for Zeeman energies in QDs are changed to $E_{\mathrm{Z}} = t_{\mathrm{C}}$. The red curves are for the hybridized singled states due to the inter-dot tunnel coupling, while the blue curves are for the Zeeman-split triplet states (singly occupied).

2.3.2 Pauli Spin Blockade

Since electron spin is generally preserved in the tunneling process, there are some conditions where an electron tunneling process becomes spin-dependent. One of the prominent examples is the Pauli Spin Blockade (PSB), where the inter-dot electron transport is forbidden by Pauli exclusion principle. It was first observed in GaAs vertical DQDs [5] and later in various DQD systems including GaAs lateral DQDs [62–64].

The PSB effect is often observed in DQDs by using voltage pulse operation. Here for simplicity, we consider the PSB observed in DQD with voltage pulse method. To understand this scheme, the energy level diagram of two-electron spin states shown in Fig.2.20 is helpful. In this scheme, spin initialization is started by waiting at negative ε region where S(2,0) state becomes the ground state. This waiting time has to be longer than the spin relaxation time T_1 but it can be shortened to tune the voltage condition nearby the charge transition line of the left QD where electron exchange between the QD and adjacent reservoir happens in tunnel rate. Then one of electrons is transferred to the other QD to form (1,1) charge state (negative ε). In this detuning ramp, the ground state undergoes two anti-crossings.

The first is between singlet and triplet+ states mediated by the local in-plane magnetic field difference between neighboring QDs [65, 66] with anti-crossing size Δ_{ST_+}. The second is between the singlet states of (1,1) and (2,0) charge states hybridized by the inter-dot tunnel coupling t_{C}. By changing the rate of ramping the detuning across each anti-crossing, we can prepare and measure the two-spin state of interest. If the detuning ramp sufficiently slow or is adiabatic at the first anti-crossing, two-electron spin state is initialized to T_+ (purple dashed arrow in Fig.2.20). If the detuning ramp is non-adiabatic or to the first anti-crossing but adiabatic for the second one as long as the ramp rate $\ll |g|\mu_{\mathrm{B}}\Delta B_{\mathrm{Z}}/h$, two-spin state is initialized to $|\downarrow\uparrow\rangle$ which is an eigenstate determined by the local Zeeman energies (orange dashed arrow in Fig.2.20). This so-called slow adiabatic passage is also utilized to spin readout not only two-spin state initialization. If two-spin state is $|\downarrow\uparrow\rangle$ in (1,1) charge state, the slow adiabatic passage to the reverse direction results the hybridized singlet state in (2,0) charge state. If two-spin state is one of triplet states, above passage results the triplet state and block the electron tunneling due to Pauli exclusion rule. These spin dependent electron tunneling from (1,1) to (2,0) or (0,2) can be detected by charge sensors.

2.4 Single Qubit operation

Single qubit operations requires control of the spin state about two independent axes. For the single spin qubit, this is commonly achieved via via electron spin resonance (ESR) technique. Here we describe a basic theory of ESR and several schemes for implementing ESR.

2.4.1 Theoty of Electron Spin Resonance

ESR is a magnetic resonance induced by oscillating magnetic field with resonant frequency f_{ESR} which is orthogonal to the static magnetic field B_{ext}. Electron spin states $|\uparrow\rangle$ and $|\downarrow\rangle$ under $B\mathrm{ext}lz$ are energetically split by the Zeeman energy $|g|\mu_{\mathrm{B}}|B_{\mathrm{ext}}|$ and the state precesses aroun the z axis with the Larmor frequency $f_{\mathrm{L}} = |g|\mu_{\mathrm{B}}|B_{\mathrm{ext}}|/h$. When we apply an magnetic field oscillating in the x-direction with a frequency $\omega \sim f_{\mathrm{L}}/2\pi$ with an amplitude $B_{\mathrm{a.c.}}$, the time-dependent Hamiltonian of the spin is given by

$$\mathcal{H}_{\mathrm{lab}} = \frac{g\mu_{\mathrm{B}}B_{\mathrm{ext}}}{2}\sigma_{\mathrm{z}} + \frac{g\mu_{\mathrm{B}}B_{\mathrm{a.c.}}}{2}\cos(\omega \mathrm{t} + \varphi)\sigma_{\mathrm{x}} \tag{2.25}$$

where φ is the phase of $B_{\mathrm{a.c.}}$ at $t = 0$. In the reference frame rotating at the frequency $\omega/2\pi$, this equation becomes simpler and clearer. From Eq.2.25, the corresponding Hamiltonian becomes

$$\mathcal{H}_{\mathrm{ref}} = -\frac{\hbar\delta}{2}\sigma_z + \hbar\omega_{\mathrm{R}}\cos(\omega \mathrm{t} + \varphi)[\cos(\omega \mathrm{t})\sigma_{\mathrm{x}} - \sin(\omega \mathrm{t})\sigma_{\mathrm{y}}], \tag{2.26}$$

where $\delta/2\pi = \omega/2\pi - f_{\mathrm{L}}$ is the frequency detuning from the resonance condition and $\omega_{\mathrm{R}} = |g|\mu_{\mathrm{B}}B_{\mathrm{a.c.}}/2\hbar$.

Eq.2.26 includes the term which oscillate at 2ω, however, these terms do not contribute much to the spin dynamics in the regime of experimental interest where $\omega \gg \omega_{\mathrm{R}}$ is satisfied. This is because the time evolution oscillating at 2ω is averaged out in the timescale of the vertical spin rotation $2\pi/\omega_{\mathrm{R}}$. Rotating wave approximation neglects these terms and the effective Hamiltonian is simplified to
,

$$\mathcal{H}_{\mathrm{ref}} \approx -\frac{\hbar\delta}{2}\sigma_z + \frac{\hbar\omega_{\mathrm{R}}}{2}[\cos(\varphi)\sigma_{\mathrm{x}} + \sin(\varphi)\sigma_{\mathrm{y}}] \equiv \mathcal{H}_{\mathrm{ESR}}. \tag{2.27}$$

Under $\mathcal{H}_{\mathrm{ESR}}$, the spin rotates around the axis of $(x, y, z) = (\omega_{\mathrm{R}}\cos\varphi, \omega_{\mathrm{R}}\sin\varphi, -\delta)$ at a frequency $\sqrt{\omega_{\mathrm{R}}^2 + \delta^2}/2\pi$ in the reference frame as shown in Fig.2.21 (a). Especially in the ESR resonance condition where $\delta = 0$ ($\omega = 2\pi f_{\mathrm{L}}$), spin will flip completely with a Rabi frequency $\omega_{\mathrm{R}}/2\pi$. The rotation axis can be chosen arbitrarily in xy plane by changing the initial phase φ and therefore ESR enables arbitrary single qubit operation.

Under ESR drive, the spin dynamics is coherent oscillation between $|\uparrow\rangle$ and $|\downarrow\rangle$. The ESR time t_{ESR} dependence of the spin flip probability is given by the Rabi formula,

$$P_{\mathrm{flip}} = \frac{\omega_{\mathrm{R}}^2}{2\Omega_{\mathrm{R}}^2}[1 - \cos(\Omega_{\mathrm{R}}\mathrm{t}_{\mathrm{ESR}})], \tag{2.28}$$

where $\Omega_{\mathrm{R}} = \sqrt{\omega_{\mathrm{R}}^2 + \delta^2}$ is the generalized Rabi frequency. Fig.2.21 (b) shows a characteristic Chevron pattern obtained by the spin flip probability as a function of t_{ESR} and δ.

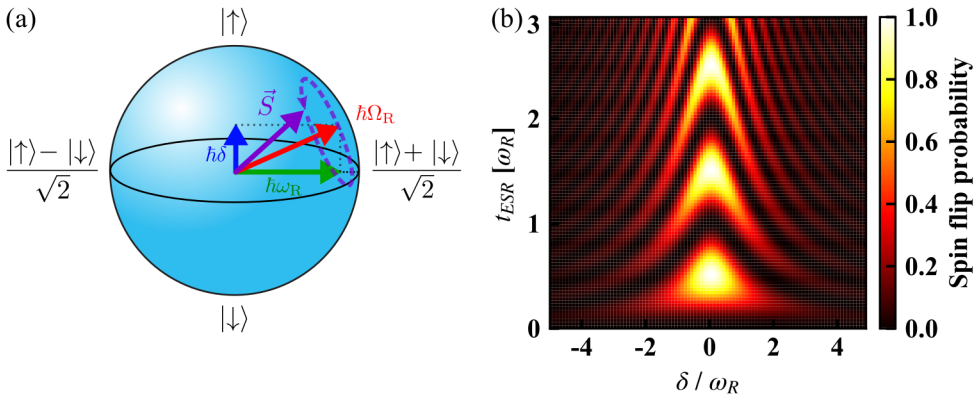

Figure 2.21: (a) Schematic image of the spin dynamics under $\mathcal{H}_{\mathrm{ESR}}$ in the rotating frame at the frequency of the oscillating field. The frequency detuning δ is expressed as the vector pointing in the z direction with $\hbar\delta$ in energy (blue arrow). The oscillating field is shown as one pointing in the x direction with $\hbar\omega_{\mathrm{R}}$ in energy(green arrow). The rotation axis and frequency is given by the sum of these contributions (red arrow). (b) Chevron pattern of spin flip probability as a function of $\delta/\omega_{\mathrm{R}}$ and ESR drive time t in unit of $2\pi/\omega_{\mathrm{R}}$

2.4.2 Micro-Magnet Electron Spin Resonance

ESR requires two different magnetic field, a static and an oscillating magnetic fields perpendicular to each other. In the low temperature experiment, it is challenging to apply a high-frequency effective magnetic field to the QDs. The first attempt of single ESR in QD was achieved by injecting an a.c. current to an on-chip coil [67] but this scheme is not appropriate to realize fast spin rotation because a strong oscillating field for the fast spin rotation causes Joule heating. In addition, the oscillating field created by the on-chip coil cannnot be restricted to only one of the multiple QD and individual control of electron spins is difficult. Therefore, electrically driven ESR schemes have been investigated which can be more localized and free from the Joule heating. However, electric fields do not directly couple to electron spin and indirect coupling mechanisms are required to drive ESR electrically [68]. One of the mediation mechanisms is to utilize a slanting magnetic field created by proximal micro-magnets (MMs) [27, 69] (Fig.2.22 (d)). This scheme solves above two problems in on-chip coil scheme as mentioned below.

Here, we review tha teory of MM-ESR method [69]. Assuming that a time-dependent electric field $\boldsymbol{E}(t)$ is applied to the electron confined in a QD with a harmonic potential $V(\boldsymbol{r}) = m^*\omega_0^2(y^2+z^2)/2$ and an un-uniform static magnetic field $\boldsymbol{B}(\boldsymbol{r})$. Here, m^* is the effective mass of an electron in the QD. The Hamiltonian of the system in the laboratory frame is written as

$$\mathcal{H}_{\rm lab} = \frac{\boldsymbol{p}^2}{2m^*} + V(\boldsymbol{r}) + e\boldsymbol{E}(t)\cdot\boldsymbol{r} + \frac{g\mu_{\rm B}\boldsymbol{B}(\boldsymbol{r})\cdot\boldsymbol{\sigma}}{2}. \tag{2.29}$$

Consider a local magnetic field whose x component is slanted in the z direction which satisfies Maxwell's equation as

$$\boldsymbol{B}(\boldsymbol{r}) = \boldsymbol{B}(x,z) = (B_0 + b_{\rm sl}x)\hat{z} + (B_x + b_{\rm sl}z)\hat{x}, \tag{2.30}$$

where B_0 is the magnetic field component parallel to $\parallel \hat{z}$. Assuming strong confinement of the electron in the x direction which is perpendicular to the 2DEG, the term $b_{\rm sl}x\hat{z}$ can be neglected. Since the B_x is normally much smaller than B_0 in the experiment, it only modifies the quantization axis. A crucial role is played b ythe term $b_{\rm sl}z\hat{x}$ which mixes the charge and the spin degrees of freedom via the last term in Eq.2.30.

When an oscillating electric field $E_z(t) = E_{\mathrm{a.c.}}\sin(\omega \mathrm{t})$ is applied in the z direction at a frequency of $\omega/2\pi$, Eq.2.30 is written as

$$\mathcal{H}_{\mathrm{lab}} = \mathcal{H}_0 + \mathcal{H}_{\mathrm{mix}} + \mathcal{H}_{\mathrm{exc}}(t) \tag{2.31}$$

$$\mathcal{H}_0 = \frac{\boldsymbol{p}^2}{2m^*} + V(\boldsymbol{r}) + \frac{g\mu_{\mathrm{B}}B_0}{2}\sigma_z \tag{2.32}$$

$$\mathcal{H}_{\mathrm{mix}} = \frac{g\mu_{\mathrm{B}}b_{\mathrm{sl}}z}{2}\sigma_x \tag{2.33}$$

$$\mathcal{H}_{\mathrm{exc}}(t) = eE_{\mathrm{a.c.}}\sin(\omega t)z. \tag{2.34}$$

Since $\mathcal{H}_0$ does not mix the orbital and the spin degree of freedom, the eigenstates $|m, n; \sigma_z\rangle$ and their eigenenergies $\varepsilon_{m,n;\sigma_z}$ can be expressed as

$$\langle y, z|m, n; \sigma_z\rangle = \phi_m(y)\phi_n(z)\psi_{\sigma_z}, \tag{2.35}$$

$$\varepsilon_{m,n;\sigma_z} = \hbar\omega_0(m + n + 1) + \frac{g\mu_{\mathrm{B}}B_0}{2}\sigma_z, \tag{2.36}$$

where $\phi_m(y)$ and $\phi_n(z)$ are the orbital eigenstates in the harmonic potential, and ψ_{σ_z} is the spinor whose eigenvalues are ± 1. Here, the Zeeman energy $|g|\mu_{\mathrm{B}}B_0$ is much smaller than the level spacing $\hbar\omega$.

The perturbation of $\mathcal{H}_{\mathrm{mix}}$ mixes the orbital and the spin degree of freedom. The hybridized two lowest levels can be expressed as pseudo-spins $|\sigma_{\mathrm{p}}\rangle$. By calculating the eigenstates and the eigenenergies of $\mathcal{H}_0 + \mathcal{H}_{\mathrm{mix}}$ up to the first order in the characteristic coupling energy $E_{\mathrm{sl}} \equiv g\mu_{\mathrm{B}}b_{\mathrm{sl}}\sqrt{\hbar/m^*\omega_0}$ as,

$$|\sigma_{\mathrm{p}}\rangle = |0, 0; \sigma_{\mathrm{z}}\rangle - \sum_{n>0} \frac{g\mu_{\mathrm{B}}b_{\mathrm{sl}}/2\,\langle 0, n|\, z\,|0, 0\rangle}{n\hbar\omega_0 - g\mu_{\mathrm{B}}B_0\sigma_z}\,|0, n; -\sigma_z\rangle\,. \tag{2.37}$$

Assuming the symmetric confinement potential where $\langle m, n|\, z\,|m, n\rangle = 0$, there is no correction of the eigenenergies in the leading order of E_{sl}.

From here, we can include the effect of the oscillating electric field onto the pseudo-spin. The diagonal elements of $\mathcal{H}_{\mathrm{exc}}$ become 0 up to the first order in E_{sl} by assuming the symmetric confinement potential and the linearity of the slanting magnetic field. The non-diagonal elements are calculated as $\langle -\sigma_{\mathrm{p}}|\,\mathcal{H}_{\mathrm{exc}}\,|\sigma_{\mathrm{p}}\rangle = \frac{g\mu_{\mathrm{B}}B_{\mathrm{a.c.}}}{2}\sin(\omega \mathrm{t}) + \mathcal{O}(\mathrm{E_{sl}})^2$. Here, the amplitude of the affective magnetic field is written as

$$B_{\mathrm{a.c.}} = -\sum_{n>0} \frac{2n\hbar\omega b_{\mathrm{sl}} e E_{\mathrm{a.c.}}}{(n\hbar\omega)^2 - (g\mu_{\mathrm{B}}B)^2} |\langle 0,0|\, z\, |0,n\rangle|^2 \approx -\frac{eE_{\mathrm{a.c.}} b_{\mathrm{sl}}}{m^*\omega^2}. \tag{2.38}$$

The effective Hamiltonian of the pseudo-spin is written by

$$\mathcal{H}_{\mathrm{lab}} = \hbar\omega_0 \sigma_{\mathrm{p0}} + \frac{g\mu_{\mathrm{B}}B_0}{2}\sigma_{\mathrm{p}z} + \frac{g\mu_{\mathrm{B}}B_{\mathrm{a.c.}}}{2}\sigma_{\mathrm{p}x} \tag{2.39}$$

up to leading order of E_{sl} where σ_{pi} is the Pauli matrices of the pseudo-spin. This is equivalent to the ESR Hamiltonian in Eq.2.25 up to overall energy shift, and it indicates that ESR can be driven in an electric manner in a slanting magnetic field.

Eq.2.39 also suggests that the spin rotation speed is in proportion to the slanting field. In addition, the local magnetic field created by MM can modify B_0 at the dot position B_z and shift the ESR resonance conditions [27, 70]. These two parameters of the local magnetic field are important for the demonstration of fast and individual spin rotation with the MM-ESR. Fig.2.22 (a) shows the SEM image of the DQD device with MM whose design is optimized for fast and individual control of spin. The U-shaped MM shown as yellow shaded region realize large slanting field (Fig.2.22 (b)) and large difference of B_z between the QDs (Fig.2.22 (c)) simultaneously [71]. In this device, over 100MHz fast spin rotation and the individual control of electron spins in DQDs are realized [34]. This MM design can be extended larger multiple QD system liken TQD and individual control of electron spins are realized [17].

2.5 Two-Qubit operation

Two-qubit entangling operation is another key techniques for the universal gate operation since the combination of single- and entangling operations realizes it. For single spin qubits, the two-qubit operations is achieved using the exchange interaction between spins in neighboring dots [23, 72]. This can be easily seen by rewriting the exchange term $-J\,|S\rangle\langle S|$ in Eq.2.23 as $J(\varepsilon)(|\uparrow\downarrow\rangle\langle\downarrow\uparrow| + |\downarrow\uparrow\rangle\langle\uparrow\downarrow| + |\mathrm{T}_+\rangle\langle\mathrm{T}_+| + |\mathrm{T}_-\rangle\langle\mathrm{T}_-|)$, ignoring the global shift in energy. As discussed in §2.2.2, $J(\varepsilon)$ can be switched by quick modulation of ε (see Fig.2.22). The SWAP operation can be performed by starting from deep in the Coulomb blockade regime with $J \ll \Delta E_{\mathrm{Z}}$ where the eigenstates are $|\uparrow\downarrow\rangle$ and $|\downarrow\uparrow\rangle$ for the $S_z = 0$ subspace and then activating activating J with the condition of $J \gg \Delta E_{\mathrm{Z}}$ for a time

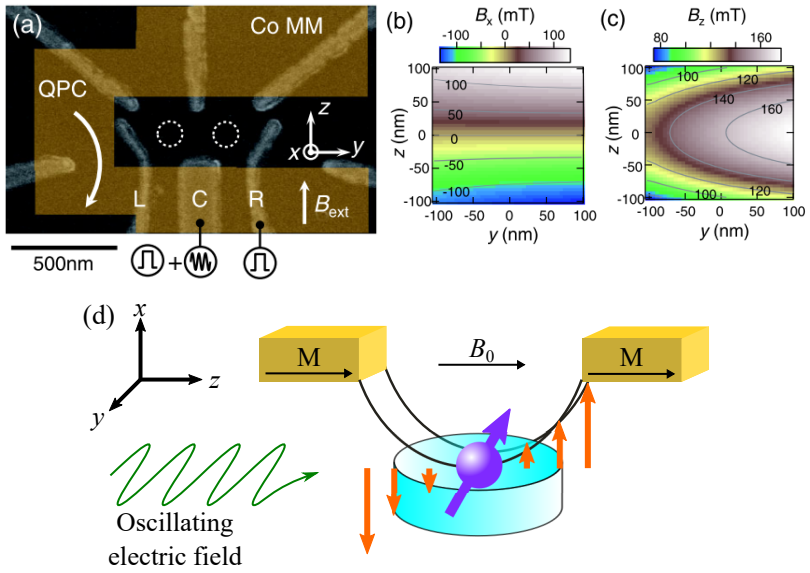

Figure 2.22: Device structure and simulated stray fields for MM-ESR. (a) The SEM image of the DQD device used to demonstrate fast and individual spin rotation [34]. The yellow shaded region shows the MM consisted by Co placed on top of the device with an 80nm thick insulator in between. (b) Numerically simulated distribution of the x component of the stray field B_x created by the MM shown in Fig.(a) [34]. The origin of the QD plane is chosen at the center of the two QDs. (c) Numerically simulated distribution of the z component of the stray field B_z [34]. (d) The schematic image of the device configuration for MM-ESR. The MM is fabricated on top of the QD device with an insulator in between and magnetized by the external magnetic field B_0 in the z direction. It is so designed that the out-of-plane (x) component of the stray field is slanted at the QD position. The slanting field, $b_{\rm sl} = \mathrm{d}B_x/\mathrm{d}z$, couples the orbital and the spin states of electron. An oscillating electric field is applied in the z direction to drive ESR.

$t_{\mathrm{SWAP}} = h/2J$ [25]. The maximally entangling gate $\sqrt{\mathrm{SWAP}}$ can be obtained by reducing the interaction time t_{SWAP} to the half.

2.6 Source of Decoherence

All qubits interact with their environments which leads to information loss [73] and it is assumed to be one of the central problems in implementing quantum computation. To correct the lost qubit information, implementing error correction codes is on eof the main motivation in this research. This section reviews the source of decoherence of single spin qubits in GaAs QDs.

Decoherence can be generally categorized into two general types [55,74]. The first type is energy relaxation caused by the qubit evolution toward thermodynamic equilibrium by transferring energy to the environment. The characteristic time T_1 is called the *energy relaxation time*. The second type is phase relaxation (*decoherence*) where the qubit loss phase information through interactions with the environment, wile preserving energy. The time constant of this phase randomization process, T_2, is called the (*intrinsic*) *phase coherence time*. The loss of phase information becomes quicker when the average is taken over ensembles in an inhomogeneous environment, which is the case for real experiment. This characteristic time T_2^*, called *ensemble phase coherence time*, gives the decay time of the ensemble qubit phase.

Relaxation and decoherence can be caused by many different sources such as the charge noise generated by the background moving charges [75, 76], lattice vibrations, fluctuating magnetic impurities, thermal and spurious noises from electrical circuits, and nuclear spin bath fluctuations [12, 77]. Qubit coherence is strongly affected by the spectrum and dynamics of relevant noise sources and the system Hamiltonian [78]. The main limitation of T_1 is caused by spin-orbit interaction (SOI) combined with phonon coupling [12]. On the other hand, $T_2^*$is limited by the nuclear field fluctuation through the hyperfine coupling in the environment [12].

2.6.1 Spin-Orbit Intereaction in Quantum Dots

For electrons in a 2DEG formed in III-V semiconductors, there are two main sources of SOI, the Dresselhaus term which is present in crystals with bulk inversion asymmetry [79] and the Rashba term which results from the structural inversion asymmetry [80, 81]. Since the SOI length ($\sim 100\mu$m) is much larger

than the size od GaAs QDs (typically ~ 100nm), the SOI effect can be treat as a perturbation. The eigenstates become admixtures of spin and orbital states [82]. The two lowest pseudo-spin states up to the leading order are

$$|\sigma_{\rm z}\rangle_{\rm p} = |0,0;\sigma_{\rm z}\rangle + \sum_{(m,n)\neq(0,0)} \frac{\langle m,n;-\sigma_{\rm z}|\,\mathcal{H}_{\rm SO}\,|0,0;\sigma_{\rm z}\rangle}{E_{0,0}-E_{m,n}-E_{{\rm Z},\sigma_{\rm z}}}\,|m,n;-\sigma_{\rm z}\rangle\,, \quad (2.40)$$

where $\mathcal{H}_{\rm SO}$ is the spin-orbit Hamiltonian, and quantum numbers m and n characterize the orbitals in the QD. Due to the SOI effect, these pseudo-spin states are susceptible to the electrical noise. The spin flipping process requires energy dissipation to the environment produced predominantly by phonons. From the Fermi's golden rule, T_1 is

$$\frac{1}{T_1} = \frac{2\pi}{\hbar}\left[\langle\uparrow|_{\rm p}\,\mathcal{H}_{\rm e-ph}\,|\downarrow\rangle_{\rm p}\right]^2 D_{\rm ph}(E_{\rm Z,p}), \quad (2.41)$$

where $\mathcal{H}_{\rm e-ph}$ is the electron-phonon coupling Hamiltonian, $D_{\rm ph}$ is the phonon density of states, and $E_{\rm Z,p}$ is the pseudo-spin Zeeman energy. This process only causes energy relaxation without the effect to phase information [83]. From Eq.2.41, T_1 depends on the phonon density of states at the energy splitting of the pseudo-spin due to conservation of energy. The effect of piezoelectric phonons dominates over that of deformation potential phonons and optical phonons due to small energy scales. T_1 has a strong field dependence of $T_1 \propto B^{-5}$ in the low temperature limit [82]. The T_1 value ranging from 120 μs at 14 T to 170 ms at 1.75 T is observed for one-electron GaAs QDs with the expected B^{-5} dependence [12, 59, 82, 84]. In leading order in $\mathcal{H}_{\rm SO}$, there is no phase randomization, such that in fact $T_2 = 2T_1$ [83].

2.6.2 Hyperfine Interaction in Quantum Dots

An electron spin confined in QD interacts with nuclear spins in the host material through the hyperfine coupling unless the nuclei are spinless. In case of GaAs QDs, all nuclei ^{69}Ga, ^{71}Ga and ^{75}As have spin 3/2 and the hyperfine coupling is known as the central spin problem [85, 86]. Since the electron wave function is non-zero at the nucleus, the Hamiltonian of hyperfine interactions is described by the Fermi contact hyperfine interaction,

$$\mathcal{H}_{\mathrm{HF}} = \sum_{k}^{N} A_k \boldsymbol{I}_k \cdot \boldsymbol{S}, \tag{2.42}$$

where $\boldsymbol{I}_k$ and $\boldsymbol{S}$ are the spin operators for the k-th nuclear spin and the electron spin, respectively, and A_k is the coupling strength between these two. The dynamics of nuclear-nuclear flip-flop, mediated by the hyperfine interaction, is usually a complex many-body problem and hard to solve. In GaAs QDs, an electron spin confined in QD interacts with 10^5 to 10^6 nuclear spins and, in a semi-classical description, the effect of the nuclear spins can be treat as an effective magnetic field,

$$\mathcal{H}_{\mathrm{HF}} = \left(\sum_{k}^{N} A_k \boldsymbol{I}_k \right) \cdot \boldsymbol{S} = g\mu_{\mathrm{B}} \boldsymbol{B}_{\mathrm{N}} \cdot \boldsymbol{S}, \tag{2.43}$$

where $\boldsymbol{B}_{\mathrm{N}}$ is the *Overhauser field*, the effective nuclear field seen by electron spins due to nuclear spins. When the nuclear spins are fully polarized, the maximum value of the Overhauser field $|\boldsymbol{B}_{\mathrm{N}}|_{\max} \sim 5\mathrm{T}$ [87]. Under typical experimental conditions without complicated nuclear spin pumping pulses, the nuclear spins are in the thermodynamic equilibrium since their Zeeman energies are mush smaller than the thermal energy even at cryogenic temperature. From the central-limit theorem, the statistical fluctuation of the Overhauser field follows the Gaussian distribution with a standard deviation $\sqrt{\langle |\boldsymbol{B}_{\mathrm{N}}|^2 \rangle} \sim |\boldsymbol{B}_{\mathrm{N}}|_{\max}/\sqrt{N}$ where N is the number of the nuclear spins interacting with the electron spin. In GaAs QDs, $N \simeq 10^6$ and the nuclear field deviation is a few mT [12, 62] with a correlation time scale of ∼10-100 s [88].

The effective magnetic field which the electron spin feels is a sum of the external $\boldsymbol{B}_0$ ($\parallel \hat{z}$) and Overhauser field : $\boldsymbol{B}_{\mathrm{eff}} = \boldsymbol{B}_0 + \boldsymbol{B}_{\mathrm{N}}$. For $|\boldsymbol{B}_0| \ll |\boldsymbol{B}_{\mathrm{N}}|$, the contribution of the transverse components of $\boldsymbol{B}_{\mathrm{N}}$ ($\parallel \hat{x}, \hat{y}$) becomes negligible. The longitudinal component $B_{\mathrm{N},z}$ causes a change of the Larmor frequency by $|g|\mu_{\mathrm{B}} B_{\mathrm{N},z}/h$ and results in dephasing when a time-ensemble average is taken over the fluctuating $B_{\mathrm{N},z}$. Under typical experimental conditions, the fluctuating $B_{\mathrm{N},z}$ follows Gaussian distribution, and then the spin phase coherence decay is also Gaussian with a characteristic time [89]

$$T_2^* = \frac{\hbar\sqrt{2}}{|g|\mu_{\mathrm{B}} \sqrt{\langle (B_{\mathrm{N},z})^2 \rangle}}. \tag{2.44}$$

When $\sqrt{\langle (B_{\mathrm{N},z})^2 \rangle} = 1$ mT and $g \approx -0.4$, T_2^* becomes 40 ns [25]. This short T_2^*, however, does not reflect the intrinsic coherence of the system, i.e. $T_2 \gg T_2^*$. The lower bound on T_2 is characterized by echo measurements which removes the low frequency nuclear spin fluctuation, such as Hahn echo [25, 74] and Car-Purcell-Meiboom-Gill (CPMG) decoupling [74, 90]. The phase coherence time as long as $T_2^{\mathrm{CPMG}} \sim 800\mu$s has been demonstrated [91] and this is considered to be the lower bound of T_2.

Preparation of less fluctuating nuclear environment is another approach to enhance spin coherence and increase the quantum gate accuracy. The dynamic nuclear spin polarization (DNP) is used to prepae less fluctuating nuclear environment and improve the coherence time by a factor of ~ 10 [92]. Recently, the adaptive qubit control after nuclear field estimation is demonstrated using a technique of fast measurement and then the coherence time enhanced by a factor of ~ 100 [93].

2.7 Application as the Fermi-Hubbard Model

Here, we describe the other application of the semiconductor QD system toward the quantum simulation experiments. Due to the potential for realizing novel electronic and magnetic properties of correlated electron phases in low dimentional condensed matter physics such as high-T_{C} superconductivity and electronic spin liquids [43–45], the quantum simulations have been investigated in multiple platforms [36–42]. There are two methods to achieve quantum simulations; digital or analougue simulation. In the digital quantum simulation, theoretical and experimental work has shown [41, 42] but it comes at the cost of requiring huge number of qubits with additional error correction overhead. The analogue quantum simulations aim to implement well-defined Hamiltonian directly. Since the semiconductor QD system is a scalable platform that can be described by a Fermi-Hubbard model and the control and detection method of the charge and spin states are highly established, it can be said the promised platform of the analogue quantum simulation.

Experimental work in TQD are reported in [7]. In this paper, realize a detailed characterization of the finite-size analogue of the interaction-driven Mott metal-to-insulator transition [43]. The benefit of the analogue quantum simulation gets bigger in larger MQD system but, as discussed in §2.1.3, the control and detection of the charge and spin state of MQD gets more difficult. Especially in QQD, the spin state measurement with PSB needs the voltage control in the multiple voltage

plane [15].

Chapter 3

Control and Detection of the Charge States of Quintuple Quantum Dot

A semiconductor quintuple quantum dot (5QD) with two charge sensors and an additional contact for the center dot to an electron reservoir is fabricated to demonstrate the concept of scalable architecture. This design enables the formation of five dots whose charge states are gate-tunable. The gate-tunability is confirmed from measurements of the charge states in the three dots with the nearest charge sensor. The gate performance of the measured stability diagram is well reproduced by a capacitance model. These results provide an important step towards realizing controllable large scale multiple quantum dot systems. In this chapter, we first describe the difficulties in scaling up the MQD system and then the solutions and fabrication of the 5QD device with a concept relevant for further scale-up and measurement of the charge state.

3.1 Difficulties in Further Scaling Up the Multiple Quantum Dot

MQD devices usually consist of QDs tunnel-coupled in a row and a single charge sensor. In this geometry, an oscillating electric field can be uniformly applied to the whole QD array. This is done to prevent unnecessary photon-assisted tunneling caused by a non-uniform electric field. The utility of such a device geometry has been proved by the realization of TQD and QQD devices; however, at the same time, it has been understood that there are some difficulties in further scaling up MQD.

3.1.1 Insufficient Sensitivity of Charge Sensor

One of the difficulties is the limited sensitivity of the charge sensor. As discussed in §2.1.2, the combination of QPC or SET and rf-reflectometry is utilized to detect the charge states in the MQD. The sensitivity of the charge sensor depends on the capacitive coupling of the sensor to the respective QDs, and therefore, it decreases as the QD becomes distant. It also depends on the property of the semiconductor wafer such as electron density or mobility; however, generally speaking, the sensitivity of the charge sensor to the MQD array is only good for the nearest three QDs. Therefore, in the further scaled-up system such as 5QDs, a single charge sensor cannot distinguish between all charge states.

3.1.2 Complicated Charge States Distribution

The second difficulty is the complicated charge state distribution. As discussed in §2.1.3, the charge states of n-QDs are spread in the n-dimensional space defined by n plunger gate voltages. The two-dimensional (2D) stability diagram is one slice of the n-dimensional charge states distribution, and therefore, mapping out the whole charge state distribution in 2D is impossible. In TQD, we could map out the full charge state distribution in the three-dimensional stability diagram as shown in Fig.2.13; however, this cannot be done for more multiple QDs. In addition, cross-capacitive couplings between QDs and gate electrodes disable the independent controls of MQD parameters such as chemical potentials and tunnel barriers.

3.1.3 Difficulties in the Electron Exchanges

MQDs are usually constructed by connecting dots in a row with a tunnel-coupled reservoir at each end. This geometry makes it difficult to load electrons from the reservoirs to the inner dots [94]. As discussed in §2.3.1 and §2.3.2, electron exchange with a reservoir is utilized for the readout and initialization of the spin states confined to the QDs. In single and double QD devices, all QDs connect with the reservoir. On the other hand, in TQD and QQD devices, QDs at each end only connect with reservoirs, but the initialization of the two electron spin states can be performed by loading electrons from the reservoirs. However, in the 5QD device, the center QD is well isolated from the reservoirs. One of the possible solutions is to use a single spin CCD method; however, it can induce undesired spin flips due to spin-orbit interaction.

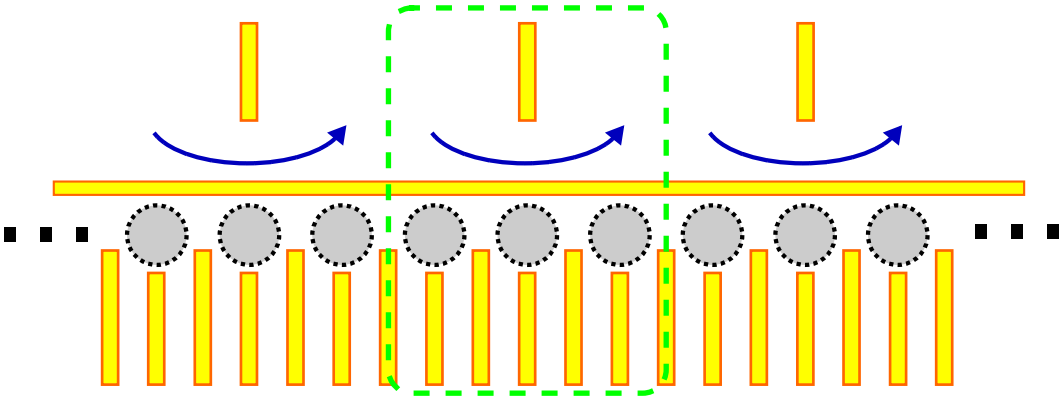

Figure 3.1: Schematic of the new device architecture. Yellow rectangles, dotted circles, and blue arrows indicate gate electrodes, QDs, and QPCs, respectively. The dashed green rectangle indicates a unit structure configured of three QDs and one charge sensor.

3.2 New Device Architecture for Further Scaling-Up

Here, we describe a device architecture to solve the above difficulties shown schematically in Fig.3.1. This architecture is designed for application to not only 5QDs but also further scaled-up MQDs. In order to complement limited sensitivity of the charge sensor, multiple charge sensors are formed so that there is one charge sensor for the 3 QDs (shown as blue arrows in Fig.3.1). In rf-reflectometry, as discussed in §2.1.2, the charge sensor configures the tank circuit with the inductance L and parasitic capacitance $C_{\rm p}$, and the charge transition of neighboring QDs are detected as changes of the reflected signal at the resonance frequency $f_{\rm RES}$ of the tank circuit. Therefore, by changing L in each tank circuit, the charge sensor signals in the rf-reflectometry can be detected by the reflected signal in different $f_{\rm RES}$. Utilizing this architecture, we can consider a unit cell of MQD structure configured of 3 or 4 QDs and a charge sensor (shown as dashed green rectangle in Fig.3.1). We will utilize this unit cell structure even in the charge state control. As discussed in §2.1.3 and [15], for the control of the charge states of QQD, multiple voltage planes are used. With a single voltage plane defined by two plunger gate voltages in end QDs, we could not observe the required charge state for PSB but it was not observable for two voltage planes of $V_{\rm P_1} - V_{\rm P_2}$ and $V_{\rm P_3} - V_{\rm P_4}$. This multi-voltage plane control is, in other words, the control of each

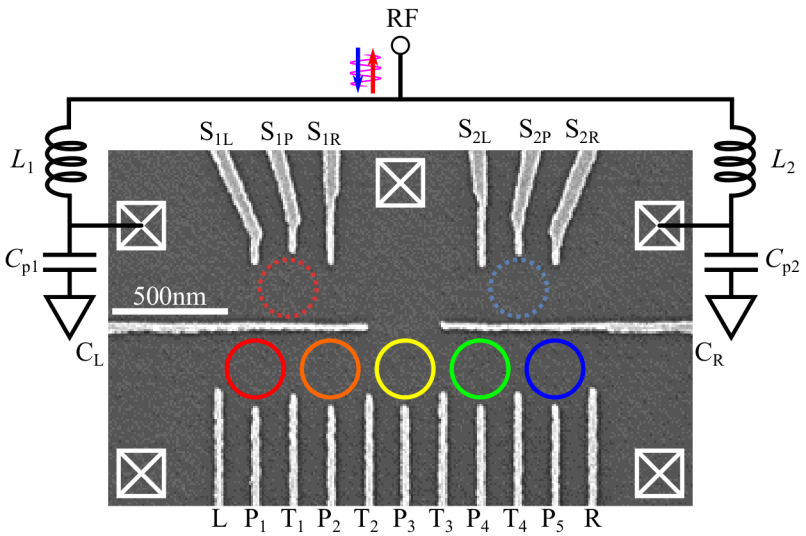

Figure 3.2: SEM image of the 5QD device and schematic of the measurement setup. White rectangles with crossmarks indicate Ohmic contacts.

unit cell for the left and right DQDs. In each voltage plane, due to the difference of capacitive couplings, the charge state of the left (or right) DQD are modulated and the other DQD is not affected so much. In the same way, the concept of different voltage plane control will work in a further scaled-up system.

3.3 Measurement of Quintuple Quantum Dot

In this section, we describe the measured result in the 5QD device in the new architecture.

3.3.1 Device Structure

Fig3.2 shows an SEM image of the 5QD device. The gate electrodes are shown in white. The 2DEG is formed 60 nm under the wafer surface. We patterned a mesa by wet-etching and formed Ti/Au Schottky surface gates by metal deposition. All measurements were conducted in a dilution fridge cryostat at a temperature of 27 mK. By applying negative voltages to the gate electrodes, seven QDs in total will

be formed at the positions indicated by five solid circles and two dotted circles. The five QDs under the horizontal gate electrodes C_L and C_R are the qubit QDs named QD_1, QD_2, QD_3, QD_4 and QD_5 in red, orange, yellow, green and blue, respectively. The plunger gate P_i tunes predominantly the energy level of QD_i , while the tunnel gate T_j tunes the tunnel coupling between QD_j and QD_{j+1}. In the conventional device architecture, the 5QD array connects with two reservoirs via both end QDs (QD_1 and QD_5) of the array. In the new architecture, a gap between C_L and C_R induces an additional coupling of QD_3 to the upper reservoir. Electrons are then loaded from the three reservoirs to all dots.

The two QDs above C_L and C_R are the sensor QDs named S_1 and S_2 in red and blue, respectively. The sensor QDs are connected to the respective RF resonators configured by the inductances $L_1 = 270$ nH and $L_2 = 470$ nH, and the parasitic capacitances $C_{p1} \simeq C_{p2} \simeq 0.4$ pF. They configure resonance circuits with different resonant frequencies f_{RES1} and f_{RES2}. These charge sensors are designed to detect the leftmost (QD_1, QD_2 and QD_3) and rightmost (QD_3, QD_4 and QD_5) TQDs, respectively.

3.3.2 Measurement Circuit

Fig.3.3 shows a schematic of the measurement circuit that refers the circuit utilized in [58]. This circuit includes two sets of the demodulation circuit for rf-reflectometry considering the simultaneous readout of the two charge sensors. The basic theory of rf-reflectometry is already described in §2.1.2; and therefore, we only describe the difference here. First, two local oscillators produce rf-carriers in different frequencies f_1 and f_2. The rf-carriers are separated in two directions by the directional coupler. One side is used to demodulate the reflected signal in each frequency at the mixers. The other side of the separated carriers are sent to the device via the combiner and attenuators. The reflected carriers are divided from incident carriers by a directional coupler in the low temperature part of the refrigerator. The reflected signal is amplified by a two step amplifier and split to two mixers.

Fig.3.4 (a) shows the frequency dependence of the reflected rf signal $|S_{21}|$ with different values of sensor conductance measured in the setup, as shown in Fig.3.2 and Fig.3.3 but not using the demodulation circuits. Three resonance dips caused by the resonance circuits including S_1 and S_2 are observed. The red and blue traces show $|S_{21}|$ in the different conductances of S_1 and S_2, respectively. The dip observed at 207 MHz (240 MHz) is largely affected by the conductance change of S_1 (S_2), and not by that of S_2 (S_1). This result indicates that the resonance dips

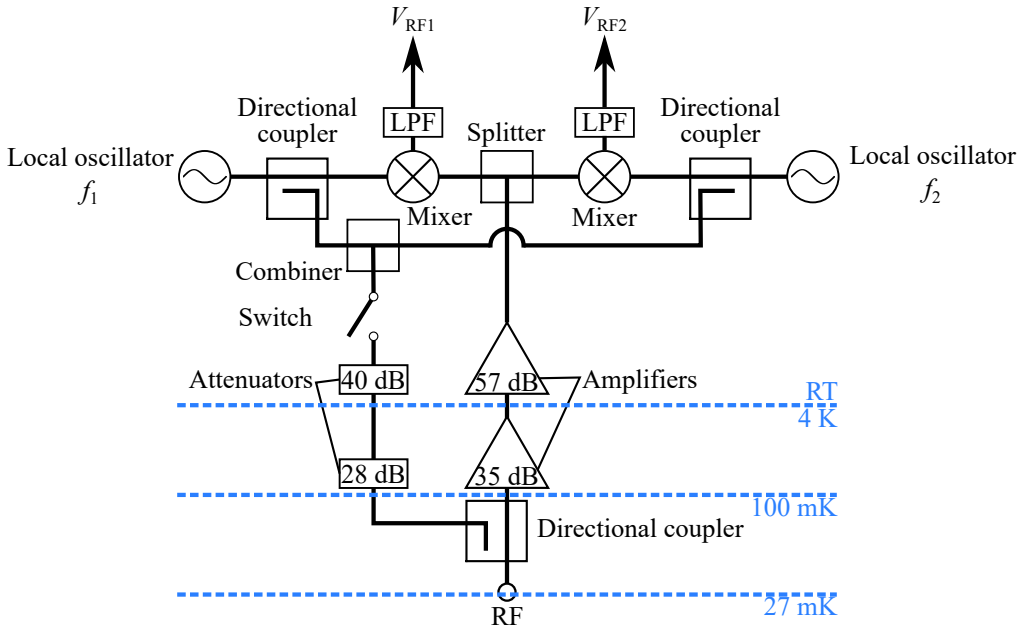

Figure 3.3: Schematic of measurement setup used in the experiment. Bottom white circle is connected to the white circle in Fig.3.2. Blue dashed lines indicate the boundary of the environment temperature.

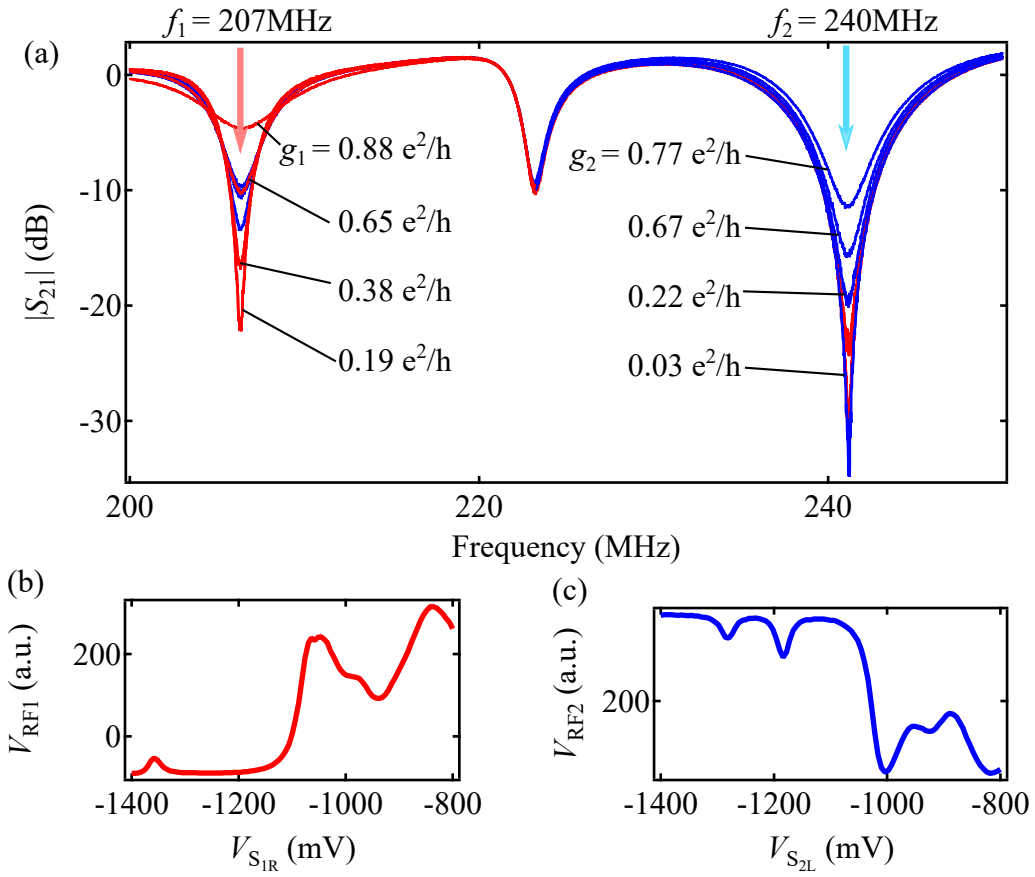

Figure 3.4: Rf-reflectometry (a) Frequency dependence of the reflected signal for different values of sensor conductance. (b)-(c) Gate voltage dependence of the V_{RF1} and V_{RF2}. In each figure, voltage applied on the gate electrode that form the sensor QD is modulated ($V_{\mathrm{S_{1R}}}$ in (b) and $V_{\mathrm{S_{2L}}}$ in (c)).

observed at 207 MHz and 240 MHz are caused by the left and right charge sensors, respectively. The center dip is not sensitive to either of the charge sensors and it is probably caused by the resonance circuit that is not connected to the device.

Fig.3.4 (b) and (c) shows the gate voltage dependences of the demodulated rf signals V_{RF1} and V_{RF2}. By modulating the gate voltage forming the sensor QD, the change in the charge sensor conductance, g_i, is detected as $V_{\mathrm{RF}i}$ ($i = 1, 2$). Note that due to a difference in phase, the V_{RF2} change appears in the opposite direction to the V_{RF1} change in Fig.3.4 (c). In the following measurement, the gate voltages for each charge sensor are adjusted to the condition most sensitive to the electrostatic changes of the surrounding environment.

3.3.3 Tuning of the Quintuple Quantum Dot

Here, we describe the tuning method in MQD. First, we estimate the voltage conditions for each single QD by the dot current measurement. Then, we readjusts these voltage conditions to form DQD, TQD, QQD and 5QD with the rf-reflectometry measurement.

Forming Single and Double Quantum Dots

In the initial tuning of the single QD, the dot current measurement is still a useful method to estimate the appropriate voltage conditions. First, we measure the gate voltage dependence of the QPC conductance in each pair of the gate electrodes such as L and $\mathrm{C_L}$ or R and $\mathrm{C_R}$. To form a single dot, the voltage on the tunnel gate electrode is tuned to the near pinch-off point of QPC and that on the plunger gate electrode is tuned to the value where the 2DEG beneath the electrode is depleted. We derive all these voltage values from the QPC traces. DQD can be formed by combining the values of gate voltages for two respective QDs. Figs.3.5 (a) - (c) show the measured dot current as a function of the voltage on the three tunnel gates L,$\mathrm{T_1}$, and $\mathrm{T_2}$, and Coulomb oscillations are observed. Fig.3.5 (d) shows the deviation of V_{RF1} to $V_{\mathrm{P_1}}$ as a function of $V_{\mathrm{P_1}}$, and $V_{\mathrm{P_2}}$ with the tunnel gate voltages when tha second or third most negative Coulomb peaks are observed in Figs.3.5 (a)-(c). The charge transition lines with two different slopes are observed in this figure, indicating that the DQD comprises of $\mathrm{QD_1}$ and $\mathrm{QD_2}$. The voltage conditions to form the DQD configured of $\mathrm{QD_4}$ and $\mathrm{QD_5}$ are estimated similarly.

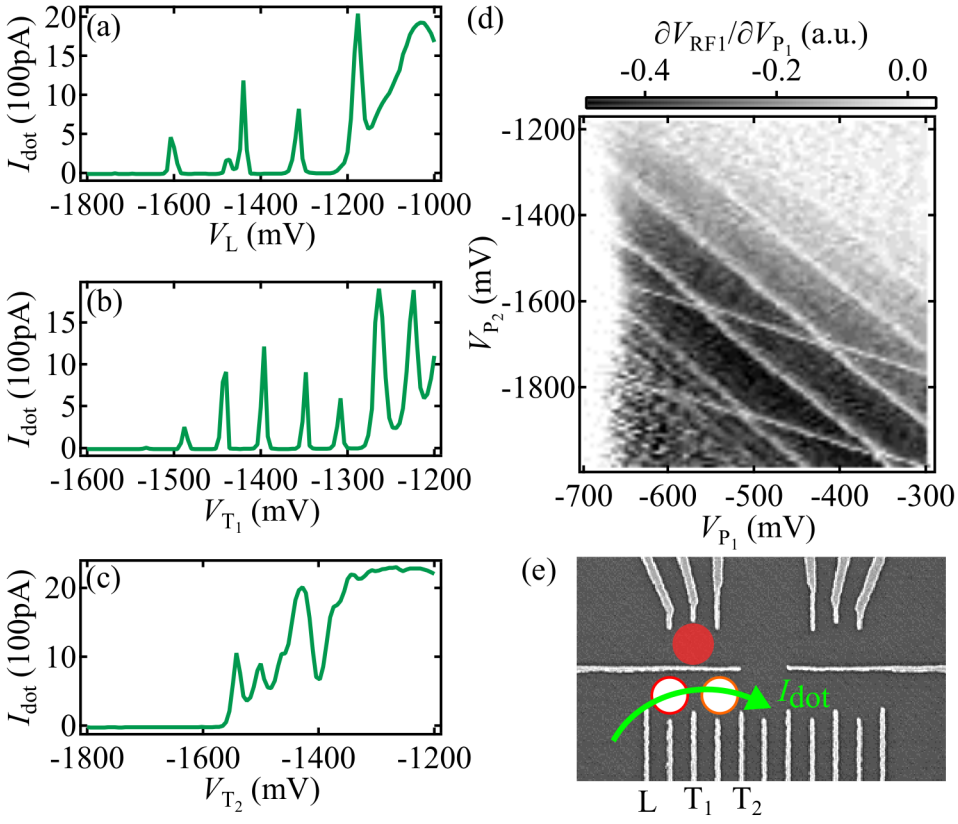

Figure 3.5: Initial tuning of DQD. (a) -(c) I_{dot} through DQD as a function of tunnel gate voltages V_{L}, $V_{\mathrm{T_1}}$, and $V_{\mathrm{T_2}}$, respectively. (d) Stability diagram of DQD configured of $\mathrm{QD_1}$ and $\mathrm{QD_2}$ in the $V_{\mathrm{P_1}} - V_{\mathrm{P_2}}$ plane. In this measurement, V_{REF1} is measured without bias voltage through DQD. (e) Schematic of the relative position of DQD, charge sensor and measured I_{dot}.

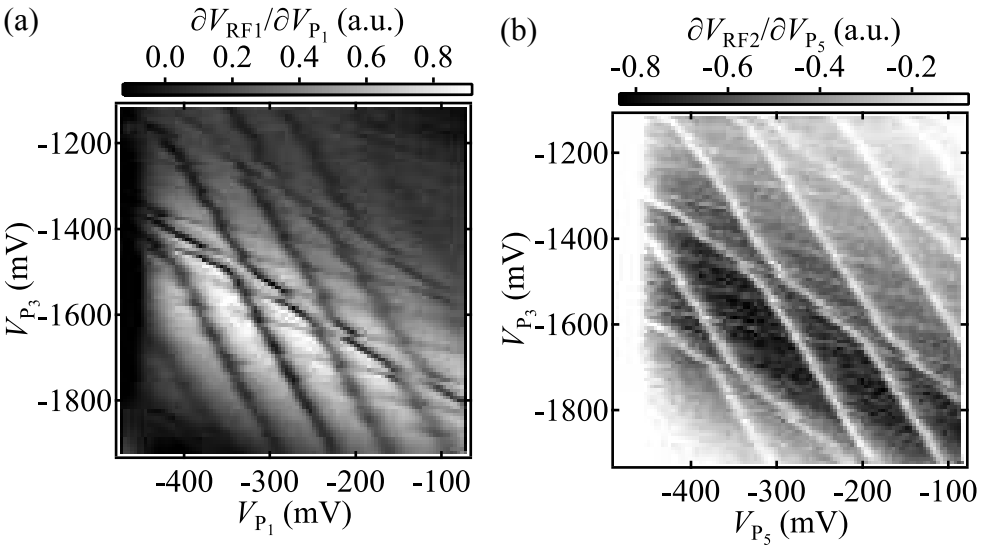

Figure 3.6: Stability diagrams of 5QD in multiple voltage planes. (a) Stability diagram in the V_{P_1}-V_{P_3} plane measured by S_1. (b) Stability diagram in the V_{P_5}-V_{P_3} plane measured by S_2. At the center of both diagrams, all gate voltage conditions are same ($V_{\mathrm{L}} = -1500$ mV, $V_{\mathrm{P}_1} = 286$ mV,$V_{\mathrm{T}_1} = -1180$ mV, $V_{\mathrm{P}_2} = -1140$ mV, $V_{\mathrm{T}_2} = -1100$ mV, $V_{\mathrm{P}_3} = -1120$ mV,$V_{\mathrm{T}_3} = -1010$ mV, $V_{\mathrm{P}_4} = -1260$ mV, $V_{\mathrm{T}_4} = -1510$ mV, $V_{\mathrm{P}_5} = -298$ mV and $V_{\mathrm{R}} = -1200$ mV.)

Tuning of the Quintuple Quantum Dot in Multiple Voltage Planes

Gate tuning of the 5QD can be simplified by splitting 5QDs into two TQDs and manipulating the charge states on the two different stability diagrams. Figs.3.6 (a) and (b) show the stability diagrams measured in the different voltage planes of V_{P_1}-V_{P_3} in (a) and V_{P_5}-V_{P_3} in (b). In each diagram, we observe three sets of distinct charge transition lines with three different slopes, reflecting the capacitive couplings between the TQD and modulating gate electrodes. In each diagram, the most and second most horizontal charge transition lines can be assigned to the charge transition lines for QD_1 and QD_2 in (a) and QD_5 and QD_4 in (b). In these voltage planes, the charge transition lines for the other QDs (QD_3, QD_4, and QD_5 in (a), QD_1, QD_2 and QD_3 in (b)) have almost the same slopes, and therefore, it is hard to distinguish. We adjust the voltages on V_{T_1}, V_{T_2}, V_{T_3}, and V_{T_4} to make all tunnel or electrostatic couplings between the adjacent dots roughly the same judging from the size of avoided crossings between two different charge transition lines. Here we confirm that there are no apparent couplings present between non-neighboring dots, because the corresponding charging lines just cross each other. Since the two diagrams share a common V_{P_3} axis in the same range, we are able to evaluate the appropriate voltages of all gates to manipulate the charge state of the 5QD.

3.3.4 Simultaneous Readout of Charge State of the Quintuple Quantum Dot

We use the gate voltage setting derived from Fig.3.6 as a guide to establish the stability diagram of the 5QD. Figs.3.7 (a) and (b) show the diagram in the V_{P_1}-V_{P_5} voltage plane measured by S_1, and S_2, respectively. In both figures, five sets of charge transition lines with different slopes can be distinguished, and from the slopes, we can assign them to charging five different dots: QD_1 to QD_5 from vertical to horizontal. The difference in the spacing of the charge transition lines of QD_1 and QD_5 is caused by the difference in the lever arm of the gates or the charging energy. These diagrams are measured simultaneously using the multiplex technique of RF reflectometry. Note the charge transition lines of QD_1 to QD_3 are clearly visible whereas those of QD_4 and QD_5 are less visible in (a). In contrast the charging lines of QD_3 to QD_5 are more visible in (b). This observation indicates that each sensor is sensitive to charging of at least three nearest QDs, and two sensors can together detect all charge transitions of the 5QD; note that the QDs in Fig.3.7 (a) and (b) are not in a few electron regime due to the lim-

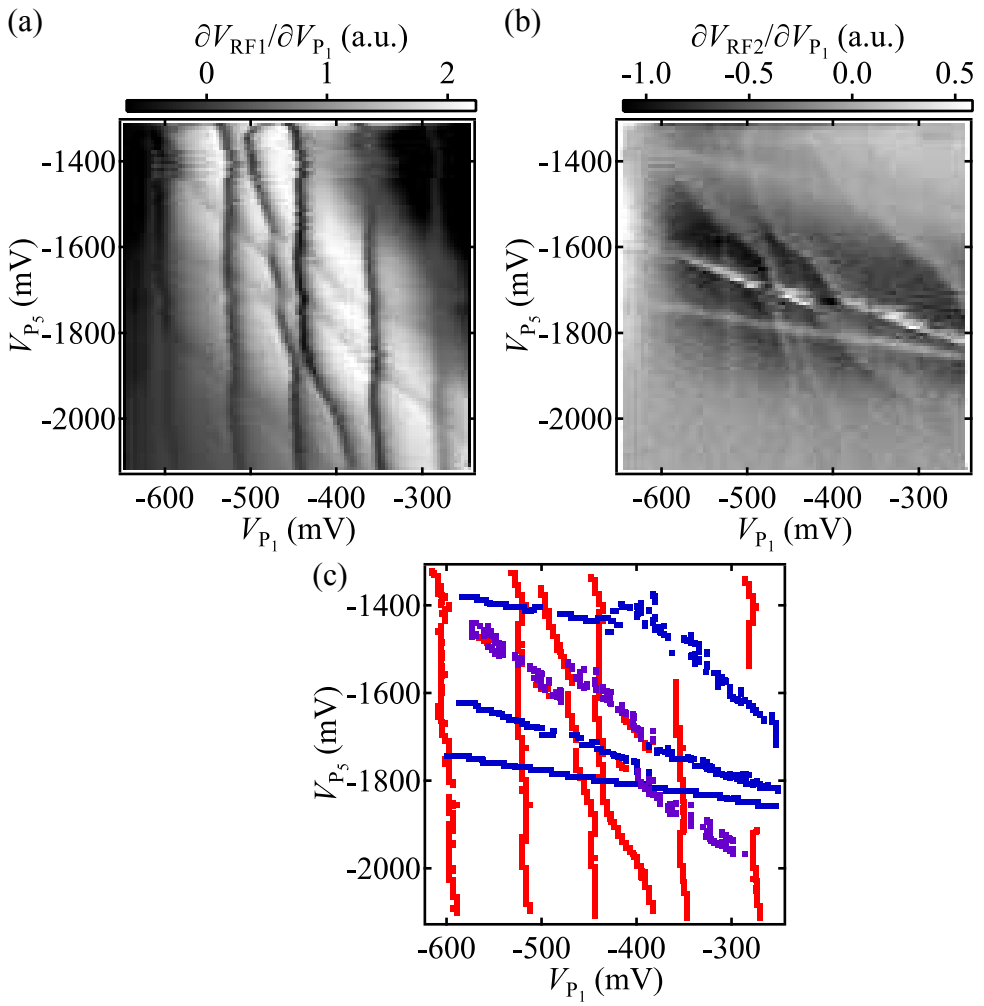

Figure 3.7: Stability diagrams of 5QD in the V_{P_1}-V_{P_5} plane. (a) and (b) Diagrams measured by S_1 and S_2, respectively. They are measured simultaneously with $V_{\mathrm{P}_2} = -1585$ mV, $V_{\mathrm{P}_3} = -1020$ mV, and $V_{\mathrm{P}_4} = -470$ mV. (c) Data points extracted from the charge transition lines in (a) and (b): Red or blue points from (a) or (b), respectively.

itation of the gate voltage range, and it contain dozens of electrons, judging from the spacing of the charge transition lines [16]. Further, QD_3 has the most electrons because of the gate electrode design. We will be able to reduce the number of electrons by reducing the gaps between the gates to form smaller dots.

In Fig.3.7 (c), we show the charging lines for the 5QD by plotting the data points of the dark and white lines in Figs.3.7 (a) and (b): red and blue points from (a) and (b) and purple points from both. Avoided crossings of charging lines of neighboring QDs indicate finite capacitive couplings among all five QDs, as is the case in Fig.3.6. Further, none of the charge transition lines are fragmented, suggesting that the tunneling rates are kept sufficiently high for all QDs.

3.3.5 Capacitive Coupling Model

In large MQD systems, the charge states become complicated and difficult to discriminate. Therefore, numerical calculations of stability diagrams are helpful in the process of adjusting gate voltages to search for the desirable charge states. We find that the stability diagram obtained here is well reproduced in a qualitative manner using a capacitive QD model [15,95]. Fig.3.8 (a) shows a schematic of the capacitive coupling model for 5QD. This model is an extension of the capacitive DQD [95] and QQD [15] model to five QDs. In this model, we consider that QD_i is capacitively coupled to the other QD_j ($i \neq j$) via a *mutual capacitance* $C_{\mathrm{m}ij}$, and to the plunger gate P_j via *cross-talk capacitance* C_{ij} ($i, j = 1, 2, 3, 4, 5$). QD_1, QD_3 and QD_5 are also coupled to the three electron reservoirs via $C_{\mathrm{L}}, C_{\mathrm{C}}$ and C_{R}, respectively, but their effect can be ignored since $V_{\mathrm{L}} = V_{\mathrm{C}} = V_{\mathrm{R}} = 0$ in the measurements. There are 45 parameters in total to adjust in this model but we can assume $C_{\mathrm{m}ij} = C_{\mathrm{m}ji}$ since it is defined only by the relative position of QD_i and QD_j. Here, we estimate the parameters for the capacitive model from some stability diagrams. $C_{\mathrm{m}ij}$ can be estimated from the size of the anti-crossing of charge transition lines of QD_i and QD_j, and C_{ii} can be estimated from the spacing of the charge transition lines of QD_i. The ratio of C_{ij} to C_{jj} can be estimated from the slope of the charge transition line of QD_j in the $V_{\mathrm{P_i}}$-$V_{\mathrm{P_j}}$ plane.

From the measured results, the values of mutual capacitances are estimated as $C_{\mathrm{m12}} = 0.1$, $C_{\mathrm{m13}} = 0.05$, $C_{\mathrm{m23}} = 0.18$, $C_{\mathrm{m24}} = 0.05$, $C_{\mathrm{m34}} = 0.18$ and $C_{\mathrm{m45}} = 0.05$, as the ratio to the charging energy of each QD. The cross-capacitance can be written as a 5×5 matrix and estimated as

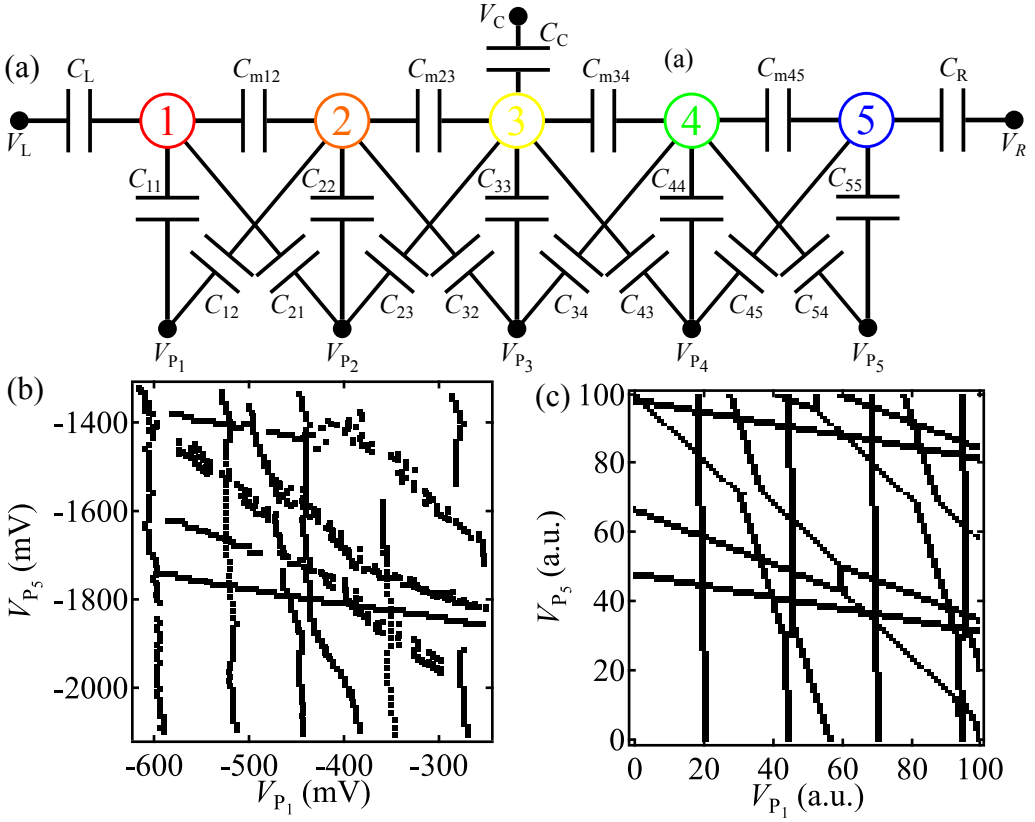

Figure 3.8: (a) Schematic of 5QD capacitive coupling model used to calculate the charge stability diagram. (b) Measured charge stability diagram of 5QD in (V_{P_1}-V_{P_5}) voltage plane (same data with Fig.3.7(c)). (c) Calculated stability diagram of 5QD in (V_{P_1}-V_{P_5}) voltage plane.

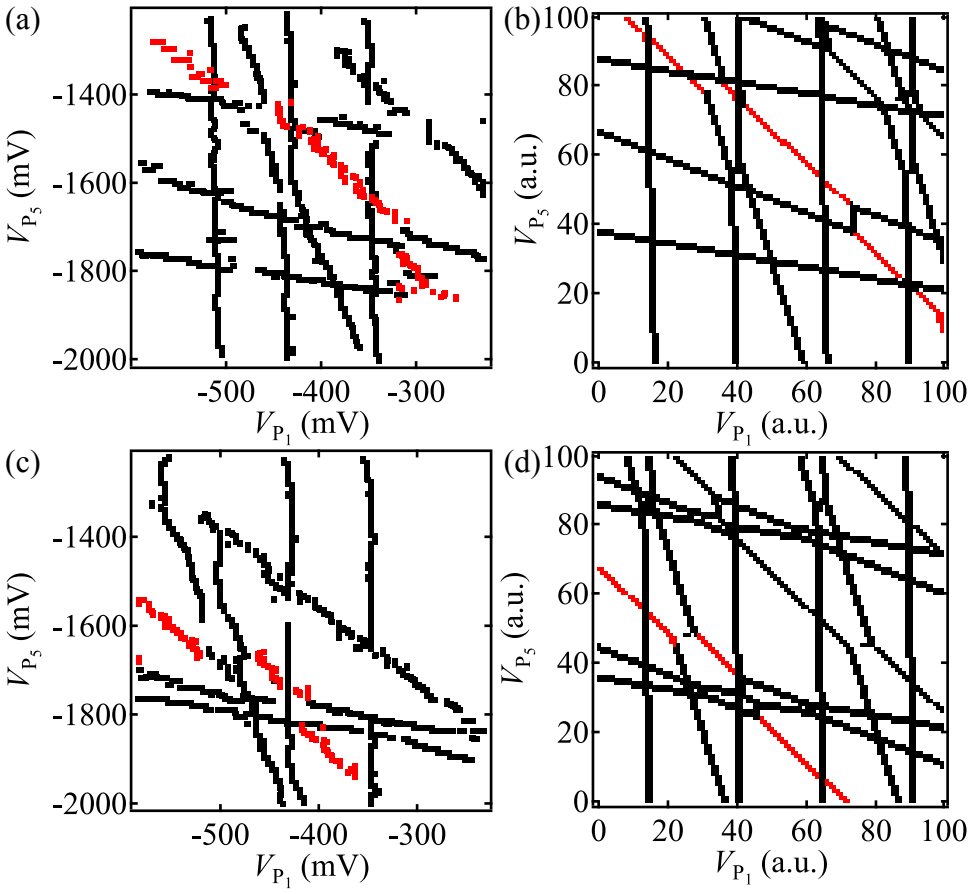

Figure 3.9: Measured and calculated stability diagrams of 5QD in (V_{P_1}-V_{P_5}) voltage plane. In each diagram, V_{P_3} or the parameter equivalent to V_{P_3} is shifted from the conditions in Fig.3.8 (b) and (c). (a) Measured diagram with negative shift in V_{P_3} about 20mV. (b) Calculated diagram with negative shift in the parameter equivalent to V_{P_3}. (c) Measured diagram with positive shift in V_{P_3} about 20mV. (d) Calculated diagram with positive shift in the parameter equivalent to V_{P_3}. In all diagram, one of the charge transition lines for QD_3 is colored red.

$$C_{\mathrm{cross}} = \begin{pmatrix} 1.0 & 0.5 & 0.05 & 0.05 & 0.0 \\ 0.5 & 1.0 & 0.75 & 0.4 & 0.1 \\ 0.25 & 0.85 & 1.0 & 0.85 & 0.3 \\ 0.1 & 0.4 & 0.80 & 1.0 & 0.5 \\ 0.0 & 0.05 & 0.05 & 0.5 & 1.0 \end{pmatrix}. \tag{3.1}$$

With this C_{cross}, the shifts of the chemical potential for QD_i, $\delta\mu_i$, can be written as

$$\begin{pmatrix} \delta\mu_1 \\ \delta\mu_2 \\ \delta\mu_3 \\ \delta\mu_4 \\ \delta\mu_5 \end{pmatrix} = C_{\mathrm{cross}} \cdot \begin{pmatrix} \Delta V_{\mathrm{P}_1} \\ \Delta V_{\mathrm{P}_2} \\ \Delta V_{\mathrm{P}_3} \\ \Delta V_{\mathrm{P}_4} \\ \Delta V_{\mathrm{P}_5} \end{pmatrix} \tag{3.2}$$

where ΔV_i is the gate voltage change of plunger gate P_i. Fig.3.8 (c) shows the calculated stability diagram with C_{cross} in Eq.3.1. This simple model shows good agreement with the experiment in which the QDs contain many electrons and when we focus on a limited range of the charge stability diagram. We see that the main features in Fig.3.8 (b) are well reproduced by the calculation. Figs.3.9 (a) and (b) show the stability diagrams measured in different values of V_{P_3} from the voltage conditions in Fig.3.8 (b) ($V_{\mathrm{P}_3} = -1040$ mV in (a) and $V_{\mathrm{P}_3} = -1000$ mV in (b)). In these figures, the charge transition line in red shifts largely but the other lines also shift due to the finite capacitive couplings. Even under these conditions, the capacitive coupling model can reproduce the stability diagrams only by slightly changing V_{P_3} in Fig.3.9 (b) and (d). This model also reproduces the shifts of the transition lines in the other plunger gate voltages. The capacitive model is a powerful tool to distinguish the charge configuration in the complicated charge state distribution.

3.3.6 Conditions for Pauli Spin Blockade in Quintuple Quantum Dots

With the capacitive coupling model, we consider the realization of spin readout using PSB. In PSB, it is necessary that two neighboring QDs have adjacent two charge states of (2,0) (or (0,2)) and (1,1). In the case of TQD, the PSB measurement for the (1,1,1) charge state can be performed on the left DQD: (2,0,1)

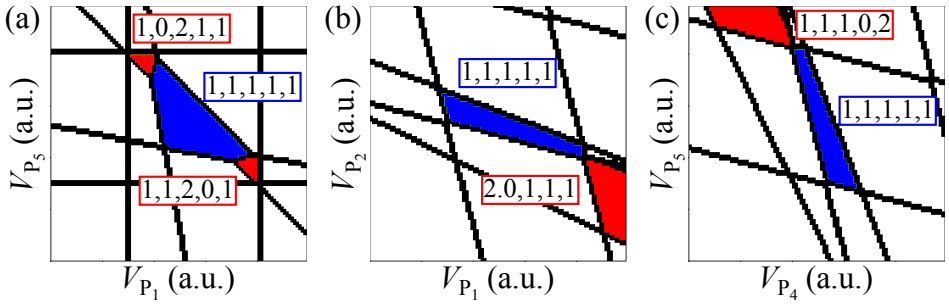

Figure 3.10: Numerically simulated stability diagrams by capacitive coupling model. (a) The stability diagram in the V_{P_1}-V_{P_5} plane around the (1,1,1,1,1) charge state shown as the blue region. (1,0,2,1,1) and (1,1,2,0,1) charge states shown as red regions are adjacent to (1,1,1,1,1) and the PSB measurements in QD_2, QD_3, and QD_4 are available in this voltage plane. (b) The stability diagram in the V_{P_1}-V_{P_2} plane around the (1,1,1,1,1) charge state. The (2,0,1,1,1) charge state is adjacent to the (1,1,1,1,1) charge state, and the PSB measurement in QD_1 and QD_2 is available in this voltage plane. (c) The stability diagram in the V_{P_4}-V_{P_5} plane around the (1,1,1,1,1) charge state. The (1,1,1,0,2) charge state is adjacent to the (1,1,1,1,1) charge state and the PSB measurement in QD_4 and QD_5 is available in this voltage plane.

$\leftrightarrow$(1,1,1) , and right DQD: (1,0,2) $\leftrightarrow$ (1,1,1). These three charge states become adjacent in the V_{P_1}-V_{P_3} voltage plane [17, 96]. In the case of QQD, however, the necessary charge states of the PSB measurement for the (1,1,1,1) charge state cannot be allocated in one voltage plane and we need voltage control in multiple voltage planes [15]. Similar to Ref. [15], we consider the voltage planes and voltage condition to realize PSB measurements in each QD of 5QD with the (1,1,1,1,1) charge state. Figs.3.10 (a)-(c) show the numerical simulation of the stability diagram with the capacitive coupling model, and the voltage conditions of V_{P_1} to V_{P_5} are assumed to be the same at the center of each diagram. In these figure, the basic charge state (1,1,1,1,1) used for qubit operation is colored blue and the charge states for PSB readout are colored red. Fig.3.10 (a) is the stability diagram in the V_{P_1}-V_{P_5} voltage plane, and the (1,0,2,0,1) and (1,1,2,0,1) charge states become adjacent. In this condition, the PSB measurements for the center three QDs (QD_2, QD_3, and QD_4) can be performed. Fig.3.10 (b) shows the stability diagram in the V_{P_1}-V_{P_2} plane and the PSB measurement can be performed for QD_1 and QD_2 with the transition of (1,1,1,1,1) $\leftrightarrow$ (2,0,1,1,1). Fig.3.10 (c) shows the stability diagram in the V_{P_4}-V_{P_5} plane and the PSB measurement can be performed for QD_4 and QD_5 with the transition of (1,1,1,1,1) $\leftrightarrow$ (1,1,1,0,2). From these numerical simulation results, we predict that the PSB measurements can be performed for all five QDs in three different voltage planes.

3.4 Summary

In conclusion, we fabricated a 5QD device based on the scalable architecture of MQDs, which consists of a TQD unit cell with two reservoirs and a charge sensor. Though the 5QD device have three reservoirs and two charge sensors, we characterized the gate performance on the charge state stability diagram and well distinguished the charge transition lines corresponding to all five QDs owing to the use of the two charge sensors. We also studied the spin and charge state control in the 5QD with the numerical simulation by the capacitive coupling model, and we found that at most three different voltage planes are necessary for the PSB measurements in all QDs These results are important steps to further scale up the MQD system and to employ this system as a spin qubit system.

Chapter 4

Four single-spin ESR and Rabi oscillations in a quadruple quantum dot

Scaling up qubits is a necessary step to realize useful systems of quantum computation. In this chapter, we demonstrate coherent manipulations of four individual electron spins using a MM-ESR method in each dot of a QQD - the largest number of dots used for the single spin control in MQDs. We observe c.w. ESR and Rabi oscillations for each dot though ESR and evaluate the spin-electric coupling of the four QDs, and finally discuss practical approaches to independently address single spins in MQD systems containing even more QDs.

In this chapter, we demonstrate single spin manipulation in each dot of the QQD device with the MM-ESR method. We use a correlated double sampling (CDS) technique [93] to enhance the ESR signal and observe a coherent oscillation (Rabi oscillation) of an electron spin in each dot by sweeping the ESR driving time. The acquired data allow us to estimate the QD positions and discuss how to improve the quality of the Rabi oscillations by considering the control speed and the addressability of the electron spin in each dot.

4.1 Device and Setup

Fig.4.1 shows a SEM image of the QQD device and a schematic picture of the measurement electric circuit. The device is fabricated in a modulation doped GaAs/AlGaAs heterostructure wafer containing a 2DEG whose depth from the

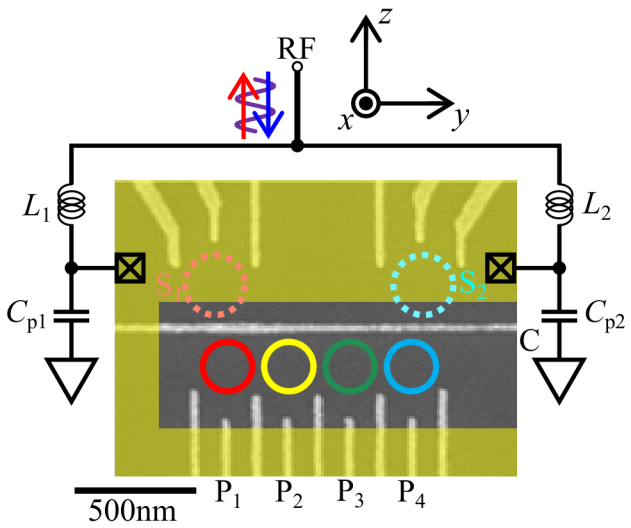

Figure 4.1: SEM image of the QQD device with a schematic representation of the measurement electric circuit. Here, z and y axes are parallel to the $[011]$ and $[0\bar{1}1]$ crystal axes, respectively.

surface is 100 nm. The Ti/Au gate electrodes placed on the surface appear in white. The MM (shown as a yellow shaded region) is placed on top of the gate electrode layer with a 100 nm thick insulator in between. By applying negative voltages on the gate electrodes, we form six dots in total as pictorially indicated by four solid and two dotted circles. The four dots under the horizontal gate electrode named C are the qubit dots named QD_1 , QD_2 , QD_3 and QD_4 in red, yellow, green and blue, respectively and tunnel-coupled next to each other. The two dots above gate C are the sensor dots named S_1, and S_2 in red, and blue, respectively. The sensor dots are connected to the respective RF resonators configured by inductances L_1 and L_2 and stray capacitances C_{p1} and C_{p2} with resonance frequency of $f_{RES1} = 298$ MHz for S_1 and $f_{RES2} = 207$ MHz for S_2. We monitor the charge state of the QQD via the reflected RF signals [97, 98], V_{RF1} and V_{RF2} of the two sensors at the respective resonance frequencies. The MM-ESR is performed by applying a microwave (MW) to gate C in the presence of an external magnetic field B_{ext} along the z-axis as shown in Fig.4.1. The MM is magnetized in the B_{ext} direction and creates a stray field across the QQD. The shape of the MM is specially designed for the MM-ESR to address the four dots [17, 35, 71] such that the stray field produces a slanting field B_{Sl}(x-component of the stray field slanted

along z) for driving the electron spin rotation and a local magnetic field B_{Z} along z axis that changes the resonance condition among the four dots. All measurements described below are conducted in a dilution fridge at a base temperature of $T = 13$ mK.

4.2 Spin State Initialization and Readout

4.2.1 Spin State Initialization Using a Detuning Pulse

Fig.4.2 (a) shows the stability diagram measured by monitoring V_{RF1} in the V_{P_1}-V_{P_4} plane. We identify the dot-lead and inter-dot charge transition lines indicated by the dotted lines, and assign them in red, yellow, green and blue from horizontal to vertical to the dot-lead charge transition lines of QD_1 , QD_2 , QD_3 and QD_4 , respectively. We denote the charge state as (n_1, n_2, n_3, n_4), where n_i with $i = 1, 2, 3, 4$ is denoting the number of electrons confined in QD_i. At the lower left corner of this diagram, all dots are completely depleted ((0,0,0,0) charge state). The inter-dot transition lines are depicted as purple dotted lines.

In the MM-ESR experiment, we use PSB in DQDs for the spin readout [25]. Then the spin configuration, up or down is distinguished by measuring the transition between (2,0) (or (0,2)) and (1,1). As discussed in the§2.1.3, the necessary charge states of the PSB measurement for (1,1,1,1) charge state cannot be allocated in one voltage plane and need voltage control in multiple voltage plane [15]. Because Our target is the demonstration and evaluation of the MM-ESR method in the QQD device, in the following measurements, we separate the QQD into two DQDs of QD_1-QD_2 and QD_3-QD_4, and mainly focus on the charge states of (2,0,0,1) and (1,1,0,1), and (1,0,1,1) and (1,0,0,2) to operate the MM-ESR in QD_1 and QD_2 with S_1, and QD_3 and QD_4 with S_2 , respectively. In Fig.4.2(a), all of these charge states are observed and positioned tight next to (1,1,1,1) charge state. We note that the tunnel coupling between QD_2 and QD_3 is not precisely tuned or measured but we can change it over a wide range. Fig.4.2 (b) (or (c)) shows the enlarged stability diagram around the boundary line between (2,0,0,1) (or (1,0,0,2)) and (1,1,0,1) (or (1,0,1,1)). By utilizing these charge configurations, we can use the similar operation protocol established in the DQD system [34] for both DQDs without large voltage condition changes.

Fig.4.3 (a) shows a schematic of the gate voltage pulses for the ESR measurements. Here three voltage conditions named I, M and O are specified in Figs.4.2 (b) and (c) by the green circles to define the four operation sections, “Initializa-

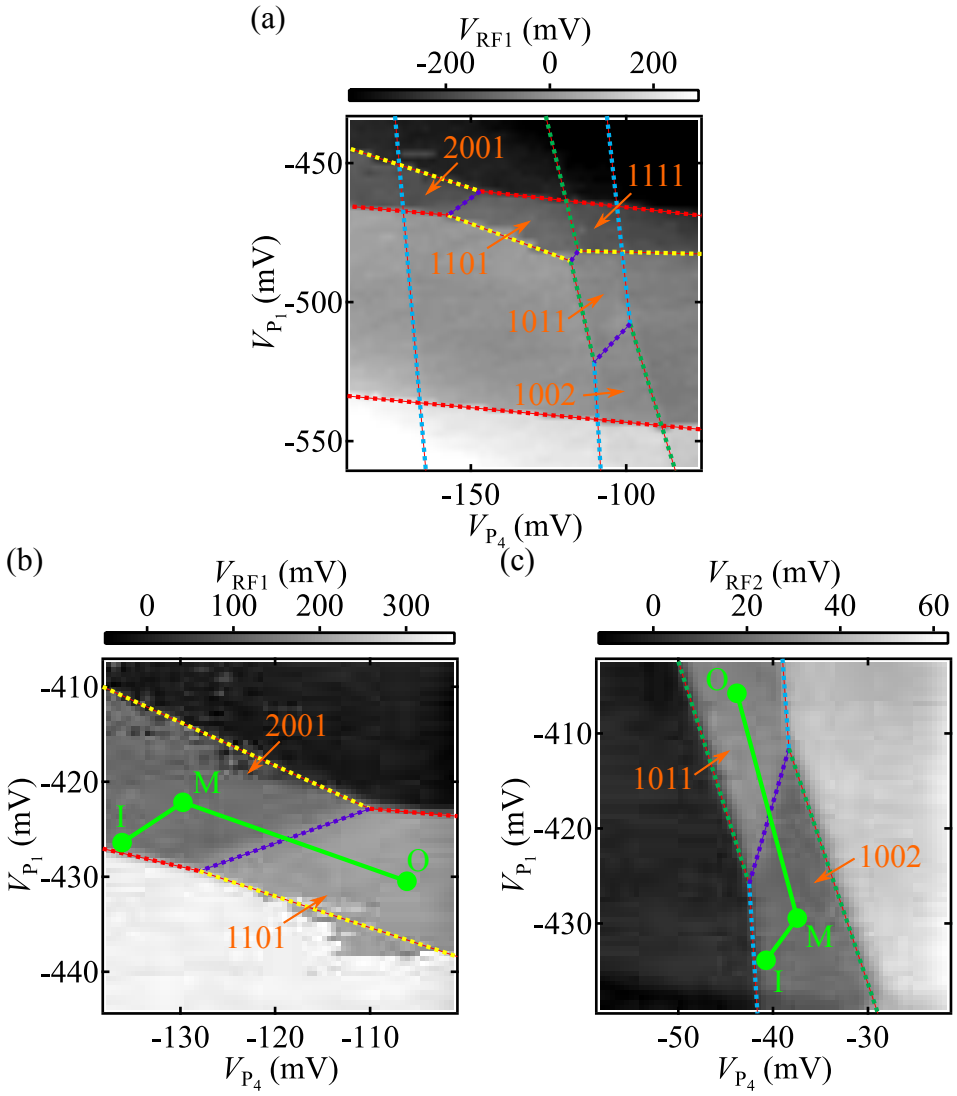

Figure 4.2: Stability diagrams of QQD measured in the device shown in Fig.4.1. (a) Stability diagram in (V_{P_1}-V_{P_4}) voltage plane measuring V_{RF1} with a background plane subtracted. (b) Enlarged stability diagram relevant for experiments in QD_1 and QD_2. Green circles and bars show the voltage conditions and pulse shape that are utilized in ESR measurements in left DQD. (d) Enlarged stability diagram relevant for experiments in QD_3 and QD_4. Here the voltage conditions and pulse shape for the ESR measurements in right DQD are shown similarly.

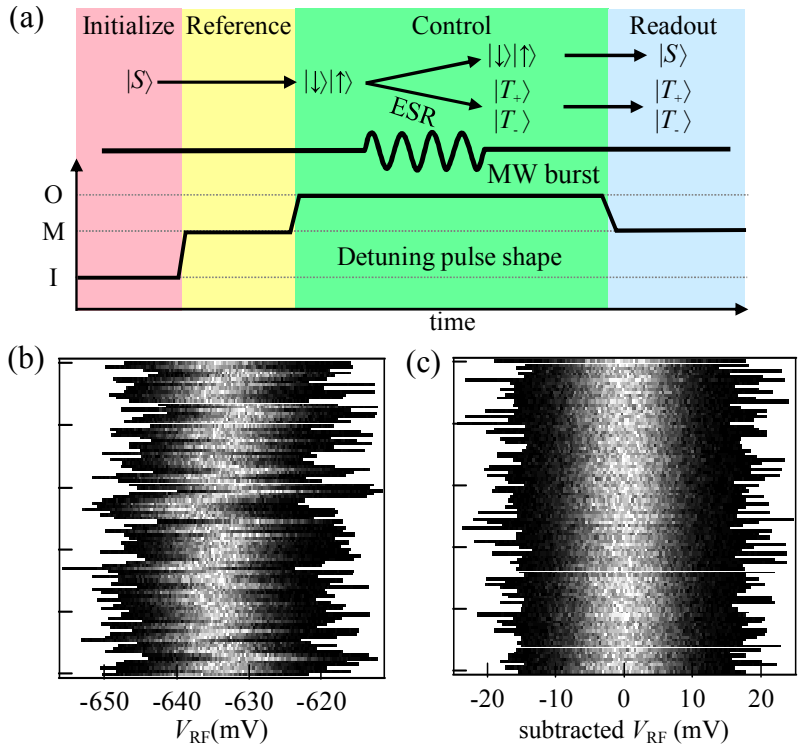

Figure 4.3: (a) The pulse sequence for the ESR measurement. The horizontal axis shows time and the vertical axis pictorially denotes the voltage conditions at points O, M and I in Figs.4.2 (b) and (c). (b) Measured charge sensor signal histograms. Each histogram consists of 512 readout results, each representing the V_{RF} value averaged over 33μs, and is generated in about 100ms. This V_{RF} histogram measurement is repeated 100 times in total. The horizontal axis indicates charge sensor signal and the vertical axis is the number of trials. (c) Measured charge sensor signal histograms with the CDS techniques. The horizontal axis indicates subtracted charge sensor signal.

tion" in red, "Reference" in yellow, "Control" in green and "Readout" in blue. Note that throughout the four operation sections, the third electron spin is decoupled from the controlled spins with an empty QD in between. In the "Initialization" section, the voltage condition is tuned to point I that is close to the charge transition line of the outer dots (QD_1 and QD_4). The two-electron spin state in QD_1-QD_2 (or QD_3-QD_4) is initialized to the ground doubly occupied singlet state $|S\rangle$ in QD_1 (or QD_4) by exchanging electrons with the adjacent reservoir. In the "Reference" section the voltage condition is tuned to point M that is deep inside the Coulomb blockade region of the doubly occupied charge state (2,0,0,1) (or (1,0,0,2), discuss later). This stage does not influence the spin state and we obtain the background signal of the charge sensor in this section. In the "Control" section the voltage condition is changed to point O where two electrons in QD_1 (or QD_4) are separated into QD_1 and QD_2 (or QD_3 and QD_4) to form (1,1,0,1) (or (1,0,1,1)) having the anti-parallel spin state $|\downarrow\rangle|\uparrow\rangle$ [25, 35]. Then, a MW burst is applied on gate C to spatially oscillate electron spins in all dots in the MM induced B_{Sl}. The electron spin coherently flips between $|\uparrow\rangle$ and $|\downarrow\rangle$ but independently in each QD when the resonance condition of $f_{\mathrm{MW}} = |g|\mu_{\mathrm{B}}(B_{\mathrm{ext}} + B_{\mathrm{Z}})/h$ is satisfied. Here f_{MW} is the MW frequency, g is the Lande g-factor of the electron confined in the QD, and μ_{B} is the Bohr magneton, respectively. Finally, in the "Readout" section with the voltage condition back to point M, the spin state is detected using PSB. When the spin is not flipped in either of QD_1 or QD_2 (or QD_3 or QD_4), the two-electron spin state returns to the doubly occupied $|S\rangle$ in QD_1 (or QD_4). When the spin is flipped in either dot, the two-electron state is either $|T_+\rangle$ or $|T_-\rangle$, the charge state remains singly occupied in QD_1-QD_2 (or QD_3-QD_4) without relaxing to the doubly occupied $|S\rangle$. Here, we measure the singlet return probability P_{S} or the probability of finding the two electron spin state in the $|S\rangle$ by taking the difference of V_{RF1} (or V_{RF2}) from that measured in the " Reference" section (CDS method).

With this readout method, the charge-state distinction fidelity affects the spin readout fidelity. However, the signals of both charge sensors show the low frequency drifts which leads to the low distinction fidelity. Fig.4.3 (b) shows a series of one hundred V_{RF} histograms taken continuously at the "Readout" section of the pulse without a MW burst. The horizontal axis indicates V_{RF} value and the vertical one indicates the sequence number of histograms that are continuously measured. The time evolution of the histogram reveals the drift of V_{RF} whose standard deviation is 2.34mV that may be due to charge noise or fluctuation of the gate voltages. The difference in V_{RF} between singly and doubly occupied charge states are roughly 50mV and 10mV in S_1 and S_2, respectively. The difference be-

tween the charge sensor sensitivities may be caused by the difference of the actual position of dot sensor. This V_{RF} drift can cause the wrong charge state assignment and lower the visibility of the ESR signal.

Here, we utilize a CDS method to stabilize the low frequency V_{RF} drift. To perform CDS, we extend the "Reference" section of the pulse sequence and V_{RF} is measured for the same acquisition time as in "Readout" section. In this method, V_{RF} signal measured in "Reference" section is used as the background signal level to be subtracted from that in the "Readout" section. Fig.4.3 (c) shows a series of compensated V_{RF} histogram. We can see that the drift in V_{RF} is greatly suppressed and the standard deviation of this drift is reduced to 0.20mV. With this stable charge sensor, we can utilize fixed threshold value for the distinction of the charge states. Without CDS method, the threshold value for the distinction is estimated from the V_{RF} histogram in each time but this method is unstable in this case. However, with the fixed threshold value that is estimated from V_{RF} histogram before ESR measurement, such instability in the readout can be removed and the readout fidelity can be improved.

4.3 Realization of c.w. ESR of Four Individual Spins

Figs.4.4 (a) and (b) show the P_{S} as a function of f_{MW} and B_{ext} upon application of the MW pulse with pulse sequence shown in Fig.4.3 (a). Figs.4.3 (a) and (b) are measured for the left and right DQD using S_1 and S_2 , respectively. We observe two distinct lines due to ESR in QD_1 and QD_2 in (a) and QD_3 and QD_4 in (b). The separation of the two ESR lines in each figure is due to the Zeeman energy difference, which arises from the differences in the MM-induced B_{Z} and g-factor among dots. This separation is much larger than the ESR line width of ~ 10 MHz and therefore enables us to access each resonance condition independently by choosing the f_{MW} and B_{ext} properly. The line width is likely dominated by the nuclear spin fluctuation, consistent with the Rabi frequencies f_{Rabi} values (discussed later) smaller than the typical standard deviation of the nuclear field (about 7MHz in GaAs QDs).

For the comparison, Figs.4.4 (c) and (d) show the similar results measured in the same device but without CDS method. Even in these figure, four individual ESR lines are observed but the S/N ratios and the strength of the ESR lines are quite smaller than that in Figs.4.4 (a) and (b). It indicates that the CDS method and stabilization of charge sensor improve the strength of ESR.

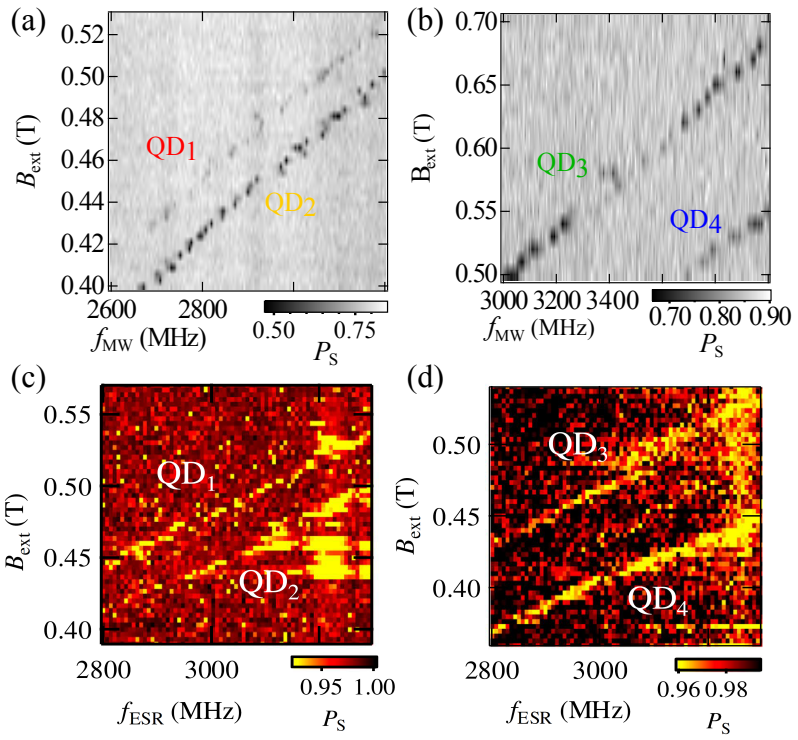

Figure 4.4: Measured P_S as a function of B_{ext} and f_{MW} with CDS method ((a) and (b)) and without CDS method ((c) and(d)) [35] . (a) and (c) show the ESR signal of the left side DQD (QD_1 and QD_2). (b) and (d) show the ESR signal of the right side DQD (QD_3 and QD_4). The two yellow or black lines in each figure indicate the ESR lines for two different QDs.

4.4 Coherent Control of Four Individual Spins

4.4.1 Observation of Four Individual Rabi Oscillations

Next, we perform measurements of single-electron spin oscillations by applying same pulse sequence but changing the MW burst time $t_{\rm MW}$ in the "Control" section. Figs.4.5 (a), (b), (c), and (d) show the $P_{\rm S}$ measured at the respective resonance condition of QD_1, QD_2, QD_3 and QD_4. We observe Rabi oscillations of the electron spin in each dot. The Rabi oscillations are best resolved in QD_2 with frequency 5.32 MHz, the highest among all dots. On the other hand, the Rabi oscillation is less clear for the other QDs because of the lower frequency of about 2 MHz. In these figures, the curve fittings are shown fitted by a power law envelope function with a $\pi/4$ phase shift [99] $P_{\rm S} = \frac{A}{\sqrt{t_{\rm MW}}}\cos(2\pi f_{\rm Rabi} t_{\rm MW} + \pi/4) + B_{\rm off} - C t_{\rm MW}$. The last linear term accounts for the reduction of $P_{\rm S}$ due to the leakage to non-qubit states presumably caused by photon-assisted tunneling [100]. Unfortunately, the fidelities of initialization, single electron spin control, and readout would be too low to estimate the control fidelity using the existing methods such as randomized benchmarking [101]. As for the quality of Rabi oscillation, possible improvements include optimizing the tunnel coupling between the QDs and reservoirs and applying higher $P_{\rm MW}$ in order to enlarge the effective a.c. magnetic field. We can estimate the contributions of spin orbit interaction [26] and nuclear spin polarization [102] to the observed $f_{\rm Rabi}$ values. Our device is fabricated so that spin orbit interaction accelerates the MM-ESR [17, 34] and its contribution is calculated to be tens of mT/μm. Similarly, the contribution of nuclear spin polarization is estimated to be about tens of mT/μm from the typical parameters for GaAs QDs. These values are two orders of magnitude smaller than the $B_{\rm Sl}$ created by MM ($\sim$1T/μm).

4.4.2 Analysis of the Rabi Oscillations

We measured Rabi oscillations for various MW output power $P_{\rm MW}$ values and derived $f_{\rm Rabi}$ from the curve fitting described above. The obtained values of $f_{\rm Rabi}$ are shown as a function of MW amplitude in Fig.4.4 (e). The MW amplitude is calculated from the applied $P_{\rm MW}$ and the RF line attenuation solely given by discrete attenuators (-39 dB). We observe $f_{\rm Rabi}$ linearly depending on the MW amplitude for each QD. We derive the slope of the linear fitting to the data points and find that it is different from dot to dot with ratio of $3:10:11:26$ for QD_1 to QD_4. The slope of the fitting line is related to the spin-electric coupling roughly

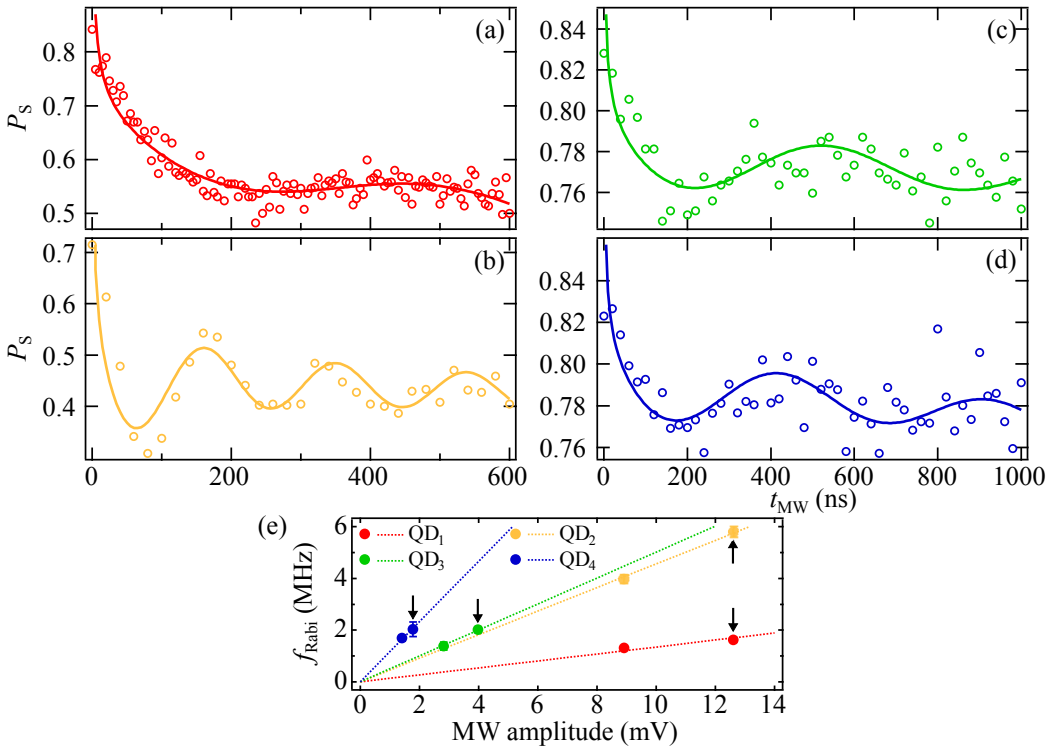

Figure 4.5: Rabi oscillations of the single electron spins measured for QD_1 with $f_{MW} = 2751$ MHz, $B_{ext} = 0.45$ T and $P_{MW} = 10$ dBm in (a), QD_2 with $f_{MW} = 2280$ MHz, $B_{ext} = 0.45$ T and $P_{MW} = 10$ dBm in (b), QD_3 with $f_{MW} = 3650$ MHz, $B_{ext} = 0.6$ T and $P_{MW} = 0$ dBm in (c), and QD_4 with $f_{MW} = 4400$ MHz, $B_{ext} = 0.6$ T and $P_{MW} = -6$ dBm in (d). The fitting parameters are $A = 0.73\sqrt{\text{ns}}$, $f_{Rabi} = 1.62$ MHz, $B_{off} = 0.65, C = 0.26\mu\text{s}^{-1}$ for QD_1, $A = 0.81\sqrt{\text{ns}}$, $f_{Rabi} = 5.32$ MHz, $B_{off} = 0.46, C = 0.051\mu\text{s}^{-1}$ for QD_2, $A = 0.38\sqrt{\text{ns}}$, $f_{Rabi} = 2.02$ MHz, $B_{off} = 0.69, C = 0.012\mu\text{s}^{-1}$ for QD_3, $A = 0.22\sqrt{\text{ns}}$, $f_{Rabi} = 2.03$ MHz, $B_{off} = 0.79$ and $C = 0.018\mu\text{s}^{-1}$ for QD_4. We checked the robustness of the fitting results against the initial values used and the errors in estimated f_{Rabi} values are about 0.05MHz. (e) MW amplitude dependence of f_{Rabi} derived for each dot from the curve fitting to the Rabi oscillation data. The dotted lines are the fitting to the data points constrained to cross the origin. Data points extracted from (a) to (d) are indicated by black arrows.

proportional to the product of B_{Sl} and $l_{\mathrm{orb}}^2/\Delta$ where l_{orb} is the orbital spread along z axis and Δ is the QD confinement energy. Considering the MM design used in this device, the B_{Sl} value should gradually increase from QD_1 to QD_4. The experimental data seemingly agree with this trend but the observed variation of the slope is quantitatively larger than expected. We discuss this discrepancy later using Fig.4.6.

We note that we could not apply a large P_{MW} to the right DQD (QD_3 and QD_4) while we could to the left DQD (QD_1 and QD_2), because the ESR signals of QD_3 and QD_4 become obscure in the high P_{MW} range. So the Rabi oscillations shown in Figs. 4.5 (c) and (d) are only measured at a small P_{MW}, and therefore the oscillation frequency is significantly lower than that for QD_2. This may not be related to the robustness of the ESR conditions because P_{S} decreases with increasing P_{MW} even in the off-resonance conditions. One of the possible reasons is that the tunnel barrier between QD_4 and the right reservoir is not well closed and the electron can tunnel out to the reservoir more easily as the P_{MW} becomes large.

4.5 Estimation of the Actual Quantum Dot Positions

4.5.1 Estimation of g-Factor and Local Magnetic Field

In what follows, we discuss the electron spin addressability in the QQD device. We estimate the g-factors and B_{Z} values of individual QDs from the resonance lines in Figs.4.4. More specifically, we extract the values of B_{ext} and f_{MW} at the resonance condition from the local minima of P_{S} and perform the linear fit to the formula $hf_{\mathrm{RES}} = g\mu_{\mathrm{B}}(B_{\mathrm{ext}} + B_{\mathrm{Z}})$ to obtain the values of g and B_{Z}. The obtained values are shown by the red circles in Figs. 4.6 (a) and (b). Those extracted from the data measured with the different gate voltage condition in our previous experiment [35] are also shown by the blue circles. With both variations of g and B_{Z} we are able to independently address the MM-ESR in each dot. Indeed, the B_{Z} difference alone will not be large enough to resolve resonances between QD_1 and QD_2 in the present experiment, because the ESR line separation will be only 20 MHz comparable to the ESR line width. The variation of g between QDs may be explained by the difference in the confinement potential [103]. On the other hand, that of B_{Z} is probably due to variation of the dot position and inhomogeneity of the MM induced stray field. In support of this, we find the observed B_{Z} in each dot different when changing the gate voltage conditions.

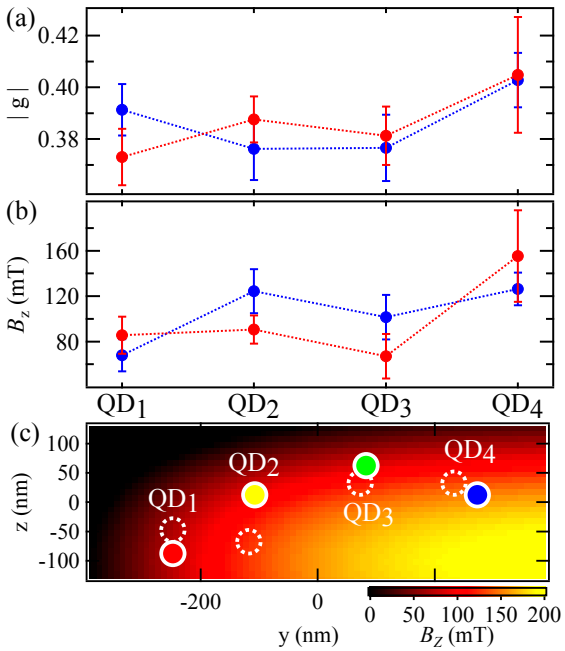

Figure 4.6: (a) g factors in each dot estimated from Figs.4.4 (a) and (b) (colored in red) and Figs.4.4 (c) and (d) (colored in blue). (b) B_Z in each dot estimated from the same data with (a) (colored in red and blue). The 90% confidence interval of estimated g and B_Z are shown as error bar. (c) Spatial distribution of the numerically calculated B_Z and the dot positions construed from the result in (b). The solid, and dotted circles indicate the positions for the data set in red, and blue in (b), respectively. Here we define the origin of the y and z axis as the center of the QD array.

This result implies that B_{Z} is varied from QD to QD in a controlled manner with the gate voltage condition and therefore allows us to independently address the MM-ESR in each dot. Fig.4.6 (c) shows a two-dimensional distribution (y-z plane in Fig.4.1) of the B_{Z} calculated numerically from the shape of the MM and the QD positions that explain the results of Fig.4.6 (b). The solid, and dotted circles indicate the positions for the data set in red, and blue in Fig.4.6 (b), respectively. The shifts of the QD positions from the center of gate structure are indeed rather large, exceeding the typical orbital spread of GaAs QDs $\sim$50nm. We speculate that these might have been caused by charged impurities or large variations among the voltages applied to the surface gates. Considering the application as quantum information processing hardware, such shifts from the center position may cause difficulties in coupling the qubits. However, Fig.4.6 (c) also indicates that their positions can be tuned by voltage conditions by a good fraction of 100 nm.

4.5.2 Estimation of Actual Quantum Dot Position

Finally, we discuss the variation of the MW amplitude dependence of f_{Rabi} among the four dots as observed in Fig.4.5 (e). The QD positions which can explain the B_{Z} values shown in Fig.4.6 (c) give the B_{Sl} ratio of $3:3:2:4$ for QD_1 to QD_4. These B_{Sl} values are numerically calculated in the same way with B_{Z}. This variation of B_{Sl} among dots is too small to fully account for that of the slopes of MW amplitude dependence. The variation of the g as shown in Fig.4.6 (a) can also influence the control speed but not so significantly. This discrepancy may be caused by inhomogeneity of the spin-electric coupling, which depends on the inhomogeneity of the confining potential profile and MM geometry or domain, although not well characterized.

4.6 Summary

In conclusion, we demonstrate coherent manipulations of four individual electron spins in each dot of a linearly coupled QQD with the MM-ESR method. The QQD is the largest multiple QD system ever used for coherent control of single electron spins. From measurements of Rabi oscillations and ESR signals, we quantified variations of the g-factor and the MM induced stray field at the dot positions. Our analysis hints at inhomogeneity in the spin-electric coupling, which may be due to the inhomogeneous dot potentials or MM stray field. The results obtained

here imply the gate-voltage-tunable addressability of four individual spins with the MM-ESR method, and therefore may pave the way towards the realization of four qubits system and the further scale-up of the spin qubit systems with QDs.

Chapter 5

Application of Quadruple Quantum Dot as a Quantum Simulation Platform

As discussed in §2.7, semiconductor MQDs can be a promising platform for the analogue quantum simulation of the Fermi-Hubbard model. Precise experiments were performed in the TQDs to study the interaction effect [7]; however, it focuses only on the charge degree of freedom. In this chapter, we investigate the method to scale up this analogue simulation to larger MQDs. First, we investigate the charge state distributions and the energy level diagrams of the QQD with the numerical simulations. Then, we measure and demonstrate the charge state distribution expected in the numerical calculations. Based on the demonstrations, we propose the measurement scheme for the analogue quantum simulation model.

However, this chapter could not be published in UT Repository because the results in this chapter are intended to published to journal later. In this version of my thesis, this chapter is deleted.

Chapter 6

Summary

This thesis focuses on scaling up the multiple QD system and its applications such as spin qubits and quantum simulations. The presented results are summarized as follows.

1. We fabricated the 5QD device with a new device architecture that considers further scaling up the MQD system. Utilizing this device, for the first time, we formed a tunnel-coupled five QD linear array. We also investigated its control and measurement method. (Chapter 3)

2. We demonstrated individual single spin control in each dot of the QQD with the MM-ESR method. We also estimated the actual dot positions from the ESR condition date and determined the possibility of further improvement of the single spin control in the QQD architecture. (Chapter 4)

3. We investigated the four electron spin states and proposed the scheme for the four electron spin state measurement in the QQD device. We demonstrated the charge state distribution when the necessary charge states are adjacent on one voltage plane. (Chapter 5, deleted in this version)

We believe that these results and improvements in scaling up the MQD system and applying the established techniques will contribute to research on quantum information processing with electron spin qubits and the application for analogue quantum simulations. In the near future, we will scale up the QD system quickly and focus on developing a multiple qubit system and we will demonstrate the quantum algorithms in this system.

Bibliography

[1] S. Tarucha, D. Austing, T. Honda, R. van der Hage and L. Kouwenhoven "Shell Filling and Spin Effects in a Few Electron Quantum Dot." *Physical Review Letters* **77**, 3613-3616 (1996).

[2] R. C. Ashoori "Electrons in artificial atoms." *Nature* **379**, 413-419 (1996).

[3] N. S. Kouwenhoven, L. P., Marcus C. M., McEuen P. L., Tarucha S., Westervelt R. M., and Wingreen "ELECTRON TRANSPORT IN QUANTUM DOTS." *the proceedings of the Advanced Study Institute on Mesoscopic Electron* **345**, 105-214 (1997).

[4] W. G. van der Wiel, S. De Franceschi, T. Fujisawa, J. M. Elzerman, S. Tarucha and L. P. Kouwenhoven "The Kondo Effect in the Unitary Limit." *Science* **323**, 2105-2108 (2000).

[5] K. Ono, D. G. Austing, Y. Tokura and S. Tarucha "Current rectification by Pauli exclusion in a weakly coupled double quantum dot system." *Science* **297**, 1313-1317 (2002).

[6] L. Gaudreau, S. A. Studenikin, A. S. Sachrajda, P. Zawadzki, A. Kam, J. Lapointe, M. Korkusinski and P. Hawrylak "Stability diagram of a few-electron triple dot." *Physical Review Letters* **97**, 036807 (2006).

[7] T. Hensgens, T. Fujita, L. Janssen, X. Li, C. J. Van Diepen, C. Reichl, W. Wegscheider, S. Das Sarma and L. M. K. Vandersypen "Quantum simulation of a Fermi - Hubbard model using a semiconductor quantum dot array." *Nature* **548**, 7665 (2017).

[8] I. Žutić, J. Fabian and S. Das Sarma "Spintronics: Fundamentals and applications." *Reviews of Modern Physics* **76**, 323-410 (2004).

[9] T. Byrnes, N. Y. Kim, K. Kusudo, and Y. Yamamoto, "Quantum simulation of Fermi-Hubbard models in semiconductor quantum-dot arrays." *Physical Review B* **78**, 075320 (2008).

[10] S. Yang, X. Wang, and S. Das Sarma, "Generic Hubbard model description of semiconductor quantum-dot spin qubits." *Physical Review B* **83**, 161301 (2011).

[11] C. A. Stafford and S. Das Sarma, "Collective Coulomb blockade in an array of quantum dots: A Mott-Hubbard approach." *Physical Review Letters* **72**, 3590 - 3593 (1994).

[12] R. Hanson, L. P. Kouwenhoven, J. R. Petta, S. Tarucha and L. M. K. Vandersypen "Spins in few-electron quantum dots." *Reviews of Modern Physics* **79**, 1217-1265 (2007).

[13] M. Ciorga, A. Sachrajda, P. Hawrylak, C. Gould, P. Zawadzki, S. Jullian, Y. Feng, and Z. Wasilewski, "Addition spectrum of a lateral dot from Coulomb and spin-blockade spectroscopy." *Physical Review B* **61**, R16315-R16318 (2000).

[14] R. H. Blick, R. J. Haug, J. Weis, D. Pfannkuche, K. V. Klitzing, and K. Eberl, "Single-electron tunneling through a double quantum dot: The artificial molecule." *Physical Review B* **53**, 7899 - 7902 (1996).

[15] M. R. Delbecq, T. Nakajima, T. Otsuka, S. Amaha, J. D. Watson, M. J. Manfra, and S. Tarucha, "Full control of quadruple quantum dot circuit charge states in the single electron regime." *Applied Physics Letters* **104**, 183111 (2014).

[16] T. Takakura, A. Noiri, T. Obata, T. Otsuka, J. Yoneda, K. Yoshida, and S. Tarucha, "Single to quadruple quantum dots with tunable tunnel couplings." *Applied Physics Letters* **104**, 113109 (2014).

[17] A. Noiri, J. Yoneda, T. Nakajima, T. Otsuka, M. R. Delbecq, K. Takeda, S. Amaha, G. Allison, A. Ludwig, A. D. Wieck, and S. Tarucha, "Coherent electron-spin-resonance manipulation of three individual spins in a triple quantum dot." *Applied Physics Letters* **108**, 153101 (2016).

[18] D. M. Zajac, T. M. Hazard, X. Mi, E. Nielsen, and J. R. Petta, "Scalable Gate Architecture for a One-Dimensional Array of Semiconductor Spin Qubits." *Physical Review Applied* **6**, 054013 (2016).

[19] A. Noiri, K. Kawasaki, T. Otsuka, T. Nakajima, J. Yoneda, S. Amaha, M. R. Delbecq, K. Takeda, G. Allison, A. Ludwig, A. D. Wieck, and S. Tarucha, "A triangular triple quantum dot with tunable tunnel couplings." *Semiconductor Science and Technology* **32**, 084004 (2017).

[20] U. Mukhopadhyay, J. P. Dehollain, C. Reichl, W. Wegscheider, and L. M. K. Vandersypen, "A 2 × 2 quantum dot array with controllable inter-dot tunnel couplings." *Applied Physics Letters* **112**, 183505 (2018).

[21] P.-A. Mortemousque, E. Chanrion, B. Jadot, H. Flentje, A. Ludwig, A. D. Wieck, M. Urdampilleta, C. Bauerle, and T. Meunier, "Coherent control of individual electron spins in a two dimensional array of quantum dots." *ArXiv* 1808.06180, (2018).

[22] D. P. DiVincenzo, "Quantum Computation." *Science* **270**, 255 - 261 (1995).

[23] D. Loss and D. P. DiVincenzo "Quantum computation with quantum dots." *Physical Review A* **57**, 120-126 (1998).

[24] J. M. Taylor, H. -a. Engel, W. Dür, a. Yacoby, C. M. Marcus, P. Zoller, and M. D. Lukin, "Fault-tolerant architecture for quantum computation using electrically controlled semiconductor spins." *Nature Physics* **1**, 177-183 (2005).

[25] J. R. Petta, A. C. Johnson, J. M. Taylor, E. A. Laird, A. Yacoby, M. D. Lukin, C. M. Marcus, M. P. Hanson, and A. C. Gossard "Coherent Manipulation of Coupled Electron Spins in Semiconductor Quantum Dots." *Science* **309**, 2180-2184 (2005).

[26] K. C. Nowack, F. H. L. Koppens, Y. V. Nazarov, and L. M. K. Vandersypen, "Coherent Control of a Single Electron Spin with Electric Fields - Supplementary." *Science* **318**, 5855 (2007).

[27] M. Pioro-Ladrière, T. Obata, Y. Tokura, Y.-S. Shin, T. Kubo, K. Yoshida, T. Taniyama, and S. Tarucha, "Electrically driven single-electron spin resonance in a slanting Zeeman field." *Nat. Phys.* **4**, 776-779 (2008).

[28] R. Brunner, Y.-S. Shin, T. Obata, M. Pioro-Ladrière, T. Kubo, K. Yoshida, T. Taniyama, Y. Tokura, and S. Tarucha, "Two-Qubit Gate of Combined Single-Spin Rotation and Interdot Spin Exchange in a Double Quantum Dot." *Physical Review Letters* **107**, 146801 (2011).

[29] F. Braakman, P. Barthelemy, C. Reichl, W. Wegschneider, and V. L.M.K., "Long-distance coherent coupling in a quantum dot array." *Nature Nanotechnology* **8**, 432 - 437 (2013).

[30] T. Fujita, T. A. Baart, C. Reichl, W. Wegscheider, and L. M. K. Vandersypen, "Coherent shuttle of electron-spin states." *Npj Quantum Information* **3**, 22 (2017).

[31] T. Nakajima, M. R. Delbecq, T. Otsuka, S. Amaha, J. Yoneda, A. Noiri, K. Takeda, G. Allison, A. Ludwig, A. D. Wieck, X. Hu, F. Nori, and S. Tarucha, "Coherent transfer of electron spin correlations assisted by dephasing noise." *Nature Communications* **9**, 2133 (2018).

[32] A. Noiri, T. Nakajima, J. Yoneda, M. R. Delbecq, P. Stano, T. Otsuka, K. Takeda, S. Amaha, G. Allison, K. Kawasaki, A. Ludwig, A. D. Wieck, D. Loss, and S. Tarucha, "A fast quantum interface between spin qubits of different codes." *Nature Communications* **9**, 5066 (2018).

[33] R. Laflamme, C. Miquel, J. P. Paz and W. H. Zurek "Perfect Quantum Error Correcting Code." *Physical Review Letters* **77**, 198-201 (1996).

[34] J. Yoneda, T. Otsuka, T. Nakajima, T. Takakura, T. Obata, M. Pioro-Ladrière, H. Lu, C. J. Palmstrøm, a. C. Gossard, and S. Tarucha, "Fast Electrical Control of Single Electron Spins in Quantum Dots with Vanishing Influence from Nuclear Spins." *Phys. Rev. Lett.* **113**, 267601 (2014).

[35] T. Otsuka, T. Nakajima, M. R. Delbecq, S. Amaha, J. Yoneda, K. Takeda, G. Allison, T. Ito, R. Sugawara, A. Noiri, A. Ludwig, A. D. Wieck, and S. Tarucha, "Single-electron Spin Resonance in a Quadruple Quantum Dot." *Scientific Reports* **6**, 31820 (2016).

[36] R. Jördens, N. Strohmaier, K. Günter, H. Moritz, and T. Esslinger, "A Mott insulator of fermionic atoms in an optical lattice." *Nature* **455**, 204 - 207 (2008).

[37] D. Tanese, H. Flayac, D. Solnyshkov, A. Amo, A. Lemaitre, E. Galopin, R. Braive, P. Senellart, I. Sagnes, G. Malpuech, and J. Bloch, "Polariton condensation in solitonic gap states in a one-dimensional periodic potential." *Nature Communications* **4**, 1749 (2013).

[38] A. Mazurenko, C. S. Chiu, G. Ji, M. F. Parsons, M. Kanász-Nagy, R. Schmidt, F. Grusdt, E. Demler, D. Greif, and M. Greiner, "A cold-atom Fermi-Hubbard antiferromagnet." *Nature* **545**, 462 - 466 (2017).

[39] A. Singha, M. Gibertini, B. Karmaker, S. Yuan, M. Polini, G. Vignale, M. I. Katsnelson, A. Pinczuk, L. N. Pfeiffer, K. W. West, and V. Pellegrini, "Two-Dimensional Mott-Hubbard." *Science* **332**, 1176 - 1179 (2011).

[40] J. Salfi, J. A. Mol, R. Rahman, G. Klimeck, M. Y. Simmons, L. C. L. Hollenberg, and S. Rogge, "Quantum simulation of the Hubbard model with dopant atoms in silicon." *Nature Communications* **7**, 11342, (2016).

[41] B. P. Lanyon, C. Hempel, D. Nigg, M. Müller, R. Gerritsma, F. Zähringer, P. Schindler, J. T. Barreiro, M. Rambach, G. Kirchmair, M. Hennrich, P. Zoller, R. Blatt, and C. F. Roos, "Universal Digital Quantum Simulation with Trapped Ions." *Science* **334**, 57 - 61 (2011).

[42] R. Barends, L. Lamata, J. Kelly, L. García-Álvarez, A. G. Fowler, A. Megrant, E. Jeffrey, T. C. White, D. Sank, J. Y. Mutus, B. Campbell, Y. Chen, Z. Chen, B. Chiaro, A. Dunsworth, I. C. Hoi, C. Neill, P. J. J. O' Malley, C. Quintana, P. Roushan, A. Vainsencher, J. Wenner, E. Solano, and J. M. Martinis, "Digital quantum simulation of fermionic models with a superconducting circuit." *Nature Communications* **6**, 7654 (2015).

[43] M. Imada, A. Fujimori, and Y. Tokura, "Metal-insulator transitions." *Reviews of Modern Physics* **70**, 1039 - 1263 (1998).

[44] L. Balents, "Spin liquids in frustrated magnets." *Nature* **464**, 199-208 (2010).

[45] P. W. Anderson, "Twenty-five years of high-temperature superconductivity - A personal review." *Journal of Physics* **449**, 012001 (2013).

[46] N. P. Ong and R. J. Cava, "Electronic Frustration on a Triangular Lattice." *Science* **305**, 5680 (2004).

[47] F. L. Pratt, P. J. Baker, S. J. Blundell, T. Lancaster, S. Ohira-Kawamura, C. Baines, Y. Shimizu, K. Kanoda, I. Watanabe, and G. Saito, "Magnetic and non-magnetic phases of a quantum spin liquid." *Nature* **471**, 612 - 616 (2011).

[48] S. Andergassen, "A frustrated trio." *Nature* **495**, 322 - 324 (2013).

[49] M. Seo, H. K. Choi, S. Y. Lee, N. Kim, Y. Chung, H. S. Sim, V. Umansky, and D. Mahalu, "Charge frustration in a triangular triple quantum dot." *Physical Review Letters* **110**, 046803 (2013).

[50] Y. Nagaoka, "Ferromagnetism in a narrow s band." *Physical Review* **147**, 392 (1966).

[51] J. Yoneda, "High-speed electrical gating of single electron spin qubits with semiconductor quantum dots." PhD thesis, The University of Tokyo, (2014).

[52] B. J. Van Wees, H. Van Houten, C. W. J. Beenakker, J. G. Williamson, L. P. Kouwenhoven, D. Van Der Marel and C. T. Foxon "Quantized conductance of point contacts in a two-dimensional electron gas." *Physical Review Letters* **60**, 9 (1988).

[53] J. M. Elzerman, R. Hanson, J. S. Greidanus, L. H. W. van Beveren, S. De Franceschi, L. M. K. Vandersypen, S. Tarucha and L. P. Kouwenhoven "Few-Electron Quantum Dot Circuit with Integrated Charge Read-Out." *Physical Review B* **67**, 161308(R) (2002).

[54] D. Schröer, A. D. Greentree, L. Gaudreau, K. Eberl, L. C. L. Hollenberg, J. P. Kotthaus, and S. Ludwig, "Electrostatically defined serial triple quantum dot charged with few electrons." *Physical Review B* **76**, 075306 (2007).

[55] M. A. Nielsen and I. L. Chuang, Quantum Computation and Quantum Information (Cambridge Series on Information and the Natural Sciences). Cambridge University Press, (2004).

[56] J. M. Taylor, J. R. Petta, A. C. Johnson, A. Yacoby, C. M. Marcus, and M. D. Lukin "Relaxation, dephasing, and quantum control of electron spins in double quantum dots." *Phys. Rev. B* **76**, 035315 (2007).

[57] J. Medford, J. Beil, J. M. Taylor, S. D. Bartlett, a C. Doherty, E. I. Rashba, D. P. Divincenzo, H. Lu, a C. Gossard, and C. M. Marcus "Self-consistent

measurement and state tomography of an exchange-only spin qubit." *Nature Nanotechnology* **8**, 654-659 (2013).

[58] E. A. Laird, J. M. Taylor, D. P. Divincenzo, C. M. Marcus, M. P. Hanson, and A. C. Gossard "Coherent spin manipulation in an exchange-only qubit." *Phys. Rev. B* **82**, 075403 (2010).

[59] J. M. Elzerman, R. Hanson, L. H. W. van Beveren, B. Witkamp, and L. M. K. V. and L. P. Kouwenhoven, "Single-shot read-out of an individual electron spin in a quantum dot." *Nature* **430**, 431 - 435 (2004).

[60] K. C. Nowack, M. Shafiei, M. Laforest, G. E. D. K. Prawiroatmodjo, L. R. Schreiber, C. Reichl, W. Wegscheider, and L. M. K. Vandersypen, "Single-Shot Correlations and Two-Qubit Gate of Solid-State Spins." *Science* **333**, 1269-1273 (2011).

[61] T. A. Baart, M. Shafiei, T. Fujita, C. Reichl, W. Wegscheider, and L. M. K. Vandersypen, "Single-Spin CCD." *Nat. Nanotechnol.* **11**, 330-334 (2015).

[62] F. H. L. Koppens, J. A. Folk, J. M. Elzerman, R. Hanson, L. H. W. van Beveren, I. T. Vink, H. P. Tranitz, W. Wegscheider, L. P. Kouwenhoven, and L. M. K. Vandersypen, "Control and detection of singlet-triplet mixing in a random nuclear field." *Science* **309**, 1346-1350 (2005).

[63] A. C. Johnson, J. R. Petta, C. M. Marcus, M. P. Hanson, and A. C. Gossard, "Singlet-triplet spin blockade and charge sensing in a few-electron double quantum dot" *Phys. Rev. B* **72**, 165308 (2005).

[64] A. C. Johnson, J. R. Petta, J. M. Taylor, A. Yacoby, M. D. Lukin, C. M. Marcus, M. P. Hanson, and A. C. Gossard, "Triplet-singlet spin relaxation via nuclei in a double quantum dot." *Nature* **435**, 925-928 (2005).

[65] J. R. Petta, H. Lu, and A. C. Gossard, "A Coherent Beam Splitter for Electronic Spin States." *Science* **327**, 669 - 673 (2010).

[66] S. Chesi, Y. D. Wang, J. Yoneda, T. Otsuka, S. Tarucha, and D. Loss, "Single-spin manipulation in a double quantum dot in the field of a micromagnet." *Phys. Rev. B* **90**, 235311 (2014).

[67] F. H. L. Koppens, C. Buizert, K. J. Tielrooij, I. T. Vink, K. C. Nowack, T. Meunier, L. P. Kouwenhoven, and L. M. K. Vandersypen, "Driven coherent

oscillations of a single electron spin in a quantum dot." *Nature* **442**, 766-771 (2006).

[68] E. I. Rashba, "Theory of electric dipole spin resonance in quantum dots: Mean field theory with Gaussian fluctuations and beyond." *Phys. Rev. B* **78**, 195302 (2008).

[69] Y. Tokura, W. G. Van Der Wiel, T. Obata, and S. Tarucha, "Coherent single electron spin control in a slanting zeeman field." *Phys. Rev. Lett.* **96**, 047202 (2006).

[70] T. Obata, M. Pioro-Ladrière, Y. Tokura, Y. S. Shin, T. Kubo, K. Yoshida, T. Taniyama, and S. Tarucha, "Coherent manipulation of individual electron spin in a double quantum dot integrated with a micromagnet." *Phys. Rev. B* **81**, 085317 (2010).

[71] J. Yoneda, T. Otsuka, T. Takakura, M. Pioro-Ladrière, R. Brunner, H. Lu, T. Nakajima, T. Obata, A. Noiri, C. J. Palmstrøm, A. C. Gossard, and S. Tarucha, "Robust micro-magnet design for fast electrical manipulations of single spins in quantum dots." *Appl. Phys. Express* **8**, 084401 (2015).

[72] G. Burkard, D. P. DiVincenzo, and D. Loss, "Coupled quantum dots as quantum gates." *Phys. Rev. B* **59**, 2070 (1999).

[73] W. H. Zurek, "Decoherence, einselection, and the quantum origins of the classical." *Reviews of Modern Physics* **75**, 715 - 775 (2003).

[74] L. M. K. Vandersypen and I. L, "NMR techniques for quantum control and computation." *Reviews of Modern Physics* **76**, 1037 - 1069 (2005).

[75] X. Hu and S. Das Sarma, "Charge-fluctuation-induced dephasing of exchange-coupled spin qubits." *Physical Review Letters* **96**, 100501 (2006).

[76] O. E. Dial, M. D. Shulman, S. P. Harvey, H. Bluhm, V. Umansky, and A. Yacoby, "Charge noise spectroscopy using coherent exchange oscillations in a singlet-triplet qubit." *Physical Review Letters* **110**, 146804 (2013).

[77] W. A. Coish and D. Loss, "Hyperfine interaction in a quantum dot: Non-Markovian electron spin dynamics." *Physical Review B* **70**, 195340 (2004).

[78] J. M. Taylor and M. D. Lukin, "Dephasing of quantum bits by a quasi-static mesoscopic environment." *Quantum Information Processing* **5**, 503 - 536 (2006).

[79] G. Dresselhaus, "Spin-orbit coupling effects in zenc blend structures." *Physical Review* **100**, 580 - 586 (1955).

[80] E. Rashba, "Properties of semiconductors with an extremum loop. 1. Cyclotron and combinational resonance in a magnetic field perpendicular to the plane of the loop." *Soviet Physics, Solid State* **2**, 1109 - 1122 (1960).

[81] P. Pfeffer, "Effect of inversion asymmetry on the conduction subbands in GaAs-$Ga_{1-x}Al_xAs$ heterostructures." *Physical Review B* **59**, 15902 - 15909 (1999).

[82] A. V. Khaetskii and Y. V. Nazarov, "Spin-flip transitions between Zeeman sublevels in semiconductor quantum dots." *Physical Review B* **64**, 125316 (2000).

[83] V. N. Golovach, A. Khaetskii, and D. Loss, "Phonon-induced decay of the electron spin in quantum dots." *Physical Review Letters* **93**, 016601 (2004).

[84] S. Amasha, K. MacLean, I. P. Radu, D. M. Zumbühl, M. A. Kastner, M. P. Hanson, and A. C. Gossard, "Electrical control of spin relaxation in a quantum dot." *Physical Review Letters* **100**, 046803 (2008).

[85] E. A. Chekhovich, M. N. Makhonin, A. I. Tartakovskii, A. Yacoby, H. Bluhm, K. C. Nowack, and L. M. K. Vandersypen, "Nuclear spin effects in semiconductor quantum dots." *Nature Materials* **12**, 494 - 504 (2013).

[86] W. A. Coish and J. Baugh, "Nuclear spins in nanostructures." *Physica Status Solidi (B)* **246**, 2203 - 2215 (2009).

[87] D. Paget, G. Lampel, and B. Sapoval, "Low field electron nuclear spin coupling in gallium arsenide under pumping conditions." *Physical Review B* **15**, 5780 - 5796 (1977).

[88] M. R. Delbecq, T. Nakajima, P. Stano, T. Otsuka, S. Amaha, J. Yoneda, K. Takeda, G. Allison, A. Ludwig, A. D. Wieck, and S. Tarucha, "Quantum Dephasing in a Gated GaAs Triple Quantum Dot due to Nonergodic Noise." *Physical Review Letters* **116**, 406802 (2016).

[89] I. A. Merkulov, A. L. Efros, and M. Rosen, "Electron spin relaxation by nuclei in semiconductor quantum dots." *Physical Review B* **65**, 205309 (2002).

[90] H. Bluhm, S. Foletti, I. Neder, M. Rudner, D. Mahalu, V. Umansky, and A. Yacoby, "Dephasing time of GaAs electron-spin qubits coupled to a nuclear bath exceeding 200 μs." *Nature Physics* **7**, 109 - 113 (2010).

[91] F. K. Malinowski, F. Martins, P. D. Nissen, E. Barnes, M. S. Rudner, S. Fallahi, G. C. Gardner, M. J. Manfra, C. M. Marcus, and F. Kuemmeth, "Notch filtering the nuclear environment of a spin qubit." *Nature Nanotechnology* **12**, 16 - 20 (2016).

[92] H. Bluhm, S. Foletti, D. Mahalu, V. Umansky, and A. Yacoby, "Enhancing the coherence of a spin qubit by operating it as a feedback loop that controls its nuclear spin bath." *Physical Review Letters* **105**, 216803 (2010).

[93] M. D. Shulman, S. P. Harvey, J. M. Nichol, S. D. Bartlett, A. C. Doherty, V. Umansky, and A. Yacoby, "Suppressing qubit dephasing using real-time Hamiltonian estimation." *Nature Communications* **5**, 5156 (2014).

[94] L. Gaudreau, A. Kam, G. Granger, S. A. Studenikin, P. Zawadzki, and Q. S. Sachrajda, "A tunable few electron triple quantum dot." *Applied Physics Letters* **95**, 193101 (2009).

[95] W. G. van der Wiel, S. De Franceschi, J. M. Elzerman, T. Fujisawa, S. Tarucha, and L. P. Kouwenhoven, "Electron transport through double quantum dots." *Reviews of Modern Physics* **75**, 1 - 22 (2003).

[96] J. Medford, J. Beil, J. M. Taylor, E. I. Rashba, H. Lu, a. C. Gossard, and C. M. Marcus, "Quantum-Dot-Based Resonant Exchange Qubit." *Physical Review Letters* **111**, 050501 (2013).

[97] D. J. Reilly, C. M. Marcus, M. P. Hanson, and A. C. Gossard, "Fast single-charge sensing with a rf quantum point contact." *Applied Physics Letters* **91**, 162101 (2007).

[98] C. Barthel, M. Kjærgaard, J. Medford, M. Stopa, C. M. Marcus, M. P. Hanson, and A. C. Gossard, "Fast sensing of double-dot charge arrangement and spin state with a radio-frequency sensor quantum dot." *Physical Review B* **81**, 161308(R) (2010).

[99] F. H. L. Koppens, D. Klauser, W. A. Coish, K. C. Nowack, L. P. Kouwenhoven, D. Loss, and L. M. K. Vandersypen, "Universal phase shift and non-exponential decay of driven single-spin oscillations." *Physical Review Letters* **99**, 106803 (2007).

[100] S. Nadj-Perge, S. M. Frolov, E. P. a M. Bakkers, and L. P. Kouwenhoven, "Spin-orbit qubit in a semiconductor nanowire." *Nature* **468**, 7327 (2010).

[101] E. Knill, D. Leibfried, R. Reichle, J. Britton, R. B. Blakestad, J. D. Jost, C. Langer, R. Ozeri, S. Seidelin, and D. J. Wineland, "Randomized benchmarking of quantum gates." *Physical Review A* **77**, 012307 (2008).

[102] E. A. Laird, C. Barthel, E. I. Rashba, C. M. Marcus, M. P. Hanson, and a. C. Gossard, "Hyperfine-Mediated Gate-Driven Electron Spin Resonance." *Physical Review Letters* **99**, 246601 (2007).

[103] V. P. Michal, T. Fujita, T. A. Baart, J. Danon, C. Reichl, W. Wegscheider, L. M. K. Vandersypen, and Y. V. Nazarov, "Non-linear and dot-dependent Zeeman splitting in GaAs/AlGaAs quantum dot arrays." *Physical Review B* **97**, 035301 (2017).